THE UNIVERSITY OF CHICAGO

MOLECULAR MECHANISMS OF RECEPTOR ACTIVATION DURING NERVOUS SYSTEM WIRING

A DISSERTATION SUBMITTED TO
THE FACULTY OF THE DIVISION OF THE BIOLOGICAL SCIENCES
AND THE PRITZKER SCHOOL OF MEDICINE
IN CANDIDACY FOR THE DEGREE OF
DOCTOR OF PHILOSOPHY

COMMITTEE ON NEUROBIOLOGY

BY
JOSEPH SHIN PAK

CHICAGO, ILLINOIS
DECEMBER 2021

What I know now is that we're all interconnected and that's a really beautiful thing. We have links to everyone else in our lives and in the world. Different people have different journeys for different reasons. You can't judge, but you can celebrate that there are connections everywhere.

-Jane Seymour

TABLE OF CONTENTS

ABSTRACT

During development, nervous system assembly is directed by a network of extracellular guidance cues that signal long- and short-range attraction and repulsion. Receptors expressed in the growth cones of axons respond to these cues, which can be secreted ligands or cell-surface proteins, leading to strengthening or reassembly of the cytoskeletal network of the growth cone. How these extracellular interactions translate into an intracellular response is yet an outstanding question in structural neurobiology, which we investigate in axonal and dendritic guidance in the developing spinal cord and olfactory system. First, the PVD neuron in *Caenorhabditis elegans* forms large dendritic arbors which are regulated by the quaternary Menorin complex. We demonstrate the ability to successfully purify component members from heterologous expression systems and form incomplete subcomplexes. In the mammalian spinal cord, the recently discovered NELL2-Robo3 complex has been demonstrated to mediate axon repulsion of commissural neurons during midline crossing. We present the structure of these proteins in complex and show that the EGF2-3 domains of NELL2 bind to the FN1 domain of Robo3. Mutation of the interface results in a decrease in binding affinity and a corresponding reduction in axon repulsion strength. Biophysical evidence collected using small-angle x-ray scattering (SAXS), multi-angle x-ray scattering (MALS), and analytical ultracentrifugation (AUC) suggests that Robo3 is a flexible, extended monomer in solution while NELL2 forms trimers which enhance axon repulsion. At high concentrations, NELL2-Robo3 complexes form gel-like condensates, which points to a signaling model where extended oligomers of Robo3 monomers are stabilized by NELL2 trimers. In the olfactory system, Kirrel2 and Kirrel3 regulate the coalescence of olfactory sensing neuron axons into distinct glomerular populations in the olfactory bulb. Our crystal structures reveal a mechanism of exclusive homodimer formation mediated by hydrogen bonding networks in Kirrel2 and hydrophobic interactions in Kirrel3. Furthermore, SAXS and AUC demonstrate that Kirrel2 and Kirrel3 form tip-to-tip dimers and lack additional binding sites that would enable cis-dimerization and extended oligomer formation. Ancestral sequence reconstructions of Kirrel family proteins highlight three residues that regulate the formation of homodimers through hydrophobic or hydrophilic interactions, suggesting that small changes in protein sequence were sufficient during evolution to expand the complexity of nervous system wiring. These three examples of neural wiring demonstrate the diversity of molecular interactions that mediate neurite guidance and its role in establishing complexity in the nervous system.

LIST OF TABLES

LIST OF FIGURES

CHAPTER 1: INTRODUCTION

The human nervous system is an incredibly complex network of billions of neurons with trillions of connections. How does such a complex organ coordinate its own self-assembly, and how did it come about? We will explore both questions in this dissertation through the exploration of structure and function of neural guidance cues, as well as the evolutionary relationships between these proteins among different animal species.

Development of neural tissue faces a unique challenge compared to other systems due to the complexity of neuron structure and connectivity (Hong and Luo 2014; Jan and Jan 2010a). Neurons themselves are highly polarized cells, capable of performing computations through cellular processes and must be connected to other cells through synapses at precisely defined locations for a neural circuit to perform physiologically relevant functions (Südhof 2017; Hong and Luo 2014). As an extreme case, some motor neuron axons can travel up to a meter in the human body and must navigate a complex extracellular environment before reaching their targets and form synapses (Giuffre and Jeanmonod 2018). This navigation is directed by cell-surface proteins which interact with their extracellular environment and relay this information back to the cell (Yamagata, Sanes, and Weiner 2003). Dysfunction of proper neural guidance cues is commonly correlated with cognitive and mental disorders; mutations in synaptogenic adhesion pairs Neurexin and Neuroligin are implicated in autism spectrum disorders, and mutations in the Semaphorin class of axon guidance cues are implicated in Schizophrenia (J. Chen et al. 2014; Gilabert-Juan et al. 2015). In order to investigate proper neural development, this dissertation will explore the mechanisms by which cell-adhesion molecules (CAMs) interact in order to direct neural projections.

Approaching these molecular interactions from a structural biology lens allows us to discover the basic molecular principles that guide protein-protein interactions (PPIs) and functions in the nervous system and generate new hypotheses on how those functions can be altered through genetic modification or therapeutic intervention. Structural biology has provided important insights into PPI function in the nervous system, such as how the assembly of clustered protocadherin networks contributes to neuronal self-recognition, or how synapse-specification proteins Neurexin and Neuroligin interact. Additionally, by examining how specific PPIs contribute to axon and dendritic guidance across different organisms, we can induce more general molecular principles of how guidance cues direct assembly of neuronal circuits.

1.1 GUIDANCE CUES IN NERVOUS SYSTEM DEVELOPMENT

Extracellular signals that direct axon and dendritic growth are known as guidance cues. These cues can be secreted or membrane-bound extracellular factors such as proteins or small peptides that encode attraction, repulsion, and adhesion, which activate receptors expressed on the growing tips of neurites, known as the growth cone (Figure 1) (Stoeckli 2018). Guidance cues are often used in combination or in sequence by neurons in order to make complex wiring decisions

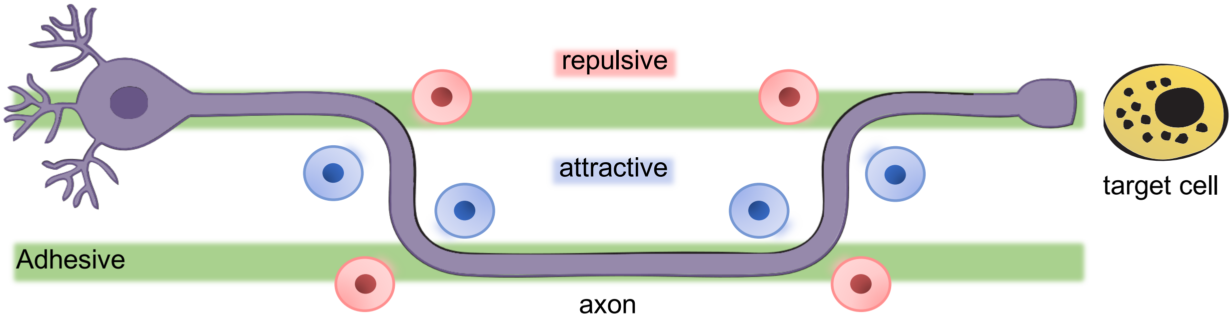

Figure 1: Guidance cues direct axonal growth.
Diagram of a neuron navigating extracellular guidance cues.

and reduce the demand for unique guidance cues to be encoded in the genome (Russell and Bashaw 2018; Komiyama and Luo 2006). The activation of growth cone receptors initiates a cellular response by the growing axon, leading to stabilization or destabilization of the actin cytoskeleton (Stoeckli 2018). How these extracellular interactions translate into an intracellular response is yet an outstanding question in structural neurobiology, which we investigate in axon guidance in the developing spinal cord and olfactory system. In the spinal cord, the recently discovered NELL2-Robo3 complex has been demonstrated to mediate axon repulsion of commissural neurons during midline crossing (Jaworski et al. 2015). We present the structure of these proteins in complex and show that the EGF2-3 domains of NELL2 bind to the FN1 domain of Robo3. Mutation of the interface results in a decrease in binding affinity and a corresponding reduction in axon repulsion strength. Biophysical evidence collected using small-angle x-ray scattering (SAXS), multi-angle x-ray scattering (MALS), and analytical ultracentrifugation (AUC) suggests that Robo3 is a flexible, extended monomer in solution while NELL2 forms trimers which enhance axon repulsion. At high concentrations, NELL2-Robo3 complexes form gel-like condensates, which points to a signaling model where extended oligomers of Robo3 monomers are stabilized by NELL2 trimers. In the olfactory system, Kirrel2 and Kirrel3 regulate the coalescence of olfactory sensing neuron axons into distinct glomerular populations in the olfactory bulb (Serizawa et al. 2006). Our crystal structures reveal a mechanism of exclusive homodimer formation mediated by hydrogen bonding networks in Kirrel2 and hydrophobic interactions in Kirrel3. Furthermore, SAXS and AUC demonstrate that Kirrel2 and Kirrel3 form tip-to-tip dimers and lack additional binding sites that would enable cis-dimerization and extended oligomer formation. Ancestral sequence reconstructions of Kirrel family proteins highlight three residues that regulate the formation of homodimers through hydrophobic or hydrophilic interactions, suggesting that small changes in protein sequence were sufficient during evolution to expand the complexity of nervous system wiring. These two examples of neural wiring demonstrate the diversity of molecular interactions that mediate axon guidance and its role in establishing complexity in the nervous system.

A major question when studying extracellular PPIs is determining how these interactions translate to a signal that is processed intracellularly (Ye et al. 2019). Typically, receptor activation involves a change in oligomeric state of the receptor, changes in conformational states, or recruitment of additional co-receptors that initiate kinase activity or recruitment of downstream signaling factors (Case, Ditlev, and Rosen 2019). For example, mammalian Slit-binding Robos, made up of 5 immunoglobulin (IG) domains and 3 Fibronectin type III (FN) domains fold in a way to form compact homodimers at the cell surface (Blockus and Chédotal 2016a). It is hypothesized that strong interactions between Robo and Slit and Heparan sulfate proteoglycans found in the extracellular matrix introduce molecular tension that pulls the compact Robo homodimer into an open conformation, which alters the intermolecular spacing between the Robo c-terminal tails, initiating downstream signaling. Thus, understanding the translation of extracellular PPIs into receptor activation is a key bridge between the structure of guidance cues and their function in nervous system wiring. In a similar vein, we will investigate Robo3, a paralog of mammalian Robo1 and Robo2, and the mechanisms of its interactions with a unique ligand, NELL2, which also mediates axon repulsion in the developing spinal cord.

1.2 AXON GUIDANCE IN THE SPINAL CORD

All bilaterians have a midline that bisect the animal into two symmetric halves. The crossing of the midline by commissural neuron axons during development ensures coordination between the two halves of the body (Vulliemoz, Raineteau, and Jabaudon 2005). In mammals, the axons of interneurons that undergo midline crossing, known as commissural neurons, travel ventrally toward the floor plate of the spinal cord where it crosses once, then travels anteriorly through the spinal cord (Figure 2) (Dickson and Gilestro 2006). The receptor Deleted in Colorectal Cancer (DCC) mediates attractive movement toward the floor plate with its ligand Netrin1, and the receptors Roundabout 1 (Robo1) and Robo2 mediate repulsion away from the floorplate with the ligands Slit1, Slit2, and Slit3 (Figure 2). In the mammalian system, Robo3, a divergent member of the Robo family of receptors, regulates the activity of DCC and Robo1/2 signaling through its cytoplasmic C-terminal tail (Zelina, Blockus, Zagar, Péres, Friocourt, Wu, Rama, Fouquet, Hohenester, Tessier-Lavigne, Schweitzer, Crollius, et al. 2014, 3). The isoform Robo3.1, which performs this regulation, is expressed in commissural axons prior to crossing the midline and represses Robo1/2 signaling while potentiating DCC signaling, ensuring that the axon crosses through the floorplate (Figure 3). Upon crossing the midline, an expression switch causes the

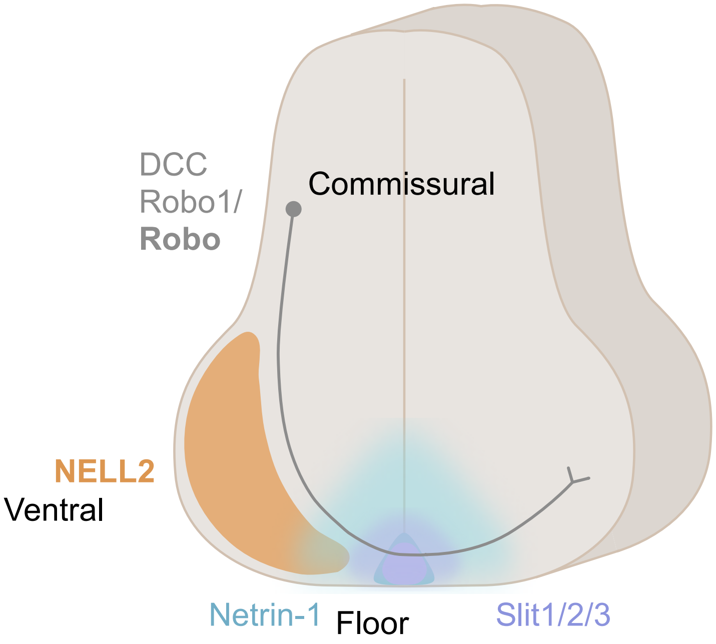

Figure 2: Diagram of a commissural axon crossing the floorplate in the mouse spinal cord.
DCC, Robo1/2, Robo3 are receptors expressed on the commissural neuron, NELL2 is secreted from the ventral horn, and Netrin and Slit1/2/3 are secreted from the floor plate

Robo3.2 isoform to be expressed, which does not regulate Robo and DCC activity and Robo1/2 repulsion away from the midline is restored. How this signaling switch is coordinated is yet an outstanding question in the field of spinal cord development.

Beyond its role in regulating the attractive and repulsive movements of axons in the spinal cord, Robo3 is also capable of performing axon guidance with a ligand like its paralogs. NELL2 was recently identified as a Robo3 ligand and is expressed in the motor column of the spinal cord (Jaworski et al. 2015). NELL2 demonstrated axon repulsive ability in commissural neurons *in vitro*, while animals lacking NELL2 in a sensitized *Robo3*$^{+/-}$ heterozygote displayed improper innervation of the motor column by commissural neurons. Thus, NELL2 and Robo3 seem to ensure that commissural neurons do not enter into the motor column inappropriately and instead cross through the floorplate. This additional function of NELL2-mediated axon repulsion appears useful in a larger, more complex system with increased variability in dorsal-ventral and medial-lateral positioning. Additionally, its divergence from Robo1/2, and the evolution of its interactions and functions in spinal cord development appears to address and allow for the increased

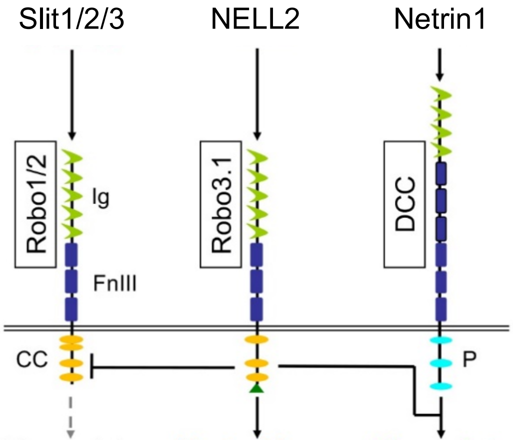

Figure 3: Coordination of DCC, Robo1/2, and Robo3 signaling in the mammalian spinal cord.
Robo1/2 signal axon repulsion with ligands Slit1/2/3 while DCC signals axon attraction with Netrin1. Robo3.1 suppresses Robo1/2 signaling while potentiating DCC signaling with its C-terminal tail. Robo3.1 also signals axon repulsion with its ligand NELL2.

complexity of the mammalian nervous system.

1.3 EVOLUTION OF NERVOUS SYSTEM WIRING

Generation of more complex wiring systems from simpler ones requires evolution of new proteins and functions. New proteins arise following gene duplication events, which creates multiple copies of the same protein and reduces selective pressure on these copies, allowing for more extensive additions, deletions, or translocation mutations and development of new protein functions (Siddiq, Hochberg, and Thornton 2017; Hochberg and Thornton 2017). These new protein functions are preserved if they are incorporated into biological processes and allow rapid advances in evolution. Often, the resulting proteins from gene duplication can distribute the functions of a single promiscuous, multifunctional protein into several proteins with fewer but specialized functions. More rarely, protein copies will develop *de novo* interactions and functions that can be incorporated into cellular processes. For neuronal guidance cues, the proliferation of additional proteins allows for a more diverse set of interactions with more unique combinations of protein-protein interactions. For example, rapid expansion of the Wirin family of IG family proteins has produced a combinatorial system of related ligand-receptor pairs such as *Drosophila* Dprs and DIPs. 38 known interactions between the 11 DIPs and 21 Dprs are used throughout the fly nervous system to specify synapse formation, act as neuronal adhesion molecules, and overall act as molecular identifiers for specific neuronal populations (Cheng, Ashley, et al. 2019).

Mounting genetic evidence has demonstrated that most modern vertebrates have undergone two rounds of whole-genome duplication, known as the 2R hypothesis, giving rise to up to four copies of each gene. This expansion of protein templates allows for the development of more complex functions in organismal development as protein functions diverge and specialize. The divergence of the mammalian Robo3 from Robo1/2 provides an opportunity to study the development of new protein functions following genome-wide duplications. Robo and Slit binding is conserved among all bilaterian animal species, and yet mammalian Robo3 lacks Slit binding completely and instead binds NELL2 with strong affinity (Blockus and Chédotal 2016a, 3; Friocourt and Chédotal 2017, 3). This Robo3-NELL2 interaction is either a *de novo* interaction within the Robo3 lineage of proteins or a segregation of functions from a promiscuous ancestor capable of binding to both Slit and NELL into specialized descendants binding to either Slit or NELL. In either case, the coordination of Robo1, Robo2, and Robo3 activity within the spinal cord represent a necessary expansion of functions in order for commissural neurons to navigate an increasingly complex spinal cord.

1.4 KIRREL HOMODIMERIZATION IN THE OLFACTORY SYSTEM

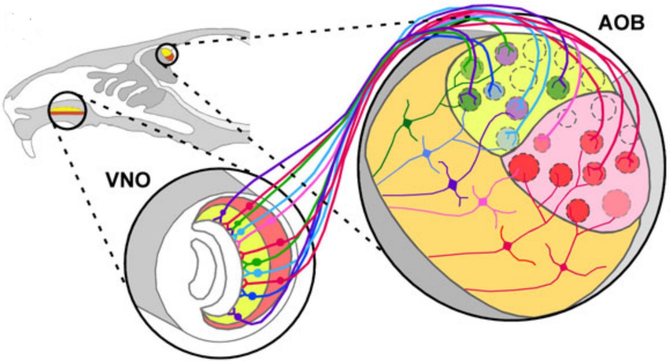

Figure 4: Coalescence of accessory olfactory neuron axons in the accessory olfactory bulb.
Randomly distributed sensory neurons in the olfactory epithelia project to the olfactory bulbs while axons expressing the same odorant receptors sort into glomeruli (from *Principles of Animal Communication*).

Another example of gene duplication producing greater diversity in neuronal wiring can be seen in the direction of olfactory system wiring by Kirrel2 and Kirrel3. In the vertebrate olfactory system, olfactory sensory neurons (OSNs) express individual odorant receptors (ORs) that respond to distinct molecular motifs (Wang et al. 1998). These olfactory sensory neurons project directly into the olfactory bulb of the cortex, where they coalesce into glomeruli of uniform populations of OSNs expressing the same ORs (Figure 4). Kirrel2 and Kirrel3 direct this coalescence in the mouse nervous system. Kirrel2 and Kirrel3 are expressed in distinct populations of OSNs, which project axons to four distinct populations of glomeruli: Kirrel2-only, Kirrel3-only, high-Kirrel2 low-Kirrel3, and high-Kirrel3 low-Kirrel2. Both Kirrel2 and Kirrel3 form exclusive homodimers, which are hypothesized to direct axon sorting into specific glomeruli (Serizawa et al. 2006; Prince et al. 2013). Loss of the distinction between Kirrel2 and Kirrel3-expressing neurons leads to behavioral defects, as Kirrel3 knockout mice are unable to distinguish between male and female and indiscriminately mount animals in an attempt to mate and exhibit reduced male-male aggression.

A more difficult question to answer is how these gene duplication events lead to the divergence of functions as well as the development of *de novo* interactions and functions. As we are limited in our ability to only access the genomes of extant animals, we cannot trace the actual evolution of proteins from their ancestral states to their current ones. However, recent advances in genomics and computational analyses present an alternative approach: the reconstruction of ancestral protein states from the sequences of large numbers of extant organisms (Hochberg and Thornton 2017). While extant paralogs contain many differences in protein sequence—the primary sequence of Robo3 is only 52% identical with Robo1—ancestral protein states represent a hypothetical moment in evolutionary time prior to its radiation into contemporary states. Therefore, fewer differences in primary sequence exist in ancestral states, allowing for easier identification of residues involved in the divergence of protein functions. By understanding how protein functions evolve, we can understand how nervous systems build in complexity.

CHAPTER 2: THE MENORIN COMPLEX AND DENDRITE MORPHOGENESIS

2.1 INTRODUCTION:

Proper neural circuit wiring requires that both axons and dendrites have been directed to their correct targets. While axon guidance has been extensively studied, mechanisms unique to dendritic arborization are less well known. The PVD neuron found in *Caenorhabditis elegans* is a useful model for studying dendrite morphogenesis due to its large, elaborate dendritic arbor that organizes into four levels of evenly spaced, orthogonal branches (Figure 5A). One PVD neuron's dendritic arbor encompasses the entire length of half of the worm's body and is responsible for sensation of harsh touch. A quaternary complex has been identified as the primary cell-adhesion complex to direct this growth; Dendritic Morphology Abnormal 1 (DMA-1), the receptor expressed on the PVD neuron, binds to three ligands: Sensory AXon guidance 7 (SAX-7), MeNoRin 1 (MNR-1), and LEukocyte-cell derived ChemoTaxin 2 (LECT-2, Figure 2)(Zou et al. 2016; Dong et al. 2013; Díaz-Balzac et al. 2016; Salzberg et al. 2013). This hypothesized complex of MNR-1, SAX-7, and LECT-2 bound to DMA-1 will hereafter be referred to as the *Menorin* complex (Figure 6). Such a large complex to govern dendritic guidance is unusual, as most guidance cues are homophilic dimers as in the case of Kirrels, or binary receptor-ligand pairs, as in the case of Netrin/DCC, or Robo/Slit. The discovery of this quaternary guidance complex raises the question of whether its function differs from other kinds of binary guidance complexes. Dong,

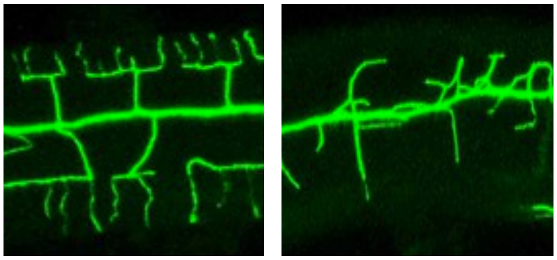

Figure 5: PVD neuron morphology
A and **B**. Wild-type (**A**) and *lect-2* mutant (**B**) phenotypes of the PVD neuron

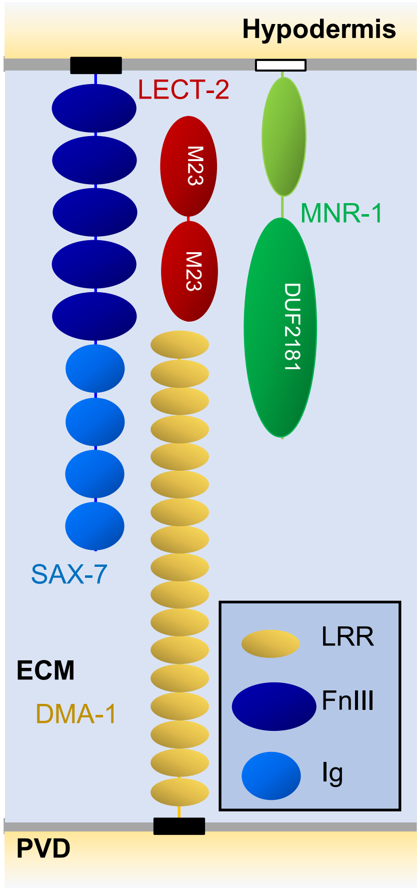

Figure 6: Schematic of the Menorin complex extracellular domains. DMA-1 contains 17 Leucine-rich repeat (LRR) domains, SAX-7 contains 5 Fibronectin type III (FnIII) domains and 4 Immunoglobulin (Ig) domains, LECT-2 contains 2 Metalloprotease 23 (M23) domains, and MNR-1 contains a Domain of Unknown Function 2181 (DUF2181) and a yet unidentified domain.

et al. shows that each individual guidance cue is insufficient for proper guidance of the higher-order branches, with the three cues together creating a path for PVD dendrite growth at the intersection of their individual localization patterns—SAX-7 is expressed in hypodermal cells and certain types of neurons, but not the PVdD neuron itself; MNR-1 is expressed in the hypodermis exclusively; and LECT-2 is secreted from muscle cells and collects along the sublateral line and in commissures (Figure 7). Loss of any single member of the complex results in abrogation of the candelabra phenotype with 100% penetrance (Figure 5B). Rather than integrating the signals of multiple ligand-receptor guidance cues, the quaternary Menorin complex appears to function as a molecular coincidence detection system where the conditions for DMA-1 activation are only satisfied in the overlay of the three ligands in an all-or-nothing response, laying out a delineated path for dendrite growth. While it is common for multiple binary cue systems to be involved in growth cone guidance, simultaneous detection of three signals by a single receptor is a novel mechanism that we will elucidate with our experimental approach (Figure 7).

The data presented here will lay out the progress we have made in determining the molecular mechanisms of interaction of the quaternary Menorin complex, including crystal structures and simulated models, as well as characterization of domain-domain interactions between complex members. Continued work will provide a model of interaction for deeper study of dendrite arborization through genetic manipulation of Menorin complex members and paves the way for the discovery and study of other molecular coincidence detection systems in the future.

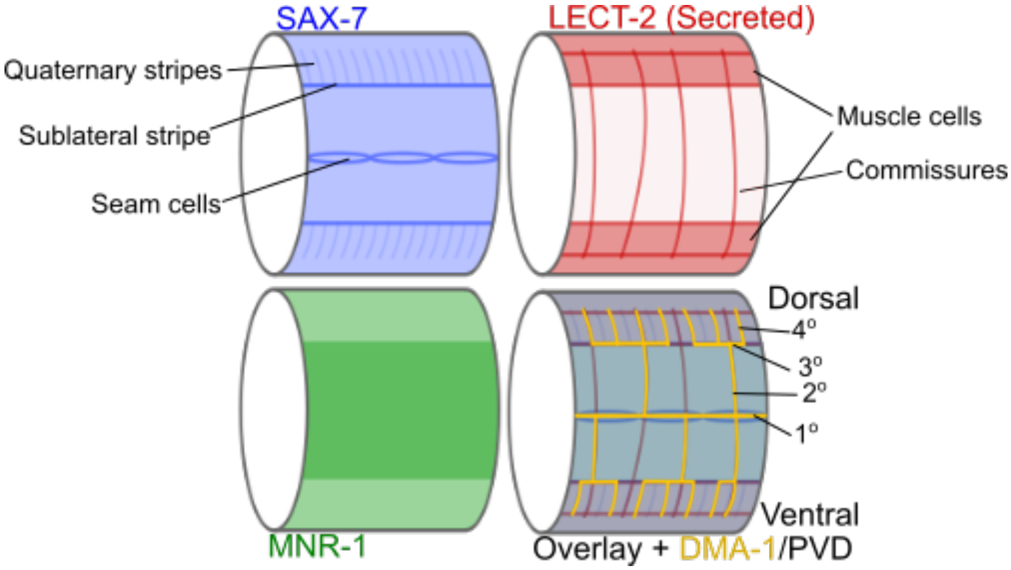

Figure 7: Menorin complex compenent expression patterns
Schematic of SAX-7 (top left), MNR-1 (top right), LECT-2 (bottom left), and overlay (bottom right) expression patterns, with PVD schematic (expressing DMA-1) drawn on the overlay with primary, secondary, tertiary, and quaternary branches identified.

2.2 RESULTS

2.2.1 Crystallization of Menorin complex components

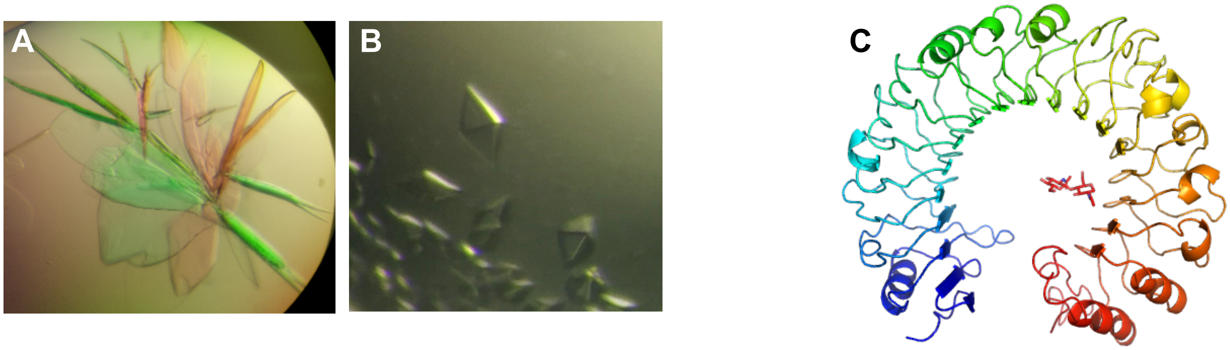

Figure 8: SAX-7 and DMA-1 crystals
A: SAX-7 crystals, **B**: DMA-1 crystals **C**: Crystal structure of DMA-1. 17 leucine-rich repeats form a horseshoe shape, with evidence of glycans in the center of the structure.

In order to determine the mechanisms of interaction between SAX-7 and DMA-1, we set out to crystallize the individual components of the Menorin complex, as well as smaller subcomplexes. While structural determination of the whole quaternary complex would provide the greatest amount of information toward understanding the assembly of the individual members, structures of the individual proteins can provide phasing information required for determination of the whole complex, and structures of smaller subcomplexes would provide important insight into the sequential order of complex assembly. While full ectodomain (ECD) SAX-7 was not able to produce crystals, a SAX-7 construct containing only the fibronectin (FN) type III domains (SAX-7 FN1-5) was concentrated to 15 mg/ml and crystallized using the NeXtaL suite of crystallization screens (Core I, Core II, Core III, Core IV, Pro-complex, and PACT suites). Crystals were formed in over 50% of conditions tested and took on the form of highly birefringent clusters of wide, flat crystals joined together at a single nucleation point (Figure 8A). DMA-1 ECD was concentrated to 10 mg/ml and crystallized using the same crystallization screens and yielded crystals only in the condition containing 0.2 M Potassium thiocyanate, 0.1 M Bis-Tris-Propane pH 8.5, and 20% Polyethylene glycol (PEG 3350), which were large enough for further processing. DMA-1 ECD crystals were bipyramidal and formed along the boundary between the protein and crystallization solutions (Figure 8B). Initial SAX-7 FN1-5 and DMA-1 ECD crystals were frozen and shipped to the Advanced Photon Source (APS) where X-ray diffraction images were collected.

SAX-7 FN1-5 produced datasets that exhibited strong anisotropy, likely due to the flat morphology of the crystals formed and diffracted to a maximum resolution of 4 Å. SAX-7 FN1-5 crystal optimization was attempted, using varied pH and PEG 3350 concentration, as well as the use of the Rx Salt screen (Hampton), though none of the optimized conditions tested produced crystals that provided better diffraction data. DMA-1 ECD crystals diffracted to 3 Å and provides acceptable resolution for determination of side chain orientations in crystal structures. However, due to the lack of structural models available, molecular replacement could not be used to determine phasing information. Seleno-methionine (SeMet) labeling was attempted in order to use anomalous diffraction data to solve the phasing issue but caused a decrease in protein yield and was not a viable method for producing crystals. Soaking with heavy metal solutions also did not produce any anomalous diffraction data. However, using AlphaFold, a model was generated that was sufficiently close enough in structure to be used as a molecular replacement model to determine the true structure of DMA-1 ECD (Figure 8C). As predicted, the structure is composed solely of 15 LRRs capped by an N- and C-terminal LRR domain and forms a large horseshoe shape, in an almost completely circular conformation.

2.2.2 SAX-7 and LECT-2 in complex:

A physical association of LECT-2 with SAX-7 has been shown to be required for the proper formation of the quaternary complex (Zou et al 2016). LECT-2 localization overlaps with SAX-7 in the quaternary stripes branching from the sublateral stripes, suggesting that these two proteins alone are capable of forming a high-affinity complex. In order to determine whether SAX-7 and LECT-2 form a complex as the first step in the formation of the quaternary complex, we set out to purify and crystallize the LECT-2:SAX-7 complex. We purified both proteins using the baculovirus expression system, capturing the proteins on Ni-NTA resin and performing fast-protein liquid chromatography (FPLC) to obtain a purified sample of proteins. Gel filtration was performed again with simultaneous injection of both proteins, and displayed a leftward shift in its elution profile, indicating that SAX-7 and LECT-2 alone are capable of forming a high-affinity complex (Figure 9). In order to determine which domains of SAX-7 interact with LECT-2, we designed a FLAG-tagged LECT-2 and attempted to pull down constructs of SAX-7 containing its component domains using anti-FLAG resin. While SAX-7 ECD, SAX-7 IG1-4 and SAX-7 FN1-5 were expressed, smaller domain groupings of SAX-7 and individual domains did not express. Of the expressing constructs, only SAX-7 ECD and SAX-7 FN1-5 eluted with LECT-2-FLAG, confirming that the FN domains are required for SAX-7:LECT-2 complex formation, and not the IG domains (Figure 10B).

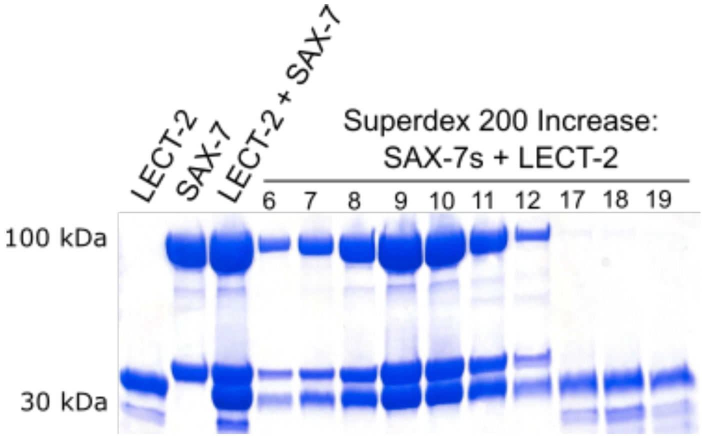

Figure 9: LECT-2 and SAX-7 form a complex over gel filtration.
LECT-2 and SAX-7 elute together from a Superdex 200 chromatography FPLC column (fractions 6-12). Injected solution contained an excess of LECT-2 (fractions 17-19).

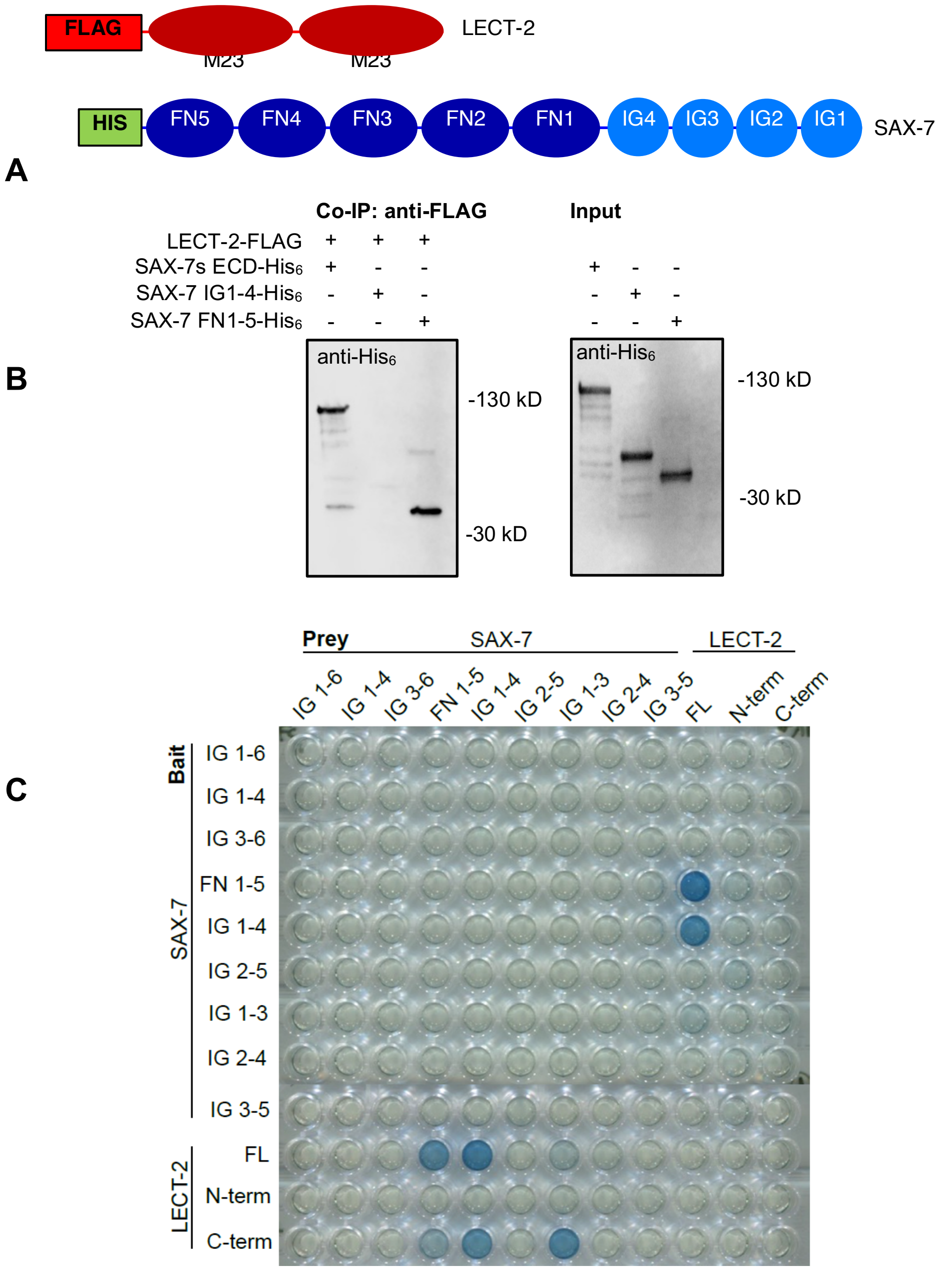

Figure 10: SAX-7 and LECT-2 physical interactions

A. Schematic of LECT-2 and SAX-7 ectodomains. **B.** Co-immunoprecipitation of SAX-7 domains with LECT-2 show SAX-7 ECD and FN1-5 pull down with LECT-2, while SAX-7 IG1-4 does not. **C.** ECIA of SAX-7 domains against LECT-2 domains. SAX-7 FN1-5 and FN1-4 bind LECT-2 while other domains display no or weak interactions. LECT-2 C-terminal domain shows binding to SAX-7 FN1-5, FN1-4, and FN1-3 but only when expressed as a prey construct.

In order to dissect further which domains specifically are involved in binding between LECT-2 and SAX-7, we performed the extracellular interactome assay (ECIA) as previously published to test for domain interactions and confirmed LECT-2 to bind to the FN1-5 domains for SAX-7. Interestingly, we observed binding of LECT-2 to SAX-7 FN1-4, but not to FN2-5 or FN3-5 (Figure 10C). This result is at odds with the previously published results by Zou et al. showing binding between LECT-2 and the C-terminal fragment of SAX-7 (CTF) which extends from the furin cleavage site to the end of the ECD, encompassing part of FN3 as well as FN4-5. This may be due to an inability of the FN3-5 domains to fold properly without the presence of the FN1 or FN2 domains. Alternatively, native cleavage of the furin site to produce the SAX-7 CTF may expose a new binding site that cannot be reproduced in a heterologous expression system. Additionally, the LECT-2 C-terminal domain displayed binding to the FN1-3 domains, although this interaction was only weakly observed with the full-length LECT-2 and only as an Fc-tagged construct. Crystallization trials were attempted using these binding domains, as well as LECT-2 alone, although none of the screens produced crystals of LECT-2 alone or in complex with SAX-7. Constructs tested for crystallization include LECT-2 FL and the LECT-2 C-terminal domain in solution with SAX-7 FL, SAX-7 FN1-5, SAX-7 FN1-3, or SAX-7 FN3-5. Despite the lack of crystal structures, these results, in conjunction with previous results, appear to demonstrate that the SAX-7 FN1, FN2, and FN5 domains are dispensable for binding to LECT-2. While the exact sequence of interaction between complex members as of yet cannot be determined, the formation of a high-affinity complex between SAX-7 and LECT-2 suggests that it occurs early in complex assembly, prior to interaction with the receptor DMA-1.

2.2.3 Co-expression of MNR-1 and SAX-7

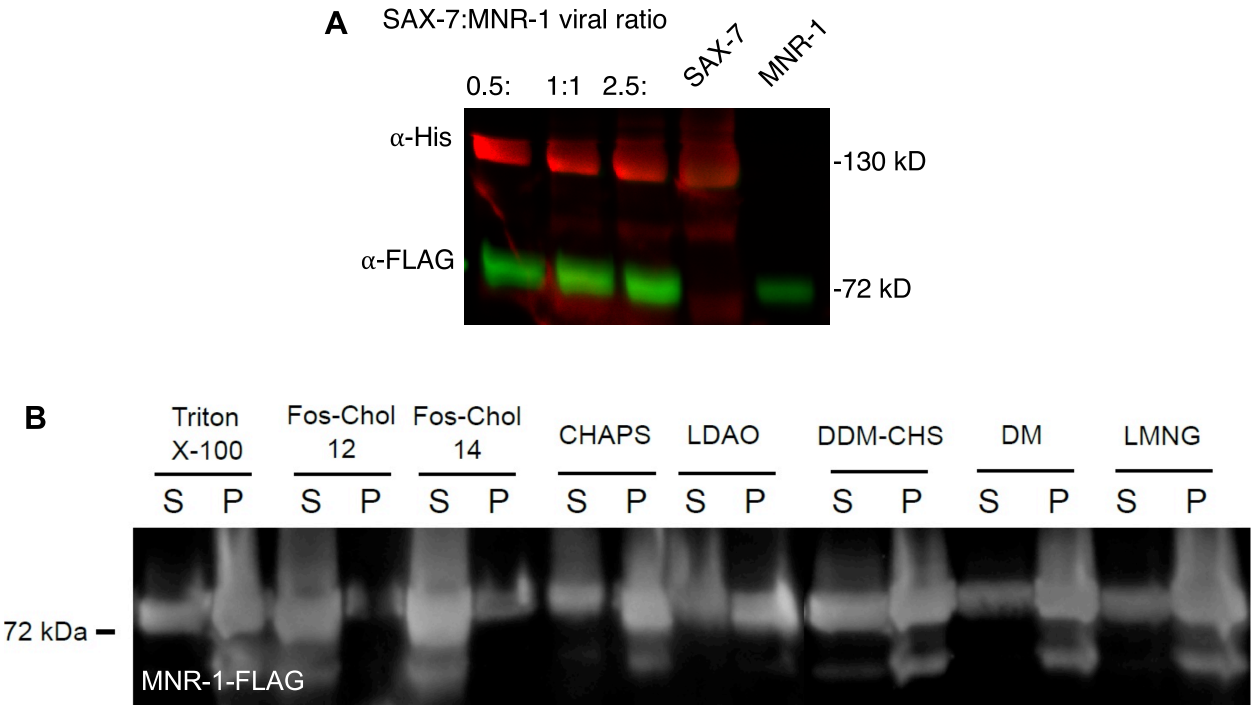

Figure 11: MNR-1 expression and solubilization

A. Co-infection of High Five cells with membrane-bound SAX-7 and MNR-1 improves MNR-1 expression (Red: SAX-7-ECD-His$_6$, Green: MNR-1-FLAG). **B.** Detergent screen to test the effectiveness of different detergents on extraction of MNR-1 from plasma membranes.

In order to determine how MNR-1 is incorporated into the quaternary complex, we set out to determine its interactions with other proteins. While MNR-1 was produced in very low quantities as a secreted construct, we created a membrane-bound construct by appending the amino-acid sequence "ATFLYKVVSSAT" to extend the hydrophobic C-terminal tail of MNR-1 and create a complete transmembrane domain, in addition to a final C-terminal hexahistidine or FLAG tag. A MNR-1 construct with a FLAG-tag (MNR-1-FLAG) was co-expressed with hexahistidine-tagged SAX-7 (SAX-7-ECD-His$_6$) in serum-free SF9 cells, increasing MNR-1 expression and suggesting that SAX-7 improves MNR-1 expression in a chaperone-like effect through a physical interaction between the two proteins (Figure 11A). In order to determine an appropriate detergent for extraction of SAX-7 and MNR-1, we tested multiple detergents in a small-scale assay (Figure 11B). As a detergent mixture of heterogeneous length, Triton X-100 was used as a positive control to determine whether the proteins could be extracted, and was tested alongside Fos-Chol 12, Fos-Chol 14, CHAPS, LDAO, DDM-CHS, DM, and LMNG (Anatrace). While all detergents extracted both MNR-1 and SAX-7 from membranes to some degree, Fos-Chol 12 and Fos-Chol 14 displayed the greatest degree of solubilization, with almost all of the protein localized to the supernatant fraction following solubilization and very little protein found in the insoluble pellet. However, as Fos-Chol 12 and Fos-Chol 14 are zwitterionic detergents, they are more likely to disrupt protein-protein interactions and denature proteins compared to nonionic detergents. The DDM-CHS mixture was the next most effective in extracting MNR-1 and SAX-7 from the membrane and is a nonionic detergent supplemented with CHS to mimic cholesterols present in the plasma membrane. As a mild detergent with good solubilization, we chose to attempt reconstitution of the full quaternary structure using this detergent in future experiments.

To test whether MNR-1 folds properly in SF9 cells and can be extracted by DDM-CHS without harming its activity as a co-ligand, we co-infected SAX-7 and MNR-1 in 1 l of serum-free SF9 cells in a large-scale purification. Purification using His-tagged resin resulted in the pulldown of a large number of contaminants whereas use of anti-FLAG resin during purification resulted in the pulldown of fewer contaminants, but greatly reduced protein yield overall. Continued optimization of this procedure, however, will likely lead to production of enough pure MNR-1:SAX-7 complexes for use in cryo-EM experiments.

2.3 DISCUSSION

While only limited progress has been made in the structural determination of the Menorin complex, we have determined key strategies in the production of the component proteins in order to do further analysis on the mechanisms of assembly. Notably, the structure of the receptor DMA-1 has been solved, marking an important first step in the determination of the overall complex. The structure shares the stereotypical horseshoe shape of other LRR family proteins, which play a large role in nervous system development in humans, especially in synapse specification (Schroeder and de Wit 2018). DMA-1 also exhibits high expression of protein as secreted baculovirus constructs sufficient for crystallization in addition to single-particle electron microscopy. However, this expression has proven to be inconsistent in the past, with sudden loss of expression, which may be attributed to the health of the virus or the health of the High-Five cells used for protein expression. Careful care must be taken to ensure consistent cell maintenance and proper storage of viruses in the future. While SAX-7 FN1-5 has produced crystals, it has exhibited poor diffraction and high anisotropy, representing an obstacle to final determination of its structure. Due to the interactions of these domains with LECT-2, and their demonstrated importance in rescuing the *in vivo* phenotype (Salzberg et al. 2013), producing these crystals capable of diffracting at higher resolutions with a complete dataset could provide important insights into its interactions with its binding partners.

LECT-2 has been demonstrated to bind to SAX-7 with high affinity and may do so as an initial step in the formation of the complex. We confirmed that LECT-2 binds to the SAX-7 FN domains with our co-IP and our ECIA data demonstrate binding between LECT-2 and the FN1-4 domains of SAX-7, as well as between the LECT-2 N-terminal domain and the FN1-3 domains of SAX-7. Previous studies have demonstrated that constructs that lack FN3 are unable to rescue *sax-7* knockout phenotypes, though it is possible that the FN3 domain alone is not binding to LECT-2. The ECIA interactions that we observed together with previously published data suggest that the FN3 and FN4 domains of SAX-7 primarily mediate binding with LECT-2. Additionally, a furin site located in the FN3 domain results in complete cleavage of SAX-7 into two chains, although gel chromatography results in the elution of a single protein. We have not yet tested whether this cleavage is necessary for interactions between SAX-7 and LECT-2, although the CTF, which binds to LECT-2, contains only the c-terminal half of the FN3 domain (Zou et al. 2016). While furin-mediated cleavage is likely not required for binding between SAX-7 and LECT-2, it may play a role in the regulation of DMA-1 signaling, by allowing for dissociation of the two halves of SAX-7 through physical force and internalization of the entire complex (Dong et al. 2016).

While MNR-1 is the namesake of this complex, it is the most difficult protein to express in high quantities. Testing of secreted constructs in both High Five and S2 insect cell lines have yielded very little protein but the expansion of a C-terminal hydrophobic tail into a full transmembrane in MNR-1 resulted in a modest increase in protein expression, making determination of a complex structure through cryo-EM a more viable option than crystallography. Co-expression with full-length SAX-7 also improves MNR-1 expression, which mimics SAX-7 and MNR-1 coexpression on the surface of hypodermis cells and may represent a more physiologically relevant interaction between the two proteins compared to a complex of secreted proteins (Salzberg et al. 2013; Díaz-Balzac et al. 2016; Dong et al. 2013). A possible scenario where the structure of the complex is determined using cryo-EM would involve first purifying SAX-7 and MNR-1 as solubilized membrane-bound constructs while LECT-2 and DMA-1 are expressed and purified as secreted constructs. LECT-2 and DMA-1 would be added to the solubilized membrane proteins in a 1:1 ratio immediately before freezing into cryo-EM grids. Successful determination of the complex structure, even a partial complex would provide valuable information on the sequence of complex assembly and stoichiometric ratios of component proteins.

2.4 METHODS:

2.4.1 Molecular cloning

Plasmids containing DNA sequences for DMA-1, SAX-7, LECT-2, and MNR-1 were obtained from the laboratory of Dr. Kang Shen. DNA constructs for protein expression were inserted into pAcGP67A (BD Biosciences) vectors for large-scale baculovirus-mediated expression and pECIA (Ozkan et al. 2013) vectors for S2 transient protein expression and interaction screening. A Hexahistidine (His_6) or FLAG (DYKDDDDK) tag was included in all constructs to aid in purification using Ni-NTA (Qiagen) or anti-DYKDDDDK G1 (GenScript) resin and for detection on western blot. PCRs were run using the Phusion polymerase system and included 5' overhangs to be incorporated into the target vectors using Gibson assembly. Assembled constructs were transformed into *E. coli* DH5α cells, grown in LB media and purified using the Qiagen miniprep kit. Plasmid sequences were by the University of Chicago Comprehensive Cancer Center DNA Sequencing and Genotyping facility prior to use in further experiments.

2.4.2 Baculovirus production

Constructs in pAcGP67A vectors were transfected into Sf9 cells (From *Spodoptera frugiperda*, Thermo Fisher) using either Cellfectin II (Thermo Fisher) or TransIT-Insect (Mirus) in stationary 6-well plates. Cells were incubated in the transfection media for 7-10 days in order to accumulate virus in the culture media. This initial generation of virus (P0) was then amplified by adding 200 μl of virus to 15 ml suspension cultures, with daily addition of cells or media to maintain a 2 million/ml density until reaching 50 ml total volume. This generation of amplified virus (P1) was harvested after 7 days post-infection by spinning down the cells at 250 × *g* for 5 min. Virus amplification was repeated if protein expression was low.

2.4.3 Protein expression and purification

For protein expression, High Five cells (from *Trichoplusia ni*, Thermo Fisher) grown in serum-free media were infected in small scale (2.5 ml in 6-well plates) or large scale (up to 1L in 2.7 L flasks) cultures and incubated for 60-72 hours. The culture was then spun down at 900 × *g* for 15 min, after which either the supernatant (for secreted proteins) or the cell pellet (for membrane-bound proteins) was transferred to another container. The supernatant was incubated for 30 min with 50 mM Tris, pH 8.0, 5 mM $CaCl_2$, and 1 mM $NiCl_2$ to precipitate unwanted contaminants in the media and reduce nonspecific binding of contaminants to Ni-NTA resin. The precipitate-media suspension was spun down at 8000 × *g* and the supernatant was collected into a fresh container. 2 ml of 50% Ni-NTA slurry was added to each liter of supernatant and incubated for 3-5 hours. Ni-NTA resin was collected in a glass funnel, washed with 50-100 ml of HEPES-buffered saline (HBS, 10 mM HEPES, 150 mM NaCl, pH 7.4) with 20 mM imidazole, and transferred to a Econo-Pac (Bio-Rad) chromatography column. Proteins were eluted with 200 mM imidazole in HBS, concentrated in Amicon Ultra centrifugal filter units (Millipore Sigma), and purified using gel filtration chromatography.

For membrane-bound proteins, cells pellets were resuspended in ice-cold lysis buffer (25 mM Tris, pH 8.0, 1x Roche Protease Inhibitor Cocktail) and mechanically lysed in a Dounce homogenizer. The lysate was spun down at 50,000 × *g* for 1 hr to collect the cell membranes and supernatant was discarded. The pellet was resuspended in solubilization buffer (20 mM Tris pH 7.3, 0.5 M NaCl, 20% Glycerol, 1% dodecyl β-D-maltoside (DDM), 1x protease inhibitor cocktail), homogenized and incubated for 1 hr at 4°C. The solubilized suspension was spun down at 50,000 × *g* for 1 hr to pellet any remaining insoluble material and incubated in Ni-NTA slurry overnight at 4°C. Ni-NTA beads were collected by spinning down solubilized solution at 250 × *g*, washed twice and transferred to a chromatography column before elution with 200 mM imidazole in HBS, 20% glycerol, and 0.1% DDM).

2.4.4 Crystallization

For initial crystal screens, purified proteins were concentrated to at least 10 mg/ml and were added to NeXtaL crystallization screens (Core I suite, Core II suite, Core III suite, Core IV suite, Pro-complex suite, and PACT suite) on a 96-well sitting drop iQ plate (SPT Labtech) using a Mosquito Crystal robot (SPT Labtech) or Crystal Gryphon robot (Art Robbins). Drop sizes were adjusted between 200 nL and 400 nL with protein and crystallization solutions being mixed in a 1:1 ratio with 50 µl crystallant in the reservoir. For optimization of crystals, selected conditions were recreated in 1.5 ml Eppendorf tubes, with small variations in pH, precipitant concentration, or salt concentration. 1 µl of Crystallant and 1 µl of protein were mixed in Chryschem M 24-well round reservoir sitting drop plates (Hampton Research) with 250 µl of crystallant in the reservoir.

2.4.5 Co-immunoprecipitation and Western blot

High Five cells were infected with viruses for His_6- and FLAG-tagged proteins as stated above in 6-well plates. After 72 hours, infected cultures were spun down at 900 × *g* for 5 min and the supernatant was collected. Culture media were mixed in a 1:1 ratio for a total volume of 1 ml and incubated with 25 µl of Ni-NTA resin or 50 µL of anti-DYKDDDDK (FLAG) resin. For Ni-NTA incubations, media was adjusted to pH 7.4 with 10x HBS and 20 mM imidazole was added to reduce nonspecific binding. Ni-NTA incubations were performed with gentle rotation for 1-3 hrs at RT, spun down at 3,000 × *g* for 5 min, washed twice with 20 mM imidazole in HBS, and eluted with 25 µL of 200 mM imidazole in HBS. Anti-FLAG incubations were brought to pH 8.0 with 10x Tris-buffered saline (TBS, 50 mM Tris, 150 mM NaCl, pH 8.0) and rotated gently at RT for 1-3 hrs. Resin was spun down at 3,000 × *g* for 5 min, washed 3x in TBS, and eluted with 50 µL

0.5 mg/ml FLAG peptide in TBS. Eluates were mixed with 6x sodium dodecyl sulfate (SDS) sample buffer, run under SDS-PAGE gel electrophoresis, and blotted onto PVDF membranes using the Power Blotter semi-dry transfer system (Thermo Fisher). Blots were blocked with 4% bovine serum albumin (BSA) in TBST (20 mM Tris, 150 mM NaCl, 0.1% Tween-20) for 1 hr, incubated with either anti-His antibody conjugated to iFluor 488 (GenScript) or anti-DYKDDDDK antibody conjugated to iFluor555 (GenScript) for 1 hr, and washed 15 min 3x with TBST. Imaging of blots was performed using the Bio-Rad ChemiDoc XRS system.

2.4.6 The Extracellular Interactome Assay (ECIA)

SAX-7 and LECT-2 constructs were cloned in to pECIA-prey and pECIA-bait plasmids(Cheng, Ashley, et al. 2019). pECIA plasmids were transfected into S2 cells using Mirus TransIT insect transfection reagent and cultured for 72-96 hrs. Conditioned culture media from pECIA-bait constructs were added to Protein A-coated plates for 3 hrs with vigorous shaking at 500 rpm, followed by blocking with 1% BSA in PBS. Culture media from pECIA-prey transfected cells was added to plates for another 3 hrs with shaking. Prey capture by Bait proteins was visualized through enzymatic conversion of KPL BluePhos substrate , where product was measured by absorbance at 650 nm with a BioTek Synergy H1 plate reader. Expression of constructs was tested by western blot.

CHAPTER 3: ROBOS, NELLS, AND MIDLINE CROSSING

3.1 INTRODUCTION

This chapter includes parts from the published manuscript Pak et al., *Nature Communications* (2020) where I was the first author, and is expanded upon with data that were not included in the paper. Establishing proper neuronal connectivity during embryonic development is critical for formation of a functional nervous system, and guidance of axons to their correct targets is a key step in the assembly of neural circuits. Axon pathfinding is orchestrated by attractive and repulsive molecular cues that activate receptors on the axonal leading process, the growth cone(Kolodkin and Tessier-Lavigne 2011). For example, Netrin-1, acting through its DCC family receptors, promotes axon growth and mediates attraction(Boyer and Gupton 2018); Slit proteins, on the other hand, are prototypical repulsive cues that signal through receptors of the Robo family(Blockus and Chédotal 2016a; Dickson and Gilestro 2006). Many classes of guidance cues and receptors, including Netrin/DCC and Slit/Robo, are conserved across taxa from invertebrates to mammals; however, evolutionary expansion of the relevant gene families and functional specialization of individual family members likely allow wiring of the more complex nervous systems found in higher organisms, including humans(Chisholm and Tessier-Lavigne 1999). The full extent and nature of these modifications to the molecular toolkit for axon guidance remain elusive.

Robo family receptors are type I transmembrane proteins that instruct neuronal wiring in various organisms, including worms, flies, mice, and humans, in addition to fulfilling diverse functions outside the nervous system(Blockus and Chédotal 2016a; Dickson and Gilestro 2006). The N-terminal extracellular domains (ECDs) of neuronally expressed Robos are composed of five immunoglobulin-like (IG) and three fibronectin type III (FN) domains (Figure

12A)(Sundaresan et al. 1998), while the vertebrate-specific family member Robo4, which is not expressed in the nervous system and regulates angiogenesis, contains only two IG and two FN domains(Huminiecki et al. 2002; Yadav and Narayan 2014). The first IG domain (IG1) of neuronal Robos binds to the canonical Robo ligands belonging to the Slit family(Liu et al. 2004; Morlot et al. 2007). Slits are multidomain secreted proteins (Figure 12A)(Rothberg et al. 1990) that interact with Robos through their second leucine-rich repeat (LRR) domain(Howitt, Clout, and Hohenester 2004; Morlot et al. 2007) to mediate axon repulsion, branching, and fasciculation(Blockus and Chédotal 2016a). How Robos are activated by Slits is a topic of contention. There are conflicting reports on whether Slit dimerization plays a role in Robo-mediated downstream effects(Howitt, Clout, and Hohenester 2004; Seiradake et al. 2009; Hohenester 2008), and if the oligomerization state of Robo changes upon Slit binding(Zakrys et al. 2014). A recent study supported a mechanism involving Slit-induced conformational change of preformed Robo dimers to allow repulsive signaling(Aleksandrova et al. 2018), while another manuscript proposed two competing modes of Robo dimer formation, regulated via Slit binding(Barak et al. 2019). A *trans* mode of Robo dimerization to turn off responses to Slit was previously proposed(Evans et al. 2015). Additionally, heparan sulfate binding by Slits are known to modulate Slit-Robo binding and signaling(Hu 2001; Hussain et al. 2006; Fukuhara et al. 2008), but a complete molecular model for the activation of a Slit-Robo-Heparan sulfate complex remains to be established.

In mammals, there are three Slit paralogs (Slit1-Slit3) and three neuronally expressed Robos (Robo1-Robo3). While Robo1 and Robo2 function as classical Slit receptors, the divergent family member Robo3 does not bind Slits and instead acts as a negative regulator of Robo1/2-mediated Slit repulsion(Sabatier et al. 2004; Camurri et al. 2005; Mambetisaeva et al. 2005; Jaworski, Long, and Tessier-Lavigne 2010). Robo3 also indirectly boosts axon attraction to Netrin-

1 without interacting with Netrin-1 itself(Zelina, Blockus, Zagar, Péres, Friocourt, Wu, Rama, Fouquet, Hohenester, Tessier-Lavigne, Schweitzer, Roest Crollius, et al. 2014). Further, a recently identified Robo3 ligand, NELL2, signals axon repulsion(Jaworski et al. 2015). These three non-canonical functions of Robo3 are best understood in the guidance of commissural axons across the midline of the mouse spinal cord and hindbrain, which has long served as a prime model system for studying axon pathfinding mechanisms. The floor plate at the ventral midline expresses Netrin-1 and Slit1/2/3, while NELL2 is expressed in regions flanking the commissural axon trajectory, including the ventral horn(Brose et al. 1999; Kennedy et al. 1994; Jaworski et al. 2015). In commissural neurons, Robo3 exists in two splice isoforms that differ at the C-termini of their intracellular domains (ICDs): Robo3.1 is expressed before midline crossing, and Robo3.2 is expressed on postcrossing axons(Z. Chen et al. 2008). Robo3.1 appears to facilitate midline crossing by preventing premature Slit repulsion from the floor plate, promoting Netrin-1-induced growth to the midline, and mediating NELL2 repulsion from the ventral horn, while Robo3.2 promotes midline exit after crossing through unknown mechanisms(Z. Chen et al. 2008; Jaworski et al. 2015; Sabatier et al. 2004; Zelina, Blockus, Zagar, Péres, Friocourt, Wu, Rama, Fouquet, Hohenester, Tessier-Lavigne, Schweitzer, Roest Crollius, et al. 2014). Consequently, in mice lacking *Robo3*, all commissural axons fail to reach the floor plate and instead project through the ipsilateral ventral horn(Jaworski et al. 2015; Sabatier et al. 2004). This crucial role of Robo3 as a signaling hub in midline guidance is conserved in humans, as midline crossing defects are seen in patients with *ROBO3* mutations, who exhibit Horizontal Gaze Palsy with Progressive Scoliosis(Jen et al. 2004). Even though Robo3 is required to mediate NELL2 repulsion in commissural axons and both Robo3.1 and Robo3.2 bind NELL2, only precrossing, not postcrossing, axons are repelled by NELL2(Jaworski et al. 2015). It has remained unclear whether

this differential NELL2 responsiveness reflects distinct signaling capabilities of Robo3.1 and Robo3.2 or other differences between pre- and postcrossing axons.

NELL2 is a secreted glycoprotein containing a laminin G-like (LamG) domain, a coiled coil (CC) domain, and six epidermal growth factor-like (EGF) domains, flanked by five von Willebrand factor type C (VWC) domains (Figure 12A)(Kuroda et al. 1999; Matsuhashi et al. 1995; Watanabe et al. 1996). The interaction between NELL2 and Robo3 maps to the EGF domains in NELL2 and the FN domains in Robo3(Jaworski et al. 2015). In addition to commissural axon guidance, NELL2 controls retinal ganglion cell wiring(Jiang et al. 2009; Nakamoto et al. 2019), and it is expressed in various regions of the developing nervous system(Kim et al. 2002; Matsuhashi et al. 1995; Nelson, Matsuhashi, and Lefcort 2002). The additional mammalian NELL family member, NELL1, also binds Robo3, but it is not expressed in the spinal cord and has little or no repulsive activity for commissural axons(Jaworski et al. 2015). Instead, NELL1 has been implicated in osteogenesis through as yet unidentified mechanisms(Desai et al. 2006). While NELLs bind Robo3, they do not strongly interact with full-length Robo1/2(Jaworski et al. 2015). The exact nature of the NELL1/2-Robo3 complex interface, the basis of the different Robo1/2 and Robo3 ligand binding specificities, and the mechanism of NELL2-dependent Robo3 activation for axon repulsion are unknown.

Here, we investigate NELL-Robo3 complex signaling in axon guidance. We identify Robo3.1 as the only neuronal Robo that can function as a NELL receptor for commissural axon repulsion. Further, we show that NELL1/2-Robo3 binding is mediated by the combined interaction of NELL EGF2 and EGF3 domains with the Robo3 FN1 domain, and we report the crystal structures of NELL1-Robo3 and NELL2-Robo3 complexes. We demonstrate that reducing NELL2 affinity for Robo3 decreases its axon guidance activity, while NELL1 possesses axon repulsive activity orders of magnitude lower than NELL2 despite comparable Robo3 affinities. We also find that divergence of the FN1 domain between Robo family members underlies their different NELL affinities and signaling capabilities, while conformational variability in the Robo ECDs further regulates accessibility of the NELL binding site. These findings are consistent with recently published manuscripts showing a cryptic NELL binding site on Robo2(Yamamoto et al. 2019), possibly occluded by a hairpin-like conformation observed in the Robo2 ECD(Barak et al. 2019). Lastly, we show that NELL-mediated oligomerization of Robo3 monomers is a strong contributor to NELL-Robo3 signaling and axon repulsion. Together, these findings expand on models of Robo activation by guidance cues and indicate that mammalian Robo3 underwent evolutionary specialization in terms of its ligand binding specificity, conformational landscape, and oligomerization state for activation and signaling.

3.2 RESULTS

3.2.1 The Robo3.1 splice variant mediates NELL2 axon repulsion

Commissural axons express the Robo3 splice variant Robo3.1 exclusively before midline crossing and replace this isoform with Robo3.2 after crossing(Z. Chen et al. 2008). Even though both isoforms can bind NELL2, only precrossing commissural axons are repelled by NELL2, but postcrossing axons are not, thereby mirroring the mutually exclusive presence of Robo3.1 and Robo3.2(Jaworski et al. 2015). We revisited the roles of the two Robo3 splice isoforms in NELL2 signaling. We first examined the relationship of precrossing axons and the NELL2 protein expression domain in mouse embryonic day 9.75 (E9.75) spinal cord sections by immunohistochemistry and found that the first Robo3-expressing axons extend toward the midline by precisely circumnavigating a sharply delineated NELL2-positive region in the ventral horn (Figure 12B). This result indicates that NELL2 forms a very steep gradient in the neural tube and

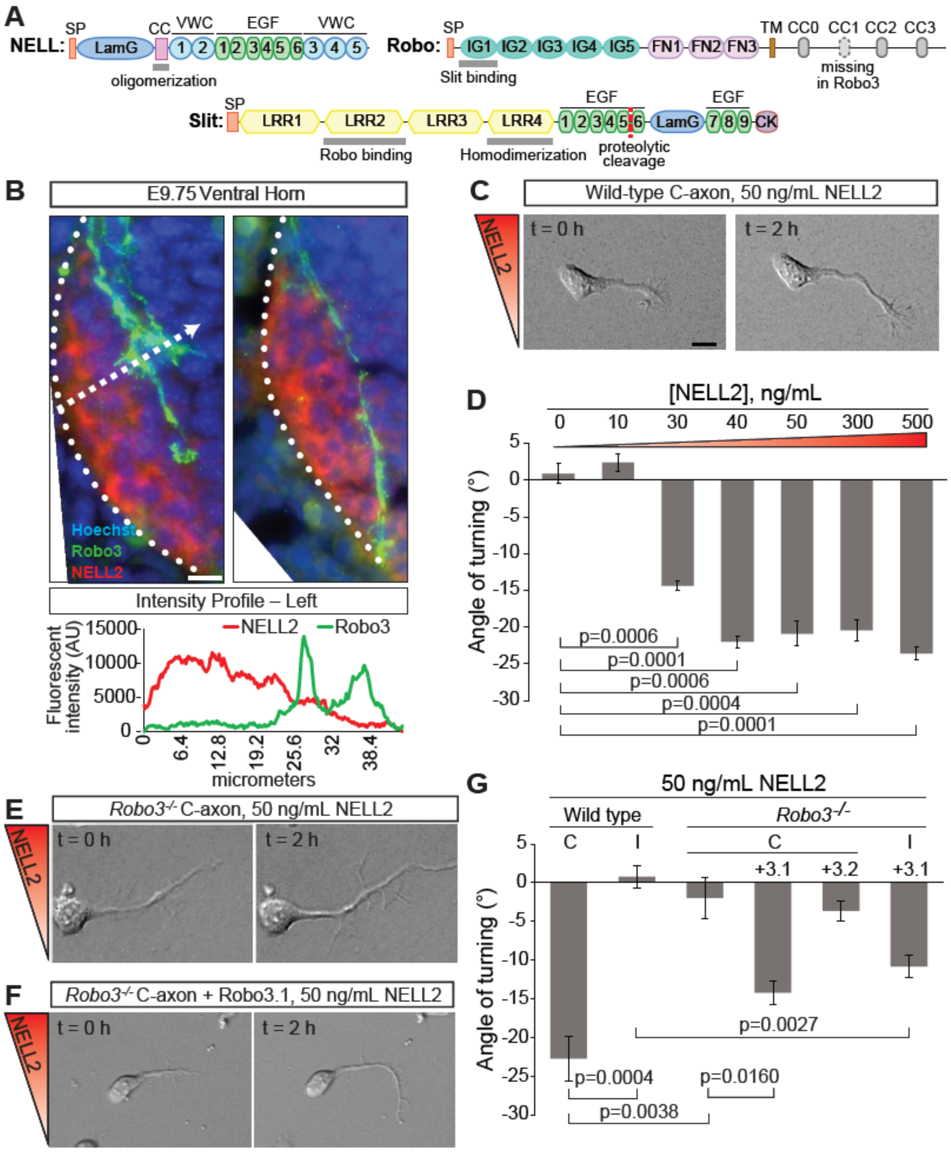

Figure 12: Robo3.1 is necessary and sufficient for axon repulsion from NELL2.

(**A**) Domain structure of NELLs, Robos and Slits, drawn true to scale for human NELL2, Robo3 and Slit1. CC with numbers indicate conserved cytoplasmic motifs. SP: signal peptide. TM: transmembrane helix. CK: C-terminal cysteine knot. (**B**) Transverse spinal cord sections from E9.75 mouse embryos were labeled with Hoechst stain and antibodies against Robo3 and NELL2. Robo3-expressing precrossing commissural axons grow around areas of NELL2 expression in the ventral horn. Dotted line indicates spinal cord border. Fluorescence intensity profile (bottom) was generated by line scan along the dashed arrow. **(C)** DIC images of a commissural axon turning away from a gradient of NELL2 in a Dunn chamber (0 h and 2 h). **(D)** Quantification of commissural axon turning angles for increasing concentrations of NELL2 (n = 3 independent experiments for all conditions). **(E,F)** DIC images of *Robo3*$^{-/-}$ neurons in a NELL2 gradient. *Robo3*$^{-/-}$ axons do not turn in response to NELL2 (E), unless rescued with Robo3.1 (F). **(G)** Quantification of turning angles in response to NELL2 for commissural (labeled C) axons (wild-type or *Robo3*$^{-/-}$ with or without Robo3.1 or Robo3.2 rescue) or ipsilateral (labeled I) axons (n = 3 for all conditions). Scale bar, 10 µm (B,C,E,F). Error bars indicate SEM.

supports the idea that Robo3.1-mediated NELL2 repulsion steers precrossing pioneer axons along the border formed by this gradient.

To directly test the roles of Robo3.1 and Robo3.2 in axon guidance by NELL2, we examined these isoforms for their ability to mediate NELL2 repulsion *in vitro*. The graduate student Zachary DeLoughery working under the supervision of Dr. Alexander Jaworski at Brown University adapted Dunn chamber axon turning assays(Yam et al. 2009) to study responses of E11.5 mouse dorsal spinal cord neurons to gradients of NELL2 and found that NELL2 induces robust repulsion of Robo3.1-positive precrossing commissural axons that plateaus at a peak concentration of 40 ng/ml (Figure 12C-D). Ipsilaterally projecting neurons, which do not express Robo3(Sabatier et al. 2004), and commissural neurons from *Robo3*$^{-/-}$ embryos do not respond to NELL2 (Figure 12E and G). When we reintroduced either Robo3.1 or Robo3.2 into *Robo3*$^{-/-}$ commissural neurons via cDNA electroporation, we found that only Robo3.1 can restore NELL2-dependent axon repulsion (Figure 12F-G), even though both isoforms are expressed on the growth cone surface after electroporation. Further, forced Robo3.1 expression in ipsilaterally projecting neurons also induces NELL2-dependent axon repulsion in these normally NELL2-unresponsive cells (Figure 12G). Thus, Robo3.1 is both necessary and sufficient for NELL2-induced axon repulsion in dorsal spinal cord neurons, while Robo3.2 cannot mediate NELL2 signaling. The Robo3.1 isoform was therefore selected for additional functional studies.

3.2.2 NELL2 EGF DOMAINS 2 AND 3 BIND THE ROBO3 FN1 DOMAIN

We have previously shown that the EGF domains of NELL2 and the FN domains of Robo3 are sufficient for binding(Jaworski et al. 2015). To understand how the NELL2-Robo3 complex forms, we further mapped the domains necessary for the ligand-receptor interaction. Binding of human (h) NELL2-alkaline phosphatase (AP) fusions to hRobo3.1-expressing COS-7 cells revealed that NELL2 EGF2 and EGF3 together, but not in isolation, bind Robo3 FN1, but not any of the other Robo3 FN domains (Figure 13A-B). NELL2-Robo3 binding is therefore mediated by NELL2 EGF2/3 and Robo3 FN1.

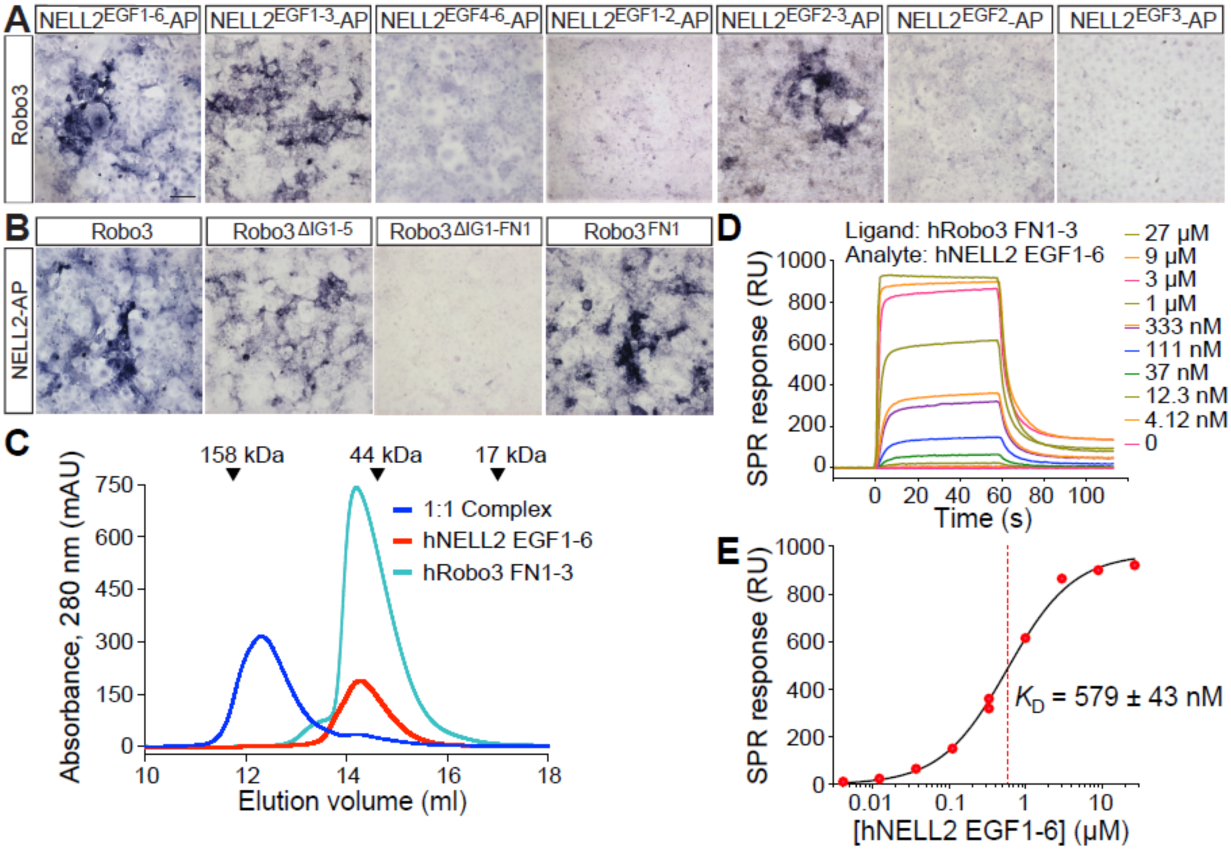

Figure 13: NELL2 EGF2-3 bind Robo3 FN1 to mediate complex formation.
(**A,B**) Domains mediating NELL2-Robo3 interactions were mapped using a COS-7-based AP fusion protein binding assay. NELL2 EGF2 and EGF3 together are necessary and sufficient for binding to Robo3 (A). Robo3 FN1 is necessary and sufficient for NELL2 binding (B). (**C**) Size-exclusion chromatography of the hNELL2 EGF1-6 and hRobo3 FN1-3 complex. hNELL2 EGF1-6, hRobo3 FN1-3, and a molar 1:1 mixed complex samples were injected in a Superdex 200 Increase 10/300 column, and the elution profile was recorded by following absorbance at 280 nm with a pathlength of 0.2 cm. Dark blue: hNELL2 EGF1-6 + hRobo3 FN1-3 complex sample; Cyan: hRobo3 FN1-3; and Red: hNELL2 EGF1-6. AU: Absorbance units. (**D,E**) SPR sensorgrams (D) and equilibrium response fitting to a Langmuir 1:1 binding model (E) for biotinylated hRobo3 FN1-3 as ligand on an NLC/neutravidin chip with hNELL2 EGF1-6 as the analyte (mobile phase) collected on a ProteOn XPR36. Legend on the right in (D) refers to concentration of the analyte injected on the SPR chip. Black curve in (E) is the Langmuir model fit to response values measured at equilibrium. ± refers to standard error of the fit. Scale bar, 100 μm, (A, B).

We next set out to determine the structure of NELL2 in complex with Robo3. Using constructs that include the hNELL2 EGF domains 1 to 6 and the hRobo3 FN domains 1 to 3, we obtained a stable complex of these molecules, as demonstrated by size-exclusion chromatography (SEC) (Figure 13C). Surface plasmon resonance (SPR) analysis of this complex yielded a dissociation constant of 0.6 μM (Figure 13D-E). We crystallized a complex of NELL2 EGF1-6 with Robo3 FN1, and Robo3 FN2-3 alone, following proteolysis within the 15-residue-long flexible linker between FN1 and FN2 in crystallization drops. The NELL2-Robo3 complex structure was determined by an MR-SAD phasing strategy to 2.76-Å resolution (

Table ***1***). The structure shows direct binding between the NELL2 EGF2 and EGF3 domains and the Robo3 FN1 domain (Figure 14A), consistent with our domain mapping data (Figure 13A-B). The two EGF domains wrap around the FN domain and interact with the β-sheet composed of the CDFG strands (Figure 14A). To our knowledge, this mode of interaction between EGF and FN domains has not been observed before. Netrin EGF domains and DCC FN domains adopt entirely different geometries in their complexes, and the NELL2-Robo3 complex therefore exhibits no structural similarity to and shares no common ancestry with the Netrin-DCC complex. We also determined the crystal structure of hRobo3 FN2-3, which showed two linearly extended FN domains with no unexpected features for the FN fold.

In the crystal structure of the NELL2-Robo3 complex, we observed electron density for three calcium ions bound to the EGF2, EGF5, and EGF6 domains. The calcium coordination sites are conserved among vertebrate and invertebrate NELL sequences. Since we did not include calcium in our purification and crystallization buffers, these calcium ions must be held tightly by the EGF domains. The electron density also showed one O-linked glycan residue on the NELL2

EGF4 domain in a motif known to be recognized by a dedicated transferase in several signaling and matrix EGF domain proteins, including Notch and NELL1(Alfaro et al. 2012; Ogawa et al. 2018), raising the possibility of shared origins or adopted functions for NELLs and Notch.

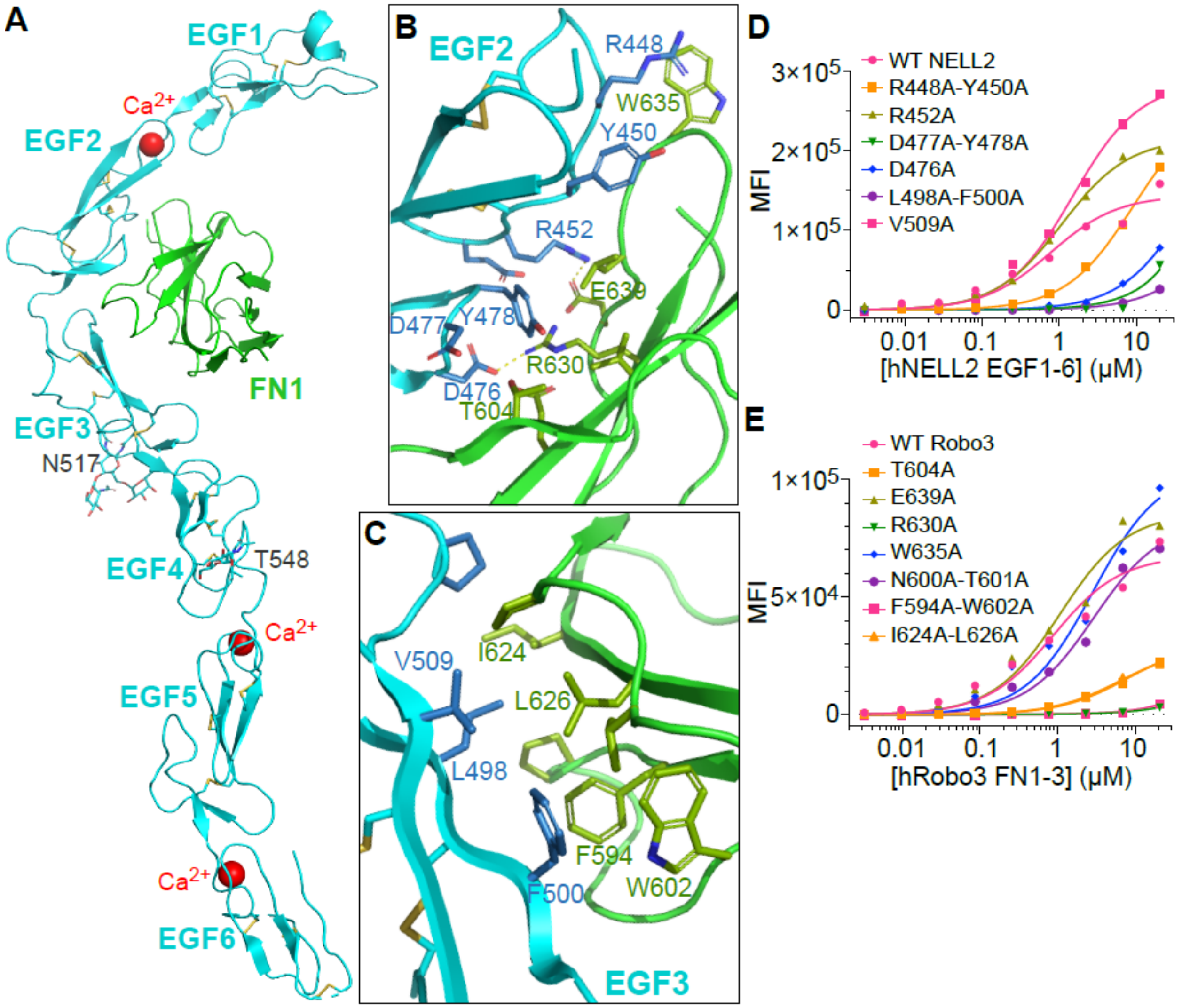

Figure 14: Crystal structure of the NELL2-Robo3 complex.
(**A**) The structure of hRobo3 (cyan) bound to hNELL2 (green). The three calcium ions are depicted as balls; the two glycan moeities and the side chains they are linked to are shown as sticks. (**B**) Interactions of the EGF2 domain with Robo3 are dominated by polar contacts. (**C**) Interactions of the EGF3 domain with Robo3 are exclusively hydrophobic. (**D**) Binding isotherms for biotinylated wild-type and mutant hNELL2 EGF1-6 measured against S2 cells expressing hRobo3 FN1-3. *y*-axis represents mean fluorescence intensity (MFI) from fluorescent streptavidin. (**E**) Binding isotherms for biotinylated wild-type and mutant hRobo3 FN1 measured against S2 cells expressing cells hNELL2 EGF1-6.

Table 1, related to Figure 14: Crystal structure of the NELL2-Robo3 complex. Data and refinement statistics for x-ray crystallography.

	hRobo3 FNIII 1 + hNELL2 EGF 1-6	**hRobo3 FNIII 2-3**	**hRobo3 FNIII 1 + hNELL1 EGF 1-3**
Data Collection			
Space Group	$P2_12_12_1$	$P2_1$	$P3_121$
Cell Dimensions			
a, b, c (Å)	41.87, 90.44, 171.58	54.99, 36.61, 64.90	87.00, 87.00, 211.30
α, β, γ (°)	90, 90, 90	90, 114.44, 90	90, 90, 120
Resolution (Å)	50-2.76 (2.92-2.76)*	55-1.80 (1.91-1.80)	55-1.80 (1.85-1.80)
R_{sym} (%)	10.6 (159.9)	6.6 (86.0)	23.8 (205.3)
$<I>/<\sigma(I)>$	10.53 (0.81)	6.59 (0.79)	5.75 (0.72)
$CC_{1/2}$	99.8 (43.0)	99.6 (58.6)	99.6 (46.5)
Completeness (%)	99.4 (96.9)	99.7 (98.1)	99.6 (95.9)
Redundancy	6.4 (6.5)	1.8 (1.6)	13.0 (6.2)
Refinement			
Resolution (Å)	50-2.76 (2.87-2.76)*	50.1-1.80 (1.88-1.80)	51.45-1.80 (1.85-1.80)
Reflections	17,498	21,770	85,786
R_{cryst} (%)	23.68 (35.27)	21.73 (42.14)	22.99 (53.83)
R_{free} (%)***	26.37 (36.00)	24.31 (41.09)	26.64 (52.77)
Number of atoms			
Protein	2392	1474	5141
Ligand/Glycans	55	6	113
Water	N/A	138	642
Average B-factors (Å^2)			
All	122.7	48.8	45.3
Protein	122.1	49.2	44.5
Ligand/Glycans	150.0	73.5	64.3
Solvent	N/A	43.8	48.2
R.m.s. deviations from ideality			
Bond Lengths (Å)	0.003	0.002	0.007
Bond Angles (°)	0.594	0.531	0.867
Ramachandran statistics			
Favored (%)	89.06	97.92	96.46
Outliers (%)	0.30	0	0
Rotamer Outliers (%)	3.57	0.63	0.35
All-atom Clashscore ‡	3.75	3.37	1.79
Coordinate Error § (Å)	0.44	0.28	0.30

* The values in parentheses are for reflections in the highest resolution bin.

** 7.5% (1315), 5.0 (1083) and 2.3% (1985) of reflections were not used during refinement for cross validation.

3.2.3 NELL2-Robo3 affinity dictates axon repulsion from NELL2

The human NELL2-Robo3 complex structure displays a surprising partitioning of the overall binding interface into a highly polar interface at the EGF2-FN1 contact (Figure 14B), and an entirely hydrophobic interface at the EGF3-FN1 contact (Figure 14C). To confirm the crystallographically observed complex structure, we engineered single- and double-point interface mutants of hNELL2 EGF1-6 and hRobo3 FN1-3 and tested them for binding in flow cytometry-based cell staining assays. Several mutations nearly abolish binding, while many others yield diminished binding activities, confirming the validity of the crystallographic model (Figure 14D-E). Cell staining results were further corroborated using the high-throughput, ELISA-like extracellular interactome assay (ECIA). To be able to test the functional effects of these mutations in an experimental setting using analysis of mouse (m) NELL2 EGF1-6 and Robo3 FN1-3 (Figure 15A-B). The binding results for mouse commissural neurons, we also measured affinities of NELL2 interface mutants by SPR mouse and human NELL2 and Robo3 using three different methods are in full agreement and confirm the structural model of the complex in solution.

To assess the necessity of the NELL2-Robo3 interface for NELL2-mediated axon repulsion, we tested the guidance activity of mNELL2 point mutants using the Dunn chamber axon guidance assay (Figure 15C-E). We found that mutants with mildly (2.4-fold) reduced mRobo3 affinity (V509A and R452A) repel commissural axons as strongly as wild-type mNELL2 (Figure 15C and E). The R448A/Y450A double mutant, which weakened affinity by 120-fold, exhibits significantly reduced repulsive activity, while the L498A/F500A double mutant with 500-fold loss of binding fails to effect any detectable axon repulsion (Figure 15D-E). Thus, the affinity of the NELL2-Robo3 interaction determines NELL2 axon guidance activity.

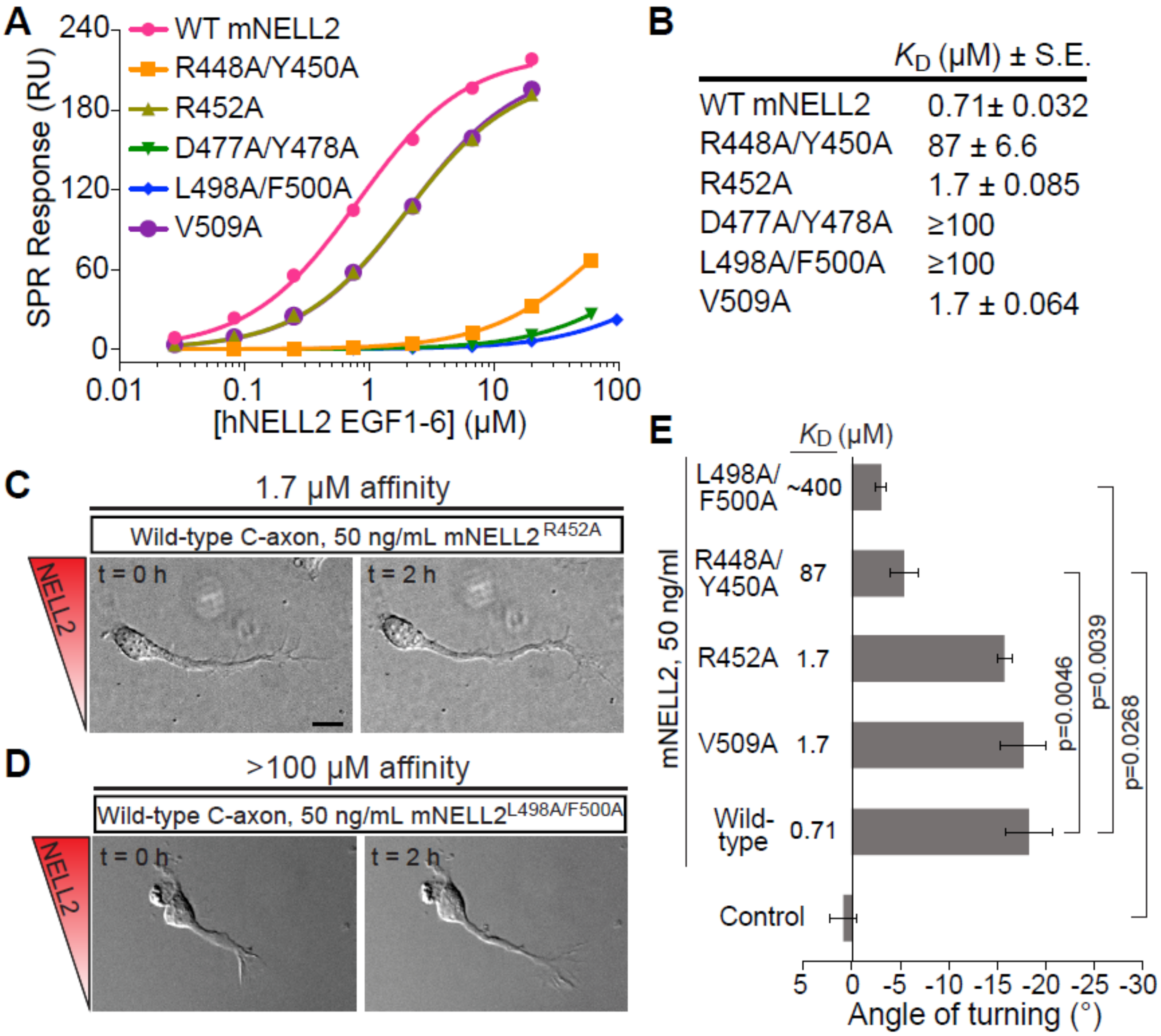

	K_D (μM) ± S.E.
WT mNELL2	0.71± 0.032
R448A/Y450A	87 ± 6.6
R452A	1.7 ± 0.085
D477A/Y478A	≥100
L498A/F500A	≥100
V509A	1.7 ± 0.064

Figure 15 Axon repulsive activity of NELL2 correlates with its affinity towards Robo3.

(A,B) Binding isotherms (A) for SPR experiments testing the interaction of mRobo3 FN1-3 with mNELL2 EGF1-6 WT and mutants. SPR responses are fit with 1:1 Langmuir isotherm model to calculate dissociation constants (K_D) (B). The ± errors represent standard error of the fit. (C,D) DIC images of commissural axons exposed to mutant forms of NELL2 with Robo3-binding affinities of 1.7 μM (C) and ≥100 μM (D) (0 h and 2 h). Commissural axons respond to NELL2 mutants with 1.7 μM binding affinity, but not with ≥100 μM affinity. (E) Quantification of commissural axon turning angles in response to wild-type NELL2 or NELL2 containing point mutations (n = 3 for WT NELL2, R452A, and L498A/F500A; n = 4 for R448A/Y450A; n = 5 for V509A). K_D values are dissociation constants measured for mNELL2 mutants via SPR (B). Scale bar, 10 μm (C, D).

3.2.4 NELL1 binds Robo3 and has weak axon repulsive activity

NELL1 can bind Robo3, but it does not mediate strong commissural axon repulsion *in vitro*(Jaworski et al. 2015). How NELL1 affinity for Robo3 relates to its guidance activity, has remained elusive. Using SEC, we isolated a hNELL1 EGF1-3-hRobo3 FN1 complex. We crystallized and determined the structure of this complex at 1.8-Å resolution using molecular replacement with the NELL2-Robo3 model. The NELL1-Robo3 structure is highly similar to the NELL2-Robo3 complex, indicated by a root-mean square deviation of only 1.39 Å over all 225 Cα atoms in the EGF1-3 and FN1 domains (Figure 16A). Using SPR, we found that hNELL1 and hNELL2 EGF1-3 domains have comparable affinities for the hRobo3 FN1-3 domains. Further, the interacting residues identified at the Robo3 interfaces for NELL1 and NELL2 are conserved among chordate NELL sequences, but not in protostome NELLs (Figure 16B), which raises the possibility that invertebrate NELLs may not interact with Robos.

NELL1 EGF2 also has a calcium ion bound (Figure 16A) at the conserved site observed for NELL2. The calcium ion is not directly located at the Robo3 binding site but is still within 11 Å of the closest Robo3 atom. Therefore, we examined NELL EGF1-3 binding to Robo3 FN1-3 with calcium chelation by EDTA, which only caused a modest (3- to 6-fold) reduction of Robo3 affinity for both NELL1 and NELL2. Taken together, these results indicate that NELL1 and NELL2 display no significant biochemical differences in Robo3 recognition.

Given the similarities in NELL1 and NELL2 domain structures and Robo3 recognition, we revisited the ability of NELL1 to repel axons. We investigated commissural axon responses to NELL1 *in vitro* and found that, at a peak concentration of 50 ng/ml, which produces maximum axon repulsion from NELL2 (Figure 12D), NELL1 does not cause a turning response (Figure 16C). Weak repulsion was observed with 250 ng/ml NELL1, and maximum axon turning occurs between

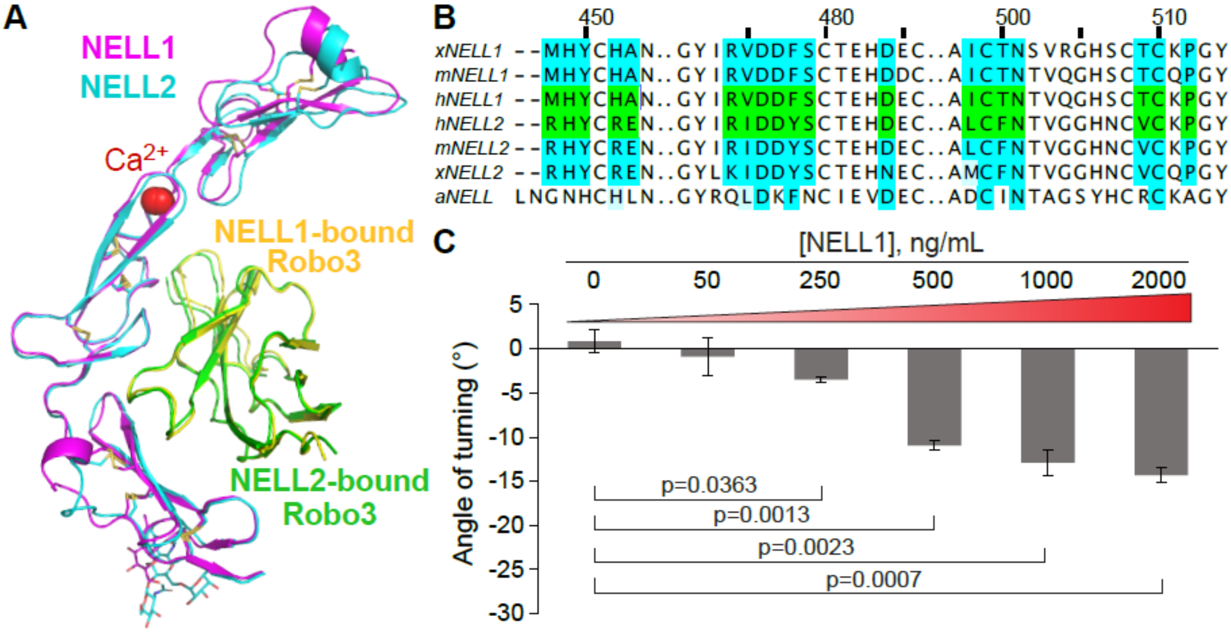

Figure 16: Axon repulsive activities and interactions of NELL family members with Robo3 are conserved to varying degrees.

(**A**) Crystal structure of hRobo3 FN1 bound to hNELL1 EGF1-3 (purple and yellow), overlaid with the hRobo3/hNELL2 structure (cyan and green). (**B**) Partial alignment of NELL sequences from *Xenopus laevis* (*x*), mouse (*m*), human (*h*), and the arthropod *Aedes aegypti* (*a*). Green squares indicate NELL residues at the Robo3-binding interface, which are highly conserved, except in aNELL. Blue positions are identical to human NELL1 or NELL2, while light blue represents conservative substitutions. (**C**) Quantification of commissural axon turning angles for increasing concentrations of NELL1 (n = 3 for all conditions). Error Bars represent SEM.

1 µg/ml and 2 µg/ml (Figure 16C), but the magnitude of this response never reaches the level seen with NELL2 (compare Figure 12D and Figure 16C). Overall, our results indicate that NELL1 can signal through Robo3 as its receptor to induce commissural axon repulsion, albeit less effectively than NELL2. To understand why NELL1 and NELL2 have different guidance activities despite the comparable affinities of their EGF1-3 domains for Robo3, we created chimeras in which the EGF1-3 domains were swapped between mNELL1 and mNELL2. Both chimeric proteins can interact with the Robo3 FN1-3 domains. We examined the axon guidance activity of these chimeric NELLs and found that NELL1 containing NELL2 EGF1-3 (NELL1$^{\text{NELL2-EGF1-3}}$) repels

commissural axons at 50 ng/ml, although not as strongly as NELL2, while NELL2 containing NELL1 EGF1-3 ($\text{NELL2}^{\text{NELL1-EGF1-3}}$) is not a potent axon repulsive cue at this concentration (Figure 16D). These results implicate the EGF1-3 domains as the major determining elements for differential axon repulsion activity of NELL1 and NELL2, despite the fact that we observed no significant differences in Robo3 affinities for the NELL1 and NELL2 EGF domains.

3.2.5 Robo1 weakly interacts with NELL2

While Robo3.1 is necessary and sufficient for NELL2-mediated axon repulsion (Figure 12E-G), Robo1 and Robo2 are not required for NELL2 signaling in commissural axons(Jaworski et al. 2015). If Robo-NELL interactions depend on the FN1 domain of Robos, we expect that the sequence of FN1 determines which Robos can function as NELL receptors. Surprisingly, the energetic hot spots for NELL2 binding on the hRobo3 interface, R630, F594/W602 and I624/L626 (Figure 14D-E), are conserved in both the Robo1 and the Robo2 FN1 domains (Figure 17A), suggesting that Robo1 and Robo2 may interact with NELLs. We were indeed able to detect weak binding activity using highly sensitive methods, SPR and ECIA, between the hRobo1 ectodomain and full-length hNELL2 with a $K_D \approx 350$ μM (Figure 17B-C). Thus, Robo1 binds NELL2 with about three orders of magnitude lower affinity than Robo3. As expected, this weak interaction is mediated by the same domains and amino acids as Robo3-NELL2 binding (Figure 17C-D). Interestingly, in isolation, Robo1 FN1-3 exhibits stronger binding to mNELL2 EGF1-6 (K_D = ***14*** μM) (Figure 17E-F), suggesting steric occlusion of the binding interface in full-length complexes. It should be noted, however, that even this increased, unmasked affinity between NELL2 and Robo1 is more than one order of magnitude weaker than the NELL2-Robo3 affinity, and binding might therefore not be sufficiently strong to effect NELL2 signaling in a physiological context. Overall, our results support a model of open vs. closed conformational states in full-length Robo1.

Furthermore, the ability of NELLs to bind to multiple mammalian Robos supports the idea that an ancestral Robo in the deuterostome lineage may have been a high-affinity receptor for both Slits and NELLs.

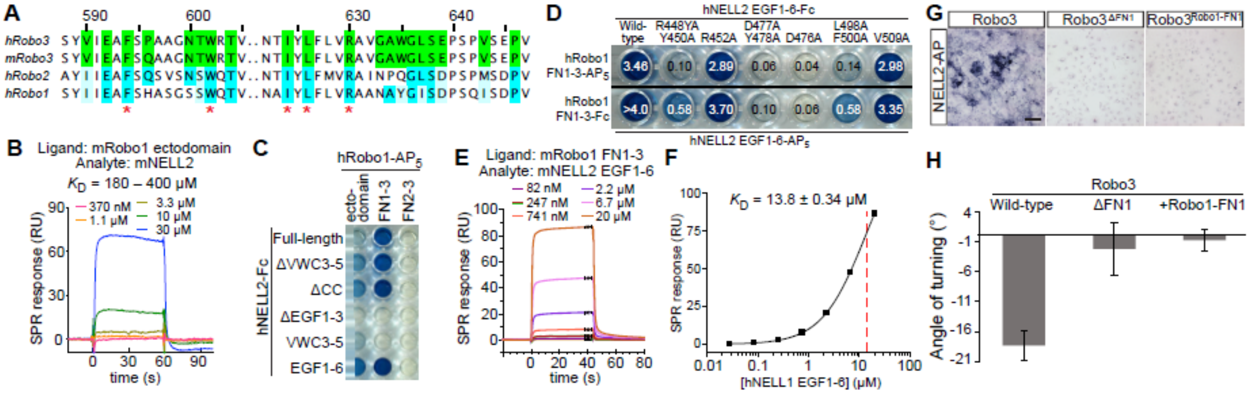

Figure 17: Robo1 interacts weakly with NELL2.

(**A**) Partial alignment of Robo sequences. Green squares indicate Robo3 residues at the NELL2-binding interface. Blue positions are identical in Robo1 and Robo2, while light blue represents conservative substitutions. (**B**) Surface plasmon resonance sensorgrams for the mRobo1 ectodomain-mNELL2 interaction. Expected maximal response is ~1,100 RU. (**C**) ECIA results for hRobo1 and hNELL2 show that FN1 and the EGF1-3 are necessary for the interaction. (**D**) ECIA results for Robo1 binding to NELL2 mutants designed at the Robo3-interaction interface. (**E**) Surface plasmon resonance sensorgrams for the mRobo1 FN1-3-mNELL2 EGF1-6 interaction. (**F**) Langmuir binding isotherm for (E). Dashed red line indicate the dissociation constant, K_D. Calculated R_{max} is 143 R.U. The fit to the isotherm is reliable given a theoretical R_{max} of 218 R.U. assuming a 100% active chip surface. (**G**) NELL2-AP-binding assay with cells expressing Robo3.1, Robo3$^{\Delta FN1}$, or Robo3$^{Robo1\text{-}FN1}$. (**H**) Quantification of turning angles in response to NELL2 for *Robo3*$^{-/-}$ commissural axons rescued with wild-type Robo3.1, Robo3$^{\Delta FN1}$, or Robo3$^{Robo1\text{-}FN1}$ (n = 3 for all conditions). Scale bar, 100 µm (G). Error bars indicate SEM.

To further test the centrality of the Robo FN1 domain for recognizing NELL2 as a ligand, we created a mutant form of mRobo3.1 lacking FN1 (Robo3$^{\Delta FN1}$) and a chimeric version containing mRobo1's FN1 in place of its own (Robo3$^{Robo1\text{-}FN1}$). Using NELL2-AP-binding assays, we found that both of these molecules fail to strongly interact with NELL2 (Figure 17G), confirming the necessity of the Robo3 FN1 domain for high-affinity ligand binding. When we tested the activity of these mutant forms of Robo3 in NELL2-mediated axon guidance, we found that neither variant can rescue NELL2-induced axon turning of *Robo3*$^{-/-}$ commissural neurons *in vitro* (Figure 17H), further establishing importance of the Robo3 FN1 domain for NELL2 repulsive signaling. These results support the idea that evolutionary divergence of Robo3's and Robo1/2's FN1 domains was a key step in Robo3's specialization as a functional NELL2 receptor.

3.2.6 Robo3 ECD is monomeric and assumes an open conformation

Signaling by many type I transmembrane proteins, including Robo1, depends on receptor and ligand oligomeric states. Recent reports suggest that the Slit-binding paralogs, Robo1 and Robo2, may be dimers or compact tetramers(Aleksandrova et al. 2018; Yom-Tov et al. 2017). Using analytical ultracentrifugation (AUC) and SEC, we confirmed that the Robo1 ectodomain exists primarily as a dimer, but in equilibrium with monomer and higher-order oligomers, while Robo3 ECD stays mostly monomeric at similar concentrations (Figure 18A-B). The predominantly monomeric nature of Robo3 was further upheld using multi-angle light scattering (MALS) experiments, and small-angle X-ray scattering (SAXS) experiments show fully extended Robo3 ectodomain monomers (Figure 18C).

Overall, our results show that Robo1 (1) is an oligomer when unliganded, and (2) prefers a conformation where the NELL-binding site is occluded (a closed state). We designed a Robo construct where the FN1 domain from the predominantly open, monomeric mRobo3 was installed in mRobo1. This chimeric construct, mRobo1$^{\text{Robo3-FN1}}$, behaved as a pure monomer with an elution volume larger than both mRobo1 and mRobo3 in SEC experiments. This smaller apparent size is not due to compaction of mRobo1$^{\text{Robo3-FN1}}$, as it still appears as a highly elongated molecule in SAXS experiments, as also observed for Robo1 and Robo3. When we measured binding of mNELL2 to mRobo1$^{\text{Robo3-FN1}}$, we observed NELL2 affinity comparable to, if not slightly stronger than that of mRobo3. These biophysical observations indicate that the FN1 domain can dictate both the oligomeric state and open vs. closed conformation of Robos with regards to the NELL binding interface.

3.2.7 NELL2 trimerization promotes its repulsive activity

Slits may exist as dimers(Howitt, Clout, and Hohenester 2004; Seiradake et al. 2009). For a comparison of the two Robo ligands, we investigated the oligomeric state of NELLs. NELLs had been reported to trimerize via disulfide linkages within or near their CC domain, as detected using non-reducing, denaturing polyacrylamide gels(Kuroda et al. 1999; Nakamura et al. 2014), but the oligomeric states of folded NELLs in solution had not been characterized before. Using a combination of SAXS and MALS experiments, we determined that both NELL1 and NELL2 are trimers in solution (Figure 18D). As expected, deletion of the CC region with its four cysteines (NELL2$^{\Delta CC}$) monomerizes NELL2 on non-reducing denaturing gels and in SEC experiments.

In order to confirm that trimeric NELL2 can simultaneously bind three Robo3 molecules, we purified a complex of full-length mNELL2 and the mRobo3 FN1 domain via SEC. The observed elution volume of this complex is indeed consistent with 3:3 stoichiometry, and quantitative western blots show equimolar binding of NELL2 and Robo3, making a 3:1 stoichiometry very unlikely. We therefore hypothesized that the axon guidance activity of Robo3.1 may depend on NELL2-mediated oligomerization. To test this, we measured commissural axon turning in response to NELL2$^{\Delta CC}$. While there is residual activity, NELL2$^{\Delta CC}$ is severely impaired in its ability to elicit axon repulsion (Figure 18E-F). We confirmed that the ΔCC construct binds Robo3 FN1-3 with similar affinity as wild-type NELL2, indicating that the CC region does not contribute to NELL2-mediated repulsion via direct interactions with Robo3. Together, these results support the theory that ligand-mediated receptor oligomerization strongly potentiates NELL2-Robo3 signaling for axon repulsion. Finally, we checked if binding of NELL2 causes large

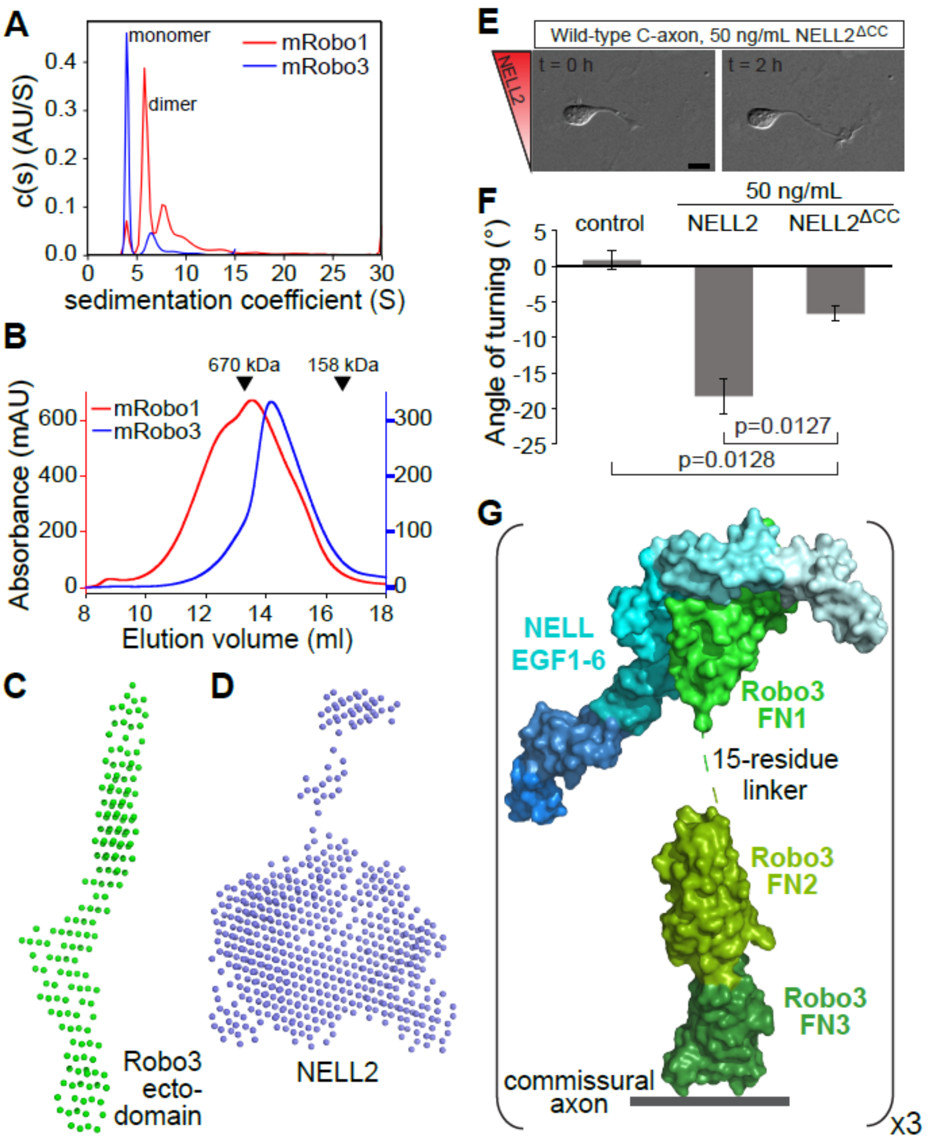

Figure 18: NELL2 trimers signal through multimerization of Robo3 monomers. (**A,B**) Sedimentation velocity (SV) AUC (A) and SEC (B) show that mRobo1 ectodomain is mostly dimeric (red urves), while mRobo3 ectodomain is a monomer (blue curves). Single-concentration SV runs (A) were performed with 2.5 μM Robo1 and 1.8 μM Robo3. (**C,D**) Bead models calculated from SAXS data indicate a fully extended shape for Robo3 (C), while NELL2 is a more compact trimer (D). Pair distance distribution ($P(r)$) analysis is in agreement with the extended shape of Robo3. (**E**) DIC images of commissural axons exposed to wild-type NELL2 or NELL2$^{\Delta CC}$ (0 h and 2 h). (**F**) Quantification of axon turning angles in response to NELL2 and NELL2$^{\Delta CC}$ (n = 3 for all conditions). NELL2$^{\Delta CC}$ repels axons to a lesser degree than wild-type NELL2. (**G**) A model for the three juxtamembrane FN domains of Robo3 capturing NELLs, based on our crystal structures. The linker between FN1 and FN2 domains of Robo3 is degradation sensitive and might be flexible, as opposed to the Robo2 FN1-FN2 linker. Scale bar, 10 μm (E). Error bars represent SEM.

conformational changes in Robo3. Pair distance distribution of mRobo3 ECD with and without mNELL2 EGF1-6 bound show little shape difference, providing evidence against conformational change as a signaling mechanism for NELL2 activation of Robo3.

3.2.8 Phylogenetic analysis of Robo and NELL interactions

In order to determine the evolutionary origins of the NELL-binding site in mammalian Robos, we created a multiple sequence alignment of 41 NELL sequences and 85 Robo sequences from 50 different animal species and developed phylogenetic trees for each protein (Figure 19A and B). We found that all vertebrate Robos had a common ancestor prior to the emergence of the cyclostomes, or before the existence of vertebrates (Figure 19B). The first genome duplication according to the 2R hypothesis gave rise to the divergence of Robo1 and Robo2 early in vertebrate evolution, first seen in the cyclostome lineage following divergence from the cephalochordates. The second genome duplication event occurred early in the gnathostome lineage, giving rise to Robo3 from Robo2, allowing for greater divergence in function and biochemical properties. Robo3 appears to have experienced particularly rapid evolution within the mammalian and aves branches as indicated by the greater number of substitutions in these branches while Robo3 in other modern gnathostomes are more similar to their Robo2 paralogs. In protostomes, Robos have undergone separate duplications unrelated to those in vertebrates, notably in *Drosophila*, where 3 copies of Robo are present. In many protostomes, recognizable NELL sequences have been completely lost, as in *Drosophila* and *C. elegans*.

In order to confirm whether the Robos from non-mammalian species bind to NELL, we selected 5 species to represent key moments in vertebrate evolution, as well as 3 species from the two major clades of protostomes, the lophotrochozoans and ecdysozoans, and performed an ECIA to test for binding between full-length proteins and between the FN1 domains of Robo and EGF1-

3 domains of NELL alone. As previously hypothesized, protostomes lacked any evidence of binding between Robo and NELL, while interactions between NELL and Robo were found to be present in all chordates tested (Figure 19C and D). The interactions between Robo and NELL from

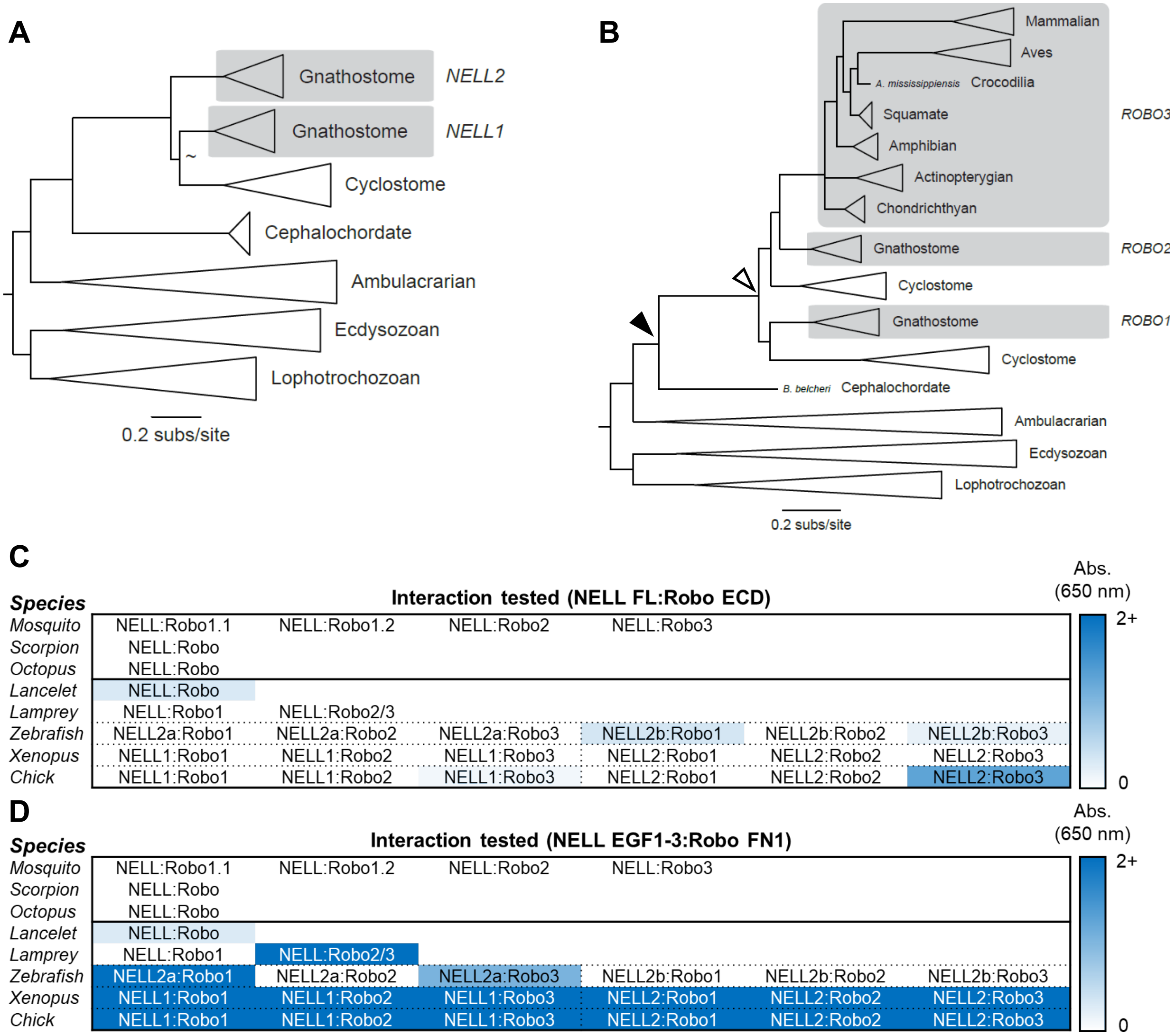

Figure 19: Vertebrate Robos bind to NELLs.
(**A**) Phylogenetic tree constructed for NELLs based on 41 sequences (**B**) Phylogenetic tree constructed for Robos based on 85 sequences. Filled arrowhead: first round of genome duplication in vertebrates, and the latest common ancestor of vertebrate Robos. Open arrowhead: second round of genome duplication in vertebrates. (**C** and **D**) ECIA of (C) full-length NELLs tested against Robo ECDs or (D) NELL EGF1-3 domains against Robo FN1 domains. Protostomes do not show any evidence of binding between NELL and Robo proteins, while binding is present in all vertebrates, as well as the cephalochordate *B. belcheri*.

the cephalochordate *Branchiostoma belcheri* was inconsistently detected, however, showing no binding in certain configurations of the assay, and showing weak binding at best. Additionally, results from the full-length assay contradicted those of the binding domains alone for higher-order vertebrates, showing binding for only NELL2b with full-length proteins but only NELL2a for binding domains alone in the case of Zebrafish proteins, and showing a negative or weak binding result where the binding domains alone gave a strong positive result for *Xenopus laevis* and Chick proteins (Figure 19C and D).

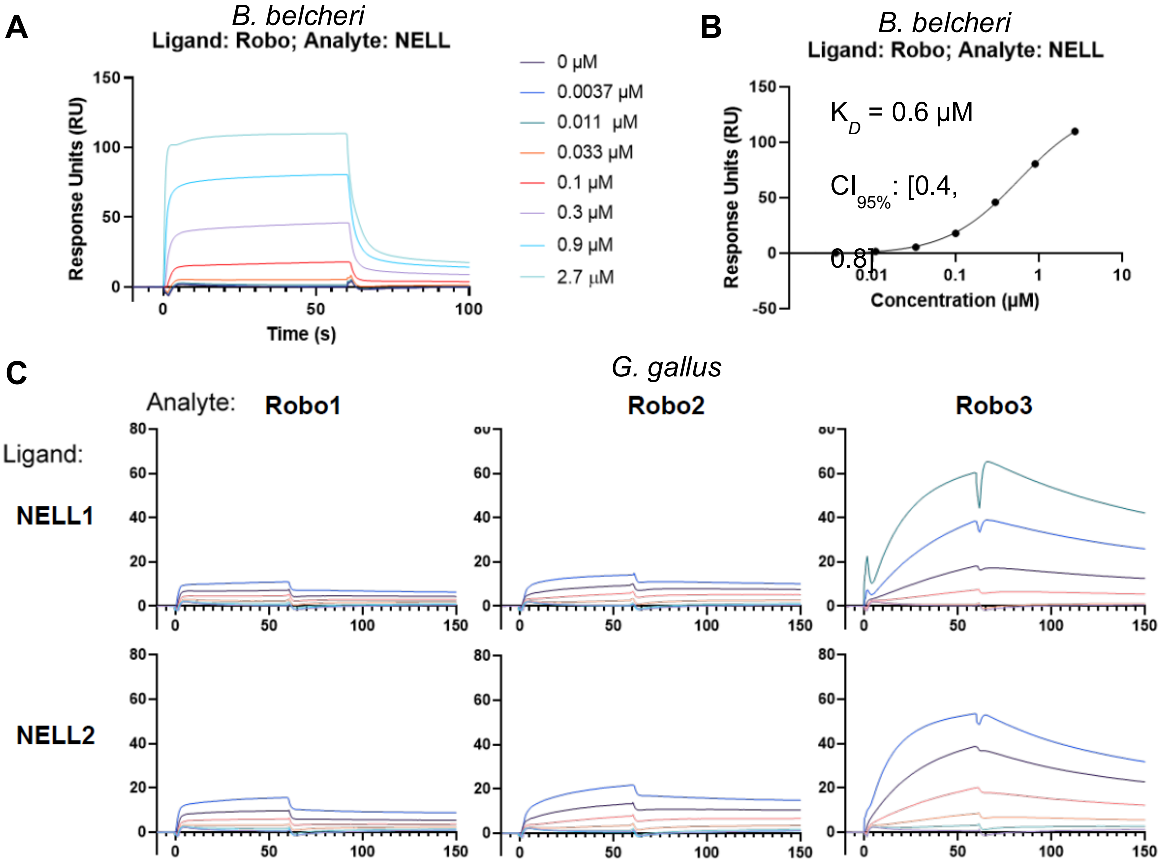

Figure 20: NELL-Robo interactions existed early in vertebrate evolution.
(**A** and **B**) SPR (A) sensorgram responses and (B) Langmuir isotherm for full-length *B. belcheri* Robo as ligand attached to the chip and NELL as analyte. Strong sensorgram responses and dissociation constant of 0.6 µM demonstrates strong binding between these cephalochordate proteins. (**C**) SPR sensorgrams for chick (*G. gallus*) Robos as ligands and NELLs as analytes. Robo1 and Robo2 exhibit weak interactions with NELL1 and NELL2 while Robo3 has much more pronounced response curves.

In order to confirm the results of the ECIA and determine if there is a structural basis for these noted differences in binding strength, we tested the binding of the full-length proteins using SPR. Surprisingly, the *B. belcheri* proteins displayed strong sensorgram responses, yielding a binding affinity of 0.6 μM ($CI_{95\%}$: [0.4, 0.8], Figure 20A and B), similar to the binding affinity between mammalian Robo3 and NELL2 proteins, which confirms that the NELL-Robo interactions present in the Robo1, Robo2, and Robo3 mammalian proteins originated from a common ancestor in the original chordate Robo and NELL prior to gene duplication. We also tested the interactions between full-length chicken Robos and NELLs and determined that Robo3 showed strong interaction with both Chick NELLs, while Robo1 and Robo2 showed SPR responses with NELLs that were at least 3-fold weaker (Figure 20C). These differences in binding affinity in the full-length proteins appear similar to the differences in binding affinity between mammalian Robos and NELLs, suggesting that chick Robos also take on conformational states that affect the availability of the NELL binding site. Chick Robo1 and Robo2 likely retain the closed, oligomeric conformational states of their mammalian counterparts while in Robo3, the open conformational state is conserved. Overall, these results indicate a conservation of the NELL binding site in chordate Robos, as well as the differences in conformational states in higher-order species.

3.2.9 Phase separation in Robo-NELL complexes

Phase separation has been demonstrated to contribute to cellular signaling, mainly through the condensation of intracellular signaling complexes that result in local concentration increases of signaling molecules and initiate downstream signaling events, such as actin polymerization. Robo and NELL exhibit the ability to form molecular condensates in solution at high concentrations, displaying a cloudy, opalescent suspension within 5 min of mixing. In order to

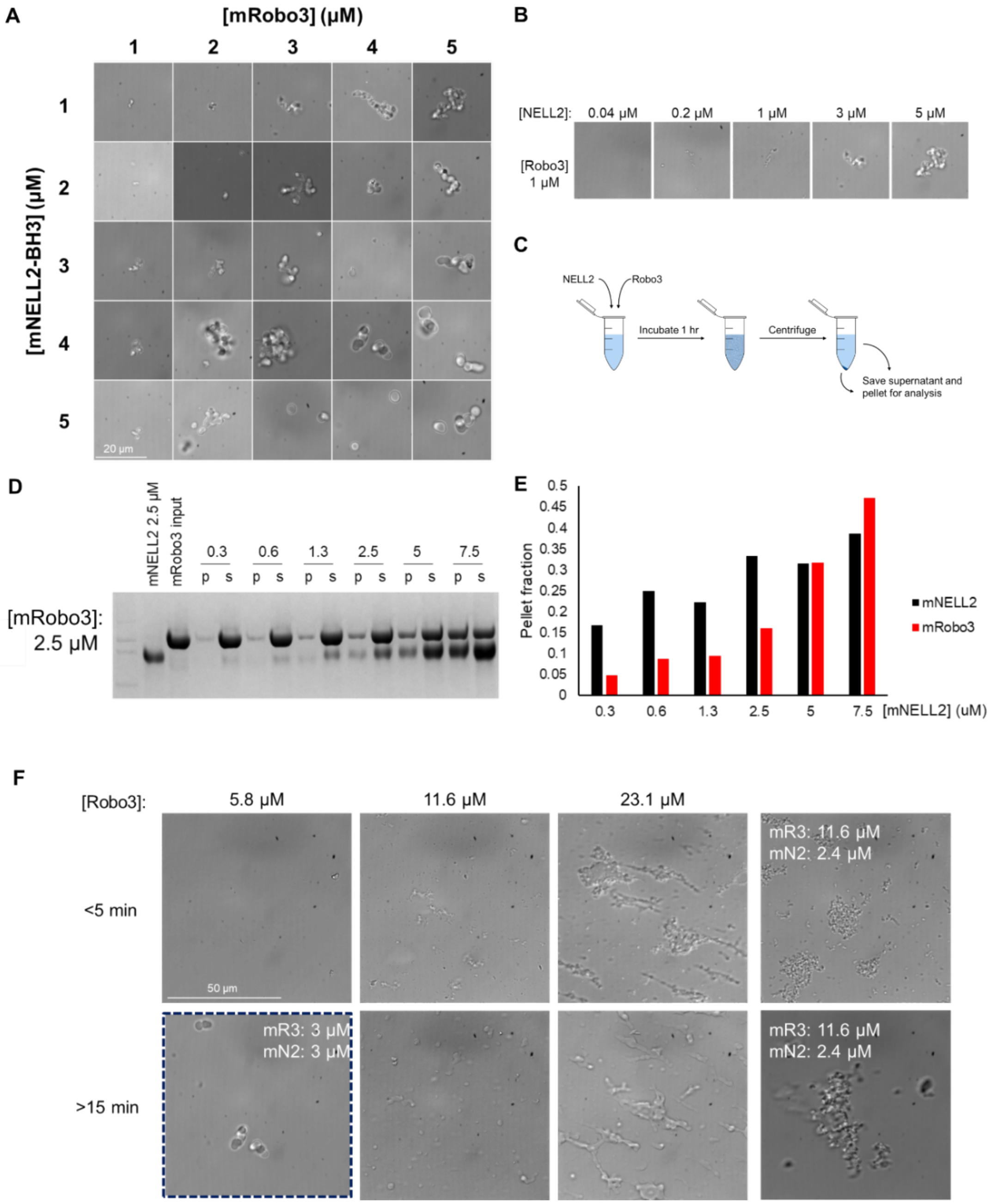

Figure 21: NELL2 and Robo3 form condensates at high concentrations.

(**A** and **B**) Characterization of NELL2-Robo3 droplets across concentrations using DIC imaging. (A) Droplets are observed at concentrations above 1 µM for both proteins and increase in size with increasing concentration. (B) When Robo3 is held constant at 1 µM, droplet formation disappears when decreasing NELL2 concentration to 0.2 µM and lower. (**C-E**) Sedimentation of condensates as shown in the (C) diagram. (D) Coomassie stain of sedimentation experiment results and (E) quantitation. Increasing concentration of NELL2 results in a greater percentage of both proteins being drawn into the droplets. (**F**) DIC images of Robo3-only and NELL2-Robo3 condensates show more fluid characteristics for Robo3-only droplets.

confirm that this condensate is indeed the result of phase separation and not precipitation, we characterized condensate morphology using confocal and DIC microscopy. 50 µl of 14 µM mRobo3 and 50 µl of 4 µM mNELL2 were mixed in a 1.5 ml microfuge tube and incubated for 5 or 30 minutes and pipetted onto a glass-bottom petri dish. Transparent clusters with distinct boundaries were observed and demonstrated growth over time, appearing as small globular clusters after 5 minutes of incubation and larger clusters after 30 minutes. A time lapse over 20 minutes demonstrates growth of the clusters, as well as fusion of the clusters, demonstrating that these condensates are liquids or gels, rather than solid precipitates. Fluorescent labeling of Robo3 with Fluorescein-NHS and NELL2 with Cy3-NHS confirmed that both proteins were localized in the condensates. In order to determine the concentration phase boundary, we mixed Robo3 and NELL2 at various concentrations and observed the formation of clusters at all concentrations higher than 1.0 µM for both Robo3 and NELL2 (Figure 21A). When Robo3 concentration was held constant at 1 µM, NELL2 concentrations above 0.2 µM were sufficient to initiate clustering, near the dissociation constant between the two proteins (Figure 21B). Sedimentation experiments performed to spin down the condensates at 18,000 × *g* also confirmed that the condensates are composed of both Robo3 and NELL2 proteins, with a greater fraction of protein being drawn into condensates with higher concentration (Figure 21D and E). Previously, we demonstrated that NELL2 works cooperatively with Robo3 to signal axon repulsion while NELL1-mediated axon repulsion activity increases linearly with increased concentration. In order to determine if phase separation could be a unique property to NELL2 for increasing affinity for Robo3 with NELL2, we tested NELL1's ability to phase separate. We determined that 15 µM Robo3 and 18 µM NELL1 will also trigger Robo3 condensation, leading to the formation of clusters that grow over time.

To confirm whether these observed condensates performed analogous functions in cells, we transfected HeLa cells with full-length hRobo3. We hypothesized that addition of hNELL2 would trigger clustering of Robo3 on the surface of cells driving more diffuse staining into discrete puncta. However, exogenous expression of Robo3 displayed punctate staining with and without the presence of NELL2. These cells display long neurite-like outgrowths, with Robo3 localized to puncta at the tips of these projections, along with their expression on the cell body (Figure 22A).

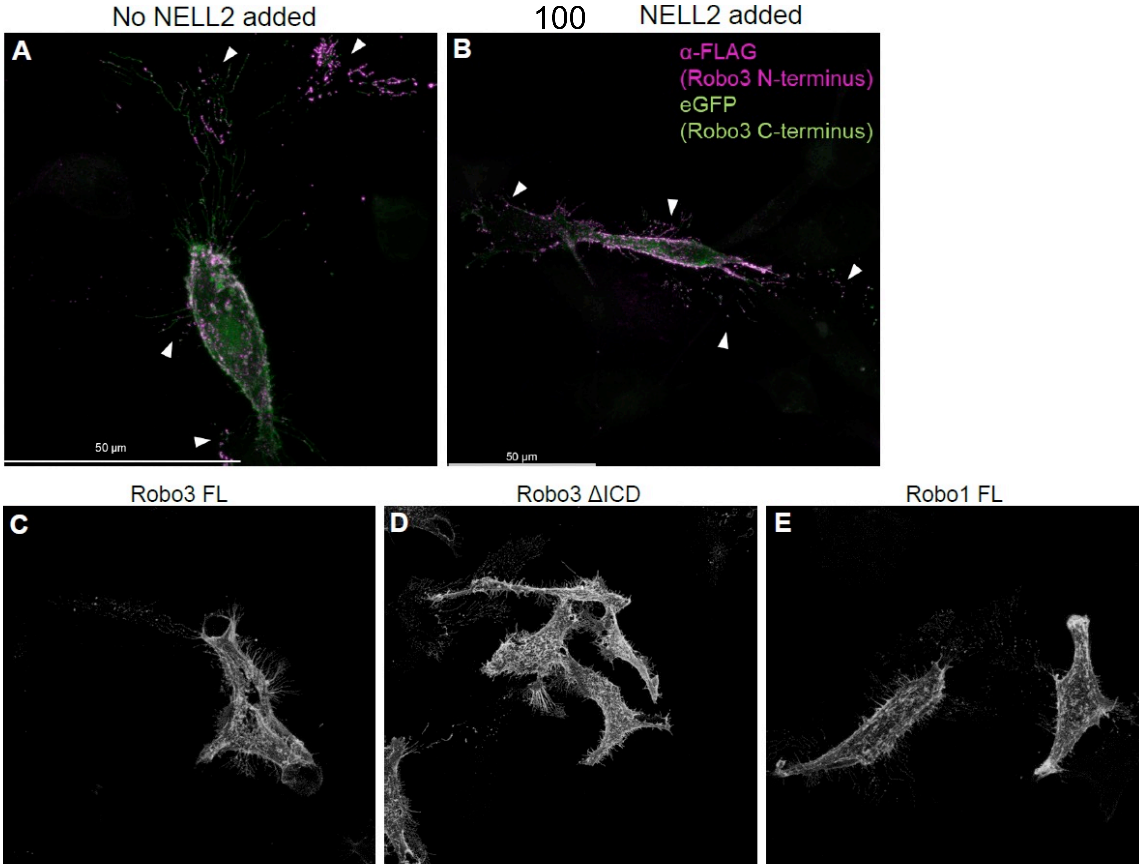

Figure 22: Robo3 spontaneously forms clusters on HeLa cells.
(**A** and **B**) Fluorescence imaging of Robo3-FL transfected into HeLa cells (A) without NELL2 and (B) with 100 nM NELL2 added to cell culture media prior to fixation in 4% PFA. Magenta: anti-FLAG (N-terminal tag), green: eGFP (C-terminal tag). (**C-E**) anti-FLAG images of HeLa cells transfected with Robo3 FL, Robo3 ΔICD, and Robo1 FL containing N-terminal FLAG tags. All constructs expressed at high levels and displayed clusters that led to deformations in the cell membrane.

NELL2 incubation at 100 nM, while capable of inducing axon repulsion, was not sufficient to induce changes in Robo3 expression patterns or growth of cellular projections (Figure 22B). Surprisingly, Robo3 ECD concentrations above 5 μM are capable of producing spontaneous Robo3 cluster formation in solution but appear to differ morphologically from NELL2-containing condensates (Figure 21F). Condensates of Robo3 alone appear more fluid and liquid compared to the more rigid and gel-like condensates of NELL2-Robo3 complexes. In addition, NELL2 induces phase separation at concentrations starting from 0.2 μM while Robo3-only phase separation appears at much higher concentrations. These results suggest that Robo3 may be able to undergo cellular signaling with its extracellular domains alone through clustering and phase separation, with NELL2 being able to stabilize these clusters at lower concentrations and decrease diffusion of Robo3 out of these clusters. Further investigation of the physiological relevance of phase separation is required, however, as spontaneous Robo3 clustering and cellular projections were observed in cell expressing constructs lacking the intracellular domain and in cells expressing full-length Robo1 (Figure 22C-E), raising the possibility that both condensates and cell-surface clusters are simply artifacts of proteins being overexpressed in cells and concentrated to a much higher degree than would be found *in vivo*.

3.3 DISCUSSION

Neuronal connectivity within circuits is shaped by axon guidance cues and their receptors. The Slit-Robo ligand-receptor pair mediates axon repulsion and fulfills a central function in regulating axon guidance at the nervous system midline. Here, we expand on this principal neuronal communication axis with a molecular and functional characterization of the divergent Robo family member, mammalian Robo3, which does not bind Slit proteins but interacts with its own repulsive ligands of the NELL family. Robo3 is essential for commissural axon crossing of the spinal cord midline, and emergence of its unique properties has been proposed as a key evolutionary step in “sculpting the mammalian brain”(Zelina, Blockus, Zagar, Péres, Friocourt, Wu, Rama, Fouquet, Hohenester, Tessier-Lavigne, Schweitzer, Roest Crollius, et al. 2014). We identify the NELL1/2-Robo3 complex interface and validate its importance for NELL-mediated axon repulsion. We also elucidate the molecular basis of NELL binding preference for Robo3 vs. other Robos and identify a low-affinity NELL2-Robo1 interaction site that is occluded by Robo1 ectodomain architecture. Lastly, we demonstrate that the Robo3.1, not Robo3.2, splice isoform mediates NELL2-induced axon repulsion, and we provide evidence that NELL2-dependent Robo3.1 multimerization strongly contributes to signaling output by the ligand-receptor complex. Our results reveal structural requirements for axon guidance by the NELL-Robo3 complex and shed light on multiple evolutionary specializations of mammalian Robo family members.

We observed in our crystal structures that the FN1 domain of Robo3 is engaged by the NELL1 and NELL2 EGF2 and EGF3 domains using a set of amino acids conserved across vertebrate Robo and NELL sequences. Since we have identified alanine mutations on both EGF domains that can nearly abolish Robo3 binding, it is clear that both domains are required for the ligand-receptor interaction, which agrees with our domain mapping data. Interactions between FN and EGF domains, to our knowledge, are not commonly reported, despite both domains being highly represented in cell surface and secreted proteomes in bilateria. One prominent example of EGF domains interacting with FN domains is Netrin binding to its receptors DCC and Neogenin(Finci et al. 2014; Xu et al. 2014), which have domain arrangements similar to Robos (4 IG followed by 6 FN vs. 5 IG and 3 FN). However, the topology of binding in Netrin-DCC and Robo-NELL complexes are completely unrelated, and the two receptor-ligand pairs appear to have arisen independently, despite functioning on the same set of commissural neurons in the developing spinal cord.

We also demonstrate a direct relationship between affinities of engineered NELL2 variants to Robo3 and the degree of repulsive effect of NELL2 on growing commissural axons *in vitro*. The correlation between a thermodynamic property of the interaction measured with isolated proteins and the downstream cellular phenotype proves the physiological relevance of the NELL2-Robo3 crystallographic interface and shows the exquisite control NELL2 has on the growth cone as a guidance cue.

Similar to NELL2, we show that NELL1 can elicit commissural axon repulsion *in vitro*, which can be explained by several observations we report here. First, NELL1 binds Robo3 with an affinity comparable to NELL2. Second, our structural and biochemical analyses of the NELL1-Robo3 EGF1-3-FN1 complex demonstrate highly similar modes of receptor engagement by the EGF2 and EGF3 domains of the two NELL family members. Third, NELL1 and NELL2 share a common oligomeric state – they are both trimeric. Despite these similarities, the guidance activity of NELL1 is at least one order of magnitude lower than NELL2's. This observation suggested the existence of differences in NELL1-Robo3 and NELL2-Robo3 complex architectures that strongly influence downstream signaling activity, possibly through the actions of the LamG and VWC domains of NELLs. However, our axon repulsion assays using chimeras of NELL1 and NELL2 identify the EGF1-3 domains as the major determinant of repulsive activity for these two proteins. This supports the idea that NELL EGF1-3 domains modulate repulsive activity independent of receptor affinity, possibly through conformational control of full-length NELLs that affects Robo signaling. NELL2 is the only NELL family member expressed in the developing spinal cord(Jaworski et al. 2015), calling into question whether NELL1 has the opportunity to interact with Robo3 *in vivo*. Instead, the known functions of NELL1, including those outside the nervous system, might be mediated by signaling through other Robo receptors (see below) via architecturally divergent complexes and signaling strategies.

NELLs were first identified as Robo3 ligands. Here, we find that NELL2 can interact with moderate affinity (K_D = 14 μM) with the Robo1 FN1 domain. This interaction can be explained by similarities in the NELL-binding surfaces across vertebrate Robo1, Robo2, and Robo3 sequences. However, the NELL2-Robo1 interaction is very weak (K_D = 350 μM) when studied in the context of the complete Robo1 ECD. This implies that the Robo1 ECD adopts a conformational state in which NELL2 access to the FN1 domain is blocked. No such inhibition was observed for the NELL2-Robo3 interactions. This can be explained by both of our observations that (1) Robo3 adopts an extended, open architecture, where the maximal pairwise distance (D_{max}, 31 nm) corresponds to an extended eight-IG/FN domain molecule, and (2) Robo3 ECD is predominantly a monomer, unlike the dimeric/oligomeric Robo1, at least in its unliganded state. As a result, NELL2 binding to an "open-state", monomeric Robo3 is unhindered by any steric clashes, which is not the case in a more compact and dimeric or tetrameric Robo1 structure reported by Aleksandrova et al(2018).

Two studies that were published as our manuscript was in preparation, in combination with our data, provide strong clues to conformational states of vertebrate Robos and interactions with NELLs. First, Yamamoto et al.(Yamamoto et al. 2019) showed that NELL1 can interact with the FN1 domain of Robo2, but not the full Robo2 ECD. This cryptic interaction is similar to the one we describe for NELL2-Robo1 binding, and both are mediated by the same domains. In addition, we are able to provide an accurate picture of this binding interface through homology with the NELL2-Robo3 structure we present, confirmed via mutagenesis. Second, Barak et al.(Barak et al.

2019) show that Robo2 adopts a closed-state monomer where domains IG4, IG5, FN1, and FN2 (domains 4 to 7) create a compact hairpin-like structure. The NELL-binding surface of FN1 we report in this manuscript is masked in the closed-state Robo2 structure, explaining why NELL binding to full-length Robo1/2 is impaired, while the extended Robo3 engages NELLs with higher affinities. Intriguingly, a Robo1 ECD with its FN1 domain swapped against that of Robo3 proved to be strictly monomeric and a high-affinity binder of NELL2. This highlights the importance of the FN1 domain not only in providing high- and low-affinity NELL binding sites in Robo3 and Robo1, respectively, but also in dictating the oligomeric state of Robos and enabling an open conformation for NELL engagement.

In our work, we measured a 25-fold difference in NELL2 affinity between full-ectodomain Robo1 and the Robo1 FN1 domain. Since NELL2 can only bind to an open-state Robo1, this indicates that the closed-state Robo1 is ~25-fold more stable than its open state, providing the first estimate of an equilibrium constant for a Robo1 conformational. It is intriguing to speculate that NELLs can act as regulators of Robo1/2 conformational states, e.g. in postcrossing commissural axons, which express high levels of Robo1/2 and navigate in close proximity to the NELL2 expression domain in the spinal cord ventral horn. Since the closed, auto-inhibited state and open, NELL-bound states of Robo1/2 are incompatible, very high concentrations of NELLs could force Robo1 and Robo2 into an open conformation that can either allow formation of active Robo1/2 or facilitate Robo1/2 binding to Slit and signal transduction. Furthermore, a *trans* tetramer proposed by Aleksandrova et al.(2018) and a *trans* dimer proposed by Barak et al.(Barak et al. 2019), as inhibited cell-cell adhesive states for Robo1/2, would also be broken by NELL binding to Robos. The reverse is also possible – Slit-activated Robo1 and Robo2 may become NELL-responsive.

Future structural, biophysical, and functional studies are required to differentiate between plausible models and reconcile existing data.

As discussed above, mammalian NELL1 and NELL2 interact with all three neuronal Robos, although with different affinities. The most parsimonious explanation for these observations is that the ancestral molecules in the chordate lineage that gave rise to the mammalian Robo and NELL paralogs interacted with each other. Since the ancestral Robo is also expected to bind Slit, it is conceivable that this receptor or some of the extant Robo family members might engage both Slits and NELLs through high-affinity interaction sites, which needs to be tested. It is also of interest to determine whether invertebrate NELLs can interact with Robos. While we did not observe strong conservation at the Robo interaction surface for invertebrate NELL sequences, we cannot rule out Robo-NELL interactions in extant invertebrates or for an ancestral bilaterian Robo-NELL pair.

Robo3 has been reported to have two splice isoforms, Robo3.1 and Robo3.2, which have identical ECDs and can both bind NELLs; however, spinal commissural axons only respond to NELL2 before crossing the midline, when they express Robo3.1, but they are unresponsive to NELL2 after crossing, at which point they express Robo3.2(Z. Chen et al. 2008; Jaworski et al. 2015). Through isoform-specific rescue experiments of *Robo3*$^{-/-}$ neurons, we show that Robo3.1 is necessary and sufficient for dorsal spinal cord axon repulsion from NELL2. Hence, Robo3.1 is the sole functional NELL receptor in commissural neurons, and distinct signaling capabilities of Robo3.1 and Robo3.2 underlie the differential sensitivity of pre- and postcrossing commissural axons to NELL2. Since Robo3.1 and Robo3.2 only differ in the extreme C-termini of their ICDs, this suggests that critical mediators of NELL2 signaling are recruited to the unique C-terminus of Robo3.1. Robo1 and Robo2 transduce Slit signaling via binding of adapter proteins to the cytoplasmic sequences that are conserved across Robos(Blockus and Chédotal 2016a). It remains to be determined whether NELL2-Robo3 signaling employs at least some of the same cytoplasmic motifs and downstream mediators as Slit-Robo1/2 and whether NELL-Robo1/2 complexes produce functional output, given the absence of a sequence similar to the Robo3.1 C-terminus.

A common strategy for signal transduction across the membrane used by single-pass transmembrane proteins is oligomerization upon cue/ligand binding, or the formation of large, lattice-like oligomers, as recently proposed for the Netrin receptor DCC or the protocadherins(Finci et al. 2014; Goodman et al. 2017; Rubinstein et al. 2015; Xu et al. 2014). As mentioned above, we and others(Kuroda et al. 1999; Nakamura et al. 2014) have demonstrated that NELLs are constitutively trimeric. Using four different methods – AUC, SEC, MALS, and SAXS – we also demonstrate that their high-affinity unliganded receptor, the extracellular domain of Robo3, is primarily a monomer, while we confirm a predominantly dimeric state for the Robo1 ECD. We also show that the axon guidance activity of monomeric NELL2 lacking its CC domain is strongly reduced. Our results indicate that, unlike Slit-binding Robos, Robo3 does not multimerize in the absence of ligand, and that NELL2-mediated formation of Robo3 trimers or higher-order oligomers is a main driver of Robo3 activation and repulsive signaling.

3.4 METHODS

3.4.1 Animals

All experimental procedures had institutional approval through Brown University's Institutional Animal Care and Use Committee and followed the guidelines provided by the National Institutes of Health. Mice carrying the *Robo3* null allele have been described before and were genotyped by PCR amplifying part of the *Robo3* genomic locus (primer sequences: TACCAGCTACTTCCAGAGAG, CCAACATCGAGTGGTACAAG, and

GATCTCTCGTGGGATCATTG)(Sabatier et al. 2004). All mice were maintained on a CD-1 background. For timed pregnancies, the day of vaginal plug was defined as E0.5. Tissue sections or neuronal cultures were prepared from embryos of either sex.

3.4.2 Spinal cord electroporation and primary neuron culture

The dorsal fifth of E11.5 mouse spinal cords were microdissected and used for preparation of neuronal cultures; in some instances, dissection was preceded by introduction of expression constructs via spinal cord electroporation. For electroporation, 100 ng/ml DNA in injection buffer (30 mM HEPES pH 7.5, 300 mM KCl, 1 mM $MgCl_2$, 0.1% Fast Green FCF (Sigma)) was injected into the central canal of the neural tube, and a BTX ECM 830 electroporator was used to electroporate DNA bilaterally into spinal cord neurons (Five 30-V pulses of 50 ms duration each for each half of the spinal cord). Dissected spinal cord fragments were washed in cold Ca^{2+}/Mg^{2+}-free Hanks' Balanced Salt Solution (HBSS). Tissue was digested with 0.05% trypsin in Phosphate-buffered saline (PBS; Gibco) at 37° for 7 min, and DNase I was added for an additional 1 min along with 0.15% $MgSO_4$. Tissue pieces were washed with warm Ca^{2+}/Mg^{2}-free HBSS, and a small fire-polished Pasteur pipette was used to triturate and dissociate the tissue into single cells. Cells were plated on nitric acid-washed and baked 18-mm coverslips coated with 100 μg/ml Poly-D-Lysine (Sigma) and 2 μg/ml N-Cadherin (R&D Systems). Cells were cultured in Neurobasal media supplemented with 10% heat-inactivated FBS and 1x penicillin/streptomycin/glutamine (Gibco). Neurons were used for experiments 16-24 h after plating. 1 h prior to use in axon turning assays, media was switched to Neurobasal media (Gibco) supplemented with 2% B-27 (Gibco) and 1x penicillin/streptomycin/glutamine.

3.4.3 AP fusion protein binding experiments

COS-7 cells (ATCC) were cultured in DMEM media (Gibco) supplemented with 5% fetal bovine serum (Gibco) and 1x penicillin/streptomycin/glutamine (Gibco). COS-7 cells were transfected using Viofectin (Viogene)(Jaworski et al. 2015). The mouse Robo3.1, human Robo3$^{\Delta IG1\text{-}5}$, human NELL2-AP, and NELL2$^{EGF1\text{-}6}$-AP expression constructs have been described before(Jaworski et al. 2015). Untagged and AP-tagged proteins for AP fusion protein binding assays and repulsion experiments were expressed *in situ* following transfection with Viofectin (Viogene). Cells expressing AP-fusion proteins were kept in Opti-MEM (Gibco), and media was collected after 48 h of culture(Jaworski et al. 2015). AP-binding assays were carried out 44-48 hours following COS cell transfection. To assess binding of AP-fusion proteins to receptor-expressing COS cells, cultures were rinsed twice in AP binding buffer (HBSS (Gibco), 20 mM HEPES pH 7.0, 0.2% BSA, 5 mM $CaCl_2$, 1 mM $MgCl_2$, 2 µg/mL Heparin (Sigma)) and incubated with AP-fusion proteins diluted in AP binding buffer for 90 min at 4°C(Jaworski et al. 2015). Cultures were washed three times with AP binding buffer, and fixed in 4% paraformaldehyde (PFA) in PBS for 15 min at room temperature. Cells were then washed three times with an aqueous solution of 20 mM HEPES pH 7.4, 150 mM NaCl. Endogenous AP activity was deactivated by incubating cultures at 65° C for 3 h. Cultures were then washed with AP buffer (100 mM Tris pH 9.5, 100 mM NaCl, 50 mM $MgCl_2$), and AP activity was visualized by incubating cultures overnight with NBT/BCIP (Roche; 1:50) in AP buffer. The visualization reaction was stopped by washing cells 3 times in 1mM EDTA, 0.1% Triton X-100 in PBS, and cultures were mounted under 80% glycerol in PBS.

3.4.4 Dunn chamber axon turning assay

The Dunn chamber axon turning assay was performed essentially as described before(Yam et al. 2009). In short, Dunn chambers were removed from a 70% ethanol bath, dried, and washed once with Neurobasal media (Gibco) then twice with conditioned media from primary neuronal cultures. Conditioned media was added to the inner and outer wells of the chamber, and a coverslip containing primary commissural neurons was inverted onto the chamber, leaving a small opening to add or remove liquid from the outer well. Conditioned media was removed from the outer well and replaced with conditioned media containing recombinant NELL1 or NELL2 at specific concentrations. The chamber was then sealed using 1:1 (w/w) paraffin/vaseline. Chambers were kept at 37°C in a stage-top incubator, and DIC images of neurons on the bridge region of the Dunn chamber (~40 fields per chamber) were acquired every 2 min for 2 h on a Nikon Ti-E microscope.

3.4.5 Quantification of axon turning

Quantitative analysis of axon turning in Dunn chambers was performed in a similar fashion to Yam et al.(Yam et al. 2009). Briefly, only neurons that extended without encountering debris or other neurons were considered for analysis. Neuron identity was confirmed by post-hoc immunostaining of the imaged coverslip for the commissural neuron marker TAG-1 to differentiate contra- vs ipsilaterally projecting neurons, or for RFP to visualize electroporated neurons. The initial axon segment at $t = 0$ h was translated to the coordinates (0,0) and rotated such that the gradient increased along the y-axis (angle of rotation was calculated from microscope stage coordinates relative to the Dunn chamber's center). To determine the magnitude and directionality of an axon's turn, the angle between the original trajectory ($t = 0$ h) of the axon's distal 10 μm and the final trajectory ($t = 2$ h) of the axon's distal 10 μm was calculated. This value, the turning angle, was averaged over 25-100 neurons in each Dunn chamber replicate, and 3-5 biological replicates (tissue from each individual embryo counting as a single replicate) were tested for each experimental condition. Positive angle indicates a turn towards the gradient, and a negative angle indicates a turn away from the gradient. Turning angles were averaged across all neurons for each replicate, and the means across multiple replicates were analyzed for statistical significance using an unpaired two-tailed t-test (n and *p* are indicated in figures and figure legends).

3.4.6 Immunohistochemistry

Unless indicated otherwise, all incubations were performed at room temperature. Following imaging in Dunn chambers, coverslips holding the cultured neurons were carefully removed from Dunn chambers and fixed in PBS containing 4% paraformaldehyde (PFA) overnight at 4°C, washed three times for 10 min in PBS, blocked in 2.5% fetal bovine serum and 0.1% Triton X-100 in PBS for 1 h, and incubated with primary antibodies in blocking solution at 4°C overnight. After three 5 min washes in 0.1% Triton X-100 in PBS, cultures were incubated with secondary antibodies in blocking solution for 2 h. Cultures were then washed three times 10 min in 0.1% Triton X-100 in PBS and mounted on glass slides using Fluoromount G. For cell-surface staining of neurons under non-permeabilized conditions, primary antibody was added directly in the growth media to live neurons and incubated at 4°C for 2 h. Cells were then washed three times with PBS, fixed in 4% PFA/PBS for 15 mins, washed three times for 10 min in PBS, then incubated with secondary antibodies in blocking solution for 2 h. Cultures were washed three times 10 min in 0.1% Triton X-100 in PBS and mounted on glass slides using Fluoromount G. Tissue section staining was performed as previously described(Jaworski, Long, and Tessier-Lavigne 2010). Primary antibodies used for IHC were goat polyclonal antibodies against Robo3 (R&D Systems, 1:200) and TAG-1 (R&D Systems, 1:200), rabbit polyclonal antibodies against NELL2 (gift from Nakamoto Lab, 1:100)(Jiang et al. 2009), RFP (Rockland, 1:500), and TuJ1 (Biolegend, 1:2000), and a rabbit monoclonal antibody against Robo3.1 (1:200)(Z. Chen et al. 2008). Secondary antibodies (Invitrogen; 1:200) were Alexa488-conjugated donkey anti-goat, and Alexa594-conjugated donkey anti-rabbit. Hoechst 33342 (Molecular Probes, 1:1000) was added with the secondary antibodies. All images were acquired on a Nikon Ti-E microscope.

3.4.7 Protein expression for structural biology

Mouse and human NELL1, NELL2, Robo1 and Robo3 proteins were expressed using baculoviruses. The mature domains or domain truncations of these genes were cloned into pAcGP67A (BD Biosciences) with C-terminal hexahistidine tags and co-transfected into Sf9 cells (*Spodoptera frugiperda*) with linearized baculovirus BestBac 2.0 (Expression Systems) using the TransIT-Insect transfection reagent (Mirus) according to manufacturer's instructions. Sf9 cells were cultured in in SF900 SFM III (Fisher, 12658-019) with 2 mM L-glutamine (HyClone SH30034.02), 20 µg/ml gentamicin sulfate and 10% fetal bovine serum. For infection of High Five cells with baculoviruses, 2-5 ml of virus-containing conditioned media from Sf9 cultures were added per 1 L of High Five culture.

The produced viruses were used to infect cultures of High Five cells (*Trichoplusia ni*, BTI-Tn-5B1-4) grown in suspension (120 r.p.m. on shakers) at 27-28ºC in Insect-XPRESS media (Lonza, BE12-730Q) with 10 µg/ml gentamicin sulfate (Lonza, 17-518L). Proteins were expresssed for 66 hours at 27-28°C post-infection. For producing biotinylated proteins, a C-terminal Avi-tag (GLNDIFEAQKIEWHE) followed by a hexahistidine tag was added to expression constructs. Avi-tagged proteins were biotinylated with the E. *coli* biotin ligase BirA.

3.4.8 Protein Purification

Secreted proteins were purified from media using Ni-NTA Agarose resin (Qiagen), followed by size-exclusion chromatography (SEC) with either Superdex 200 10/300 or Superose

6 10/300 columns (GE Healthcare) in HEPES-buffered saline (HBS: 10 mM HEPES pH 7.2, 150 mM NaCl). Protein complexes were isolated by SEC.

3.4.9 Protein crystallization

The purified hNELL2 EGF1-6/hRobo3 FN1-3 complex was concentrated to 15 mg/ml in HBS, and crystallized using the sitting-drop vapor diffusion method in two similar conditions: 17% PEG 3,350, 0.4 M NaSCN and 0.1 M HEPES, pH 7.5, 12% PEG 6,000. The two crystal forms were washed, dissolved in water, and run on SDS-polyacrylamide gels. Silver-staining of the gels revealed that the first crystal form was likely NELL2 EGF1-6 complexed to Robo3 FN1 following proteolysis in the linker joining FN1 and FN2 domains, and the second crystal form likely contained the remaining FN2 and FN3 domains of Robo3.

The purified hNELL1 EGF1-3/hRobo3 FN1 complex was concentrated to 15 mg/ml in HBS, and crystallized using the sitting-drop vapor diffusion method in 20% PEG 3,350, 0.2 M $Mg(NO_3)_2$. Crystal screening and optimization was performed using a Mosquito crystallization robot (TTP Labtech).

3.4.10 X-ray crystallography

Crystals grown in the first condition (hNELL2 EGF1-6/hRobo3 FN1 complex) were cryoprotected in 17% PEG 3,350, 0.4 M NaSCN, 30% Glycerol before being vitrified in liquid nitrogen. The crystals diffracted to ~2.7 Å resolution at Argonne National Laboratory's Advanced Photon Source synchrotron beamline 23-ID-D. Molecular replacement (MR) with the first Fibronectin type III domain model from human Robo2 (PDB: 1UEM) yielded a weak solution with a Z-score of 13 using *PHASER*(McCoy et al. 2007), which was not sufficient to determine phases accurately enough to model the entire structure. Therefore, we prepared selenomethionine-labeled human NELL2 EGF1-6 (hRobo3 FN1 contains no methionines) according to Cronin et al.(Cronin, Lim, and Rogers 2007) in baculoviral/High Five cell cultures. The SeMet-labeled complex degraded similarly in crystal drops and crystallized in the original crystallization condition. X-ray diffraction data was collected at the peak absorption wavelength for selenium (12660.3 eV) to ~2.7-Å resolution at the APS beamline 24-ID-C.

Both native and SeMet datasets were reduced using *XDS*(Kabsch 2010), and subjected to an MR-SAD (molecular replacement with single-wavelength anomalous diffraction) phasing strategy using *phenix.autosol*(Terwilliger et al. 2009). The MR solution for the Robo3 FN1 domain was again weak but was sufficient to identify two highly-ordered methionine sulfur positions, those in M456 and M465, in the EGF2 domains of hNELL2, which was in turn sufficient to phase the anomalous diffraction dataset and yield interpretable electron density maps. Following initial model building using maps from the anomalous dataset, a native dataset was used for complete model building in *COOT*(Emsley et al. 2010) and reciprocal-space refinement using *phenix.refine*(Afonine et al. 2012). Within the model, the C-terminal EGF domains had inferior density, likely as a result of flexibility and lack of crystallographic contacts. As a result, the modeling of the sixth EGF domain is incomplete, and the details of coordination of the third calcium binding site is unclear. Validation of the model was performed using tools provided in *COOT* and in *Molprobity*(V. B. Chen et al. 2010) as part of the *PHENIX* package.

Crystals grown in the second condition (hRobo3 FN2-3) were cryoprotected in 12% PEG 6,000, 0.1 M HEPES, pH 7.5, 30% Glycerol before being vitrified in liquid nitrogen. The crystals diffracted to 1.8 Å resolution at APS beamline 23-ID-D. Molecular replacement with PDB: 4HLJ using the MoRDA pipeline(Vagin and Lebedev 2015) yielded a strong solution. Model building and reciprocal-space refinement was performed using *COOT* and *phenix.refine*, respectively.

Validation of the model was performed using tools provided in *COOT* and *Molprobity* as part of the *PHENIX* package.

hNELL1 EGF1-3/hRobo3 FN1 crystals were cryoprotected by adding 30% Glycerol to the crystallization condition. Diffraction data to 1.8 Å was collected at APS beamline 23-ID-D. The structure was solved with MR using the NELL2/Robo3 structure as a model in *PHASER*. The structural model was built and refined as described above. The positioning of the two FN domains within the crystallographic lattice appears to have caused less well-defined density for parts of the FN2 domain due to flexibility, and higher overall B-factors for FN2 atoms.

3.4.11 Affinity measurements by cell staining

The cell staining protocol from Salzman et al.(Salzman et al. 2016) was followed after adopting it for *Drosophila* S2 cells and with modifications. NELL2 and Robo3 ectodomain constructs with an C-terminal FLAG tag are expressed in *Drosophila* S2 cells by creating a fusion with the transmembrane helix of rat Neurexin-1, using transient transfections with the TransIT-Insect transfection reagent (Mirus) according to manufacturer's instructions. After culturing for 3 days, cells were collected and washed with PBS twice. Final cell pellet was resuspended in PBSB (1x Phosphate Buffered Saline + 0.1% Bovine Serum Albumin), incubated with an iFluor488-coupled anti-FLAG antibody (GenScript, 1 μg/ml) for 30 min at 4°C and washed with PBSB twice. Next, protein ligand at various concentrations was added onto cells for 30 min at 4°C, and cells were washed twice with PBSB. Finally, cells were mixed with Cy5-labeled Streptavidin for 30 min at 4°C and washed twice with PBSB. (Expression plasmid for a Streptavidin cysteine mutant, and expression, purification and Cy5 labeling protocols were a gift from Michael Birnbaum.) Cells were then run through an Accuri C6 flow cytometer to detect fluorescence at the 488 nm and Cy5/695nm channels. Analysis was performed using the Accuri C6 software, where gating was performed to select anti-FLAG positive cells, and binding was measured in the Cy5/695 nm channel as mean fluorescence intensities (MFI). Ligand concentrations used for staining vs. 695 nm MFI values were plotted for fitting to 1:1 Langmuir binding isotherms (Figure 14D-E).

3.4.12 The Extracellular Interactome Assay (ECIA)

Robo and NELL constructs were cloned in to pECIA-prey and pECIA-bait plasmids(Cheng, Ashley, et al. 2019). The assay was performed as described before(Cheng, Ashley, et al. 2019; Özkan et al. 2013). When mutants of Robo and NELL constructs were tested for binding, the expression levels of the bait and prey were normalized for comparison purposes by quantitation via western blot and dilution of samples at higher concentrations.

3.4.13 Quantitation by Western Blot

Quantitation of purified protein from SEC and secreted protein in conditioned media for ECIA was achieved using western blots against the hexahistidine epitope present at the C-termini of all constructs (antibody: fluorescent His-Tag Antibody with iFluor 488, Genscript, catalog no. A01800, 1:500 dilution). Quantitation of fluorescent signal was performed using a Biorad Chemidoc system and ImageLab version 6 (Biorad). For mNELL2 binding to mRobo3 FN1, peak fractions from the SEC elutions were loaded onto an SDS-PAGE gel in triplicate, along with samples of mNELL2 and mRobo3 mixed in a 1:1 molar ratio as standards. A linear regression was calculated between concentration and intensity of the standards.

3.4.14 Surface plasmon resonance (SPR)

SPR experiments were performed with streptavidin (SA) chips using a Biacore T200, 3000, or 8K (GE Healthcare) or NLC (Neutravidin) chips on a ProteOn XPR36 (Biorad). Robo3 FN1-3 samples were biotinylated using BirA biotin ligase taking advantage of a C-terminal Avi-tag. hRobo3 FN1-3 was captured on an NLC chip, and mRobo3 FN1-3 was captured on an SA chip.

The experiments were performed at 25°C in 10 mM HEPES, pH 7.2, 150 mM NaCl, 0.05% Tween-20 and 0.1% BSA; lack of BSA resulted in binding curves with strong non-specific binding which appeared to incorrectly imply high affinity and slow dissociation. All curve fitting was done using the BIAEvaluation, Insight evaluation (GE Healthcare) or Prism (Graphpad) following a 1:1 Langmuir binding model. Prism was used especially when a non-specific-binding term had to be introduced in data fitting (see below).

mRobo1 ectodomain was captured on a CM5 chip using random amine coupling at a density of ~1,200 R.U. The remainder of the SPR experiment was performed as above. Assuming a range of 50 to 100% active surface, the equilibrium binding responses of mNELL2 ectodomain yield K_D values of 190 to 400 μM (Figure 17B).

mRobo1 FN1-3 was captured on a Streptavidin Biacore chip via chemical biotinylation of N-terminal amine with N-hydroxysuccinimidobiotin (NHS-Biotin) at pH 6.5. 315 R.U. of mRobo1 was captured on a Biacore SA chip. The remainder of the SPR experiment was performed as above. The results of the experiment are in Figure 17E-F. While a theoretical maximum of ~235 R.U. was expected for mNELL2 EGF1-6 binding, the sensorgram data yielded an R_{max} of 143 R.U., predicting a reasonable ~60% active Robo1 surface.

For the Robo chimera and mNELL2$^{\Delta CC}$ experiments, mRobo3 ECD, mRobo1$^{Robo3\text{-}FN1}$ ECD, mNELL2, and mNELL2$^{\Delta CC}$ were captured on a Biacore Series S SA chip after chemical biotinylation with NHS-Biotin performed as above. 167 RU of mRobo3, 177 RU of mRobo1$^{Robo3\text{-}FN1}$, 100 RU of mNELL2, and 100 RU of mNELL2$^{\Delta CC}$ were captured on the surface. The SPR experiment was carried out with the same buffer conditions as above, with the addition of a regeneration step between each run with 10 mM HEPES, pH 7.2, 150 mM NaCl, 0.05% Tween-20, 0.1% BSA, and 10 mM EDTA in order to remove any nonspecific binding.

When full-length NELL2 was used as analyte against a full-ectodomain Robo surface (i.e. mobile phase), we observed binding with a fast and a slow component. Since we have no independent evidence for a two-step binding mechanism or heterogenous ligand/analyte, we analyzed the binding data with a 1:1 Langmuir binding isotherm with a linear non-specific binding term ($NS \times$ [Analyte]). This yields dissociation constants (0.5-1 μM) closely matching other values we measured for Robo3-NELL2 binding.

Finally, in some of our SPR experiments with NELL2$^{\Delta CC}$, which were performed on a newly installed Biacore 8K, larger-than-usual injection spikes were observed. As affinity analysis was performed based on equilibrium binding, these spikes do not affect the reported K_D values.

3.4.15 Analytical ultracentrifugation (AUC)

Experiments were performed on a Beckman Coulter analytical ultracentrifuge with an An50-Ti rotor. The data were analyzed using the c(s) methodology in SEDFIT(P. Schuck 2000; Zhao et al. 2013). Partial-specific volume, density, and viscosity were calculated using SEDNTERP(Laue et al. 1992). For analysis, partial specific volumes of 0.7299 and 0.7322 cm^3/g for mRobo1 and mRobo3 samples, respectively, were used. Density and viscosity of the solution were assumed to be 1.005 g/cm^3 and 0.01025 Poise. AUC data illustrations were drawn using GUSSI(Brautigam 2015).

A pilot, single-concentration experiment was performed at 200,000 g at 20ºC with 2.5 μM mRobo1 and 1.8 μM mRobo3 (Figure 18A). 400 μl mRobo1 and mRobo3 samples were prepared and placed in 1.2 cm-pathlength centerpieces, except for the 100 μl 9.8 μM, 11.1 μM and 20 μM mRobo3 samples, which were placed in 0.4-cm pathlength centerpieces. Samples were centrifuged at 140,000 g for mRobo1 and at 200,000 g for mRobo3, at 20ºC.

SV data for mRobo3 revealed a major species at 4 S with a frictional ratio of 1.6 to 1.7, indicating an elongated shape, and an expected mass of 88 kDa, in agreement with a monomer. A ~7-S peak observed in mRobo3 samples did not become more prominent with increasing mRobo3 concentrations, indicating that this peak may represent a contaminant or misfolded or aggregated species. For mRobo1, numerous peaks are observed in $c(s)$ distributions, including the major 6.6-S peak representing dimeric mRobo1, but also peaks at 4S and several between 8 and 30 S. The species appear to be in equilibrium, as the monomer wanes with increasing mRobo1 concentrations, and the 8.1-S peak (possibly a tetramer) becomes the second most prevalent peak with increasing concentrations.

3.4.16 Multi-angle light scattering (MALS)

MALS experiments were done on a Wyatt HELEOS II scattering detector coupled to an AKTA FPLC (GE Healthcare) with a Superose Increase 6 10/300 column using HBS as the sample and running buffer. For data collection and analysis, ASTRA software version 5.3.4 (Wyatt Technology Corp) was used. Average molar mass values calculated using the Zimm model were 117 kDa for hRobo3 (expected monomer: 108 kDa), 373 kDa for hNELL2 (expected trimer: 296 kDa), 292 kDa for mNELL1 (expected trimer: 301 kDa) and 294 kDa for mNELL2 (expected trimer: 296 kDa).

3.4.17 Small-angle x-ray scattering (SAXS)

hRobo3 ectodomain and full-length hNELL2 samples were injected at a concentration of 10-30 μM in a Superose 6 Increase 10/300 size exclusion column equilibrated with HBS at the Advanced Photon Source beamline 18 (Bio-CAT). For mRobo1, mRobo3, and mRobo1$^{\text{Robo3-FN1}}$ ectodomains, samples with ~1 mg total of protein were injected. Data reduction and processing was performed using the BioXTAS RAW package(Hopkins, Gillilan, and Skou 2017). Guinier plots for both datasets were drawn in RAW and *P*(*r*) analysis as performed with GNOM. Molecular weights were calculated using the Vc method of Rambo and Tainer(Rambo and Tainer 2013), yielding a monomeric 100 kDa for hRobo3 ECD and trimeric 283 kDa for hNELL2. Bead models were calculated using DAMMIF(Franke and Svergun 2009). Models provided by DAMMIF were averaged and filtered by DAMAVER and DAMFILT(Volkov and Svergun 2003). Bead models shown in Figure 18C,D are produced from DAMFILT.

3.4.18 Imaging of condensates

50 µl Robo and 50 µl NELL were mixed at various concentrations in optically clear microfuge tubes and incubated at RT for 5 min to 1 hr to allow condensates to form. Tubes were initially imaged using an iPhone 8 plus camera to demonstrate the development of opalescence in solution. 5 µl of the condensate mixture was plated onto a glass slide, covered with a glass coverslip, and sealed with nail polish to prevent evaporation. Alternatively, 100 µl of the condensate mixture was pipetted into glass-bottom wells (CultureWell ChamberSLIP 16, Grace Bio-Labs). Images were taken on an Olympus DSU spinning disk confocal using a 100x objective. Time-lapse images were taken every 30 seconds for 20 minutes. For fluorescence imaging, proteins were labeled with either NHS-Fluorescein or NHS-Cy5 following protein purification. Crosslinking of fluorophores was limited to the N-terminal amine group by maintaining a pH of 6.5 buffered with 0.1 M MES and performed overnight at 4 °C. Reactions were terminated by adding 200 mM Tris to solutions and gel filtration was immediately performed on the labeled proteins to remove excess fluorophore from the solution.

3.4.19 Sedimentation assays

Phase separation of NELL2-Robo3 complexes was induced with Robo3 concentrations held at 2.5 µM and NELL2 concentrations ranging from 0.1 µM to 7.5 µM. 100 µl of NELL2 and

100 µL of Robo3 were mixed and incubated for 1 hr, followed by centrifugation at 18,000 × *g* for 10 minutes. The supernatant was carefully transferred to another microfuge tube and mixed with SDS sample loading buffer for Coomassie and western blot analysis. The pellet was washed twice in HBS, then resuspended in 200 µl HBS and mixed with SDS loading buffer.

3.4.20 HeLa cell imaging

HeLa cells were obtained from the lab of Dr. Jingyi Fei and transfected with membrane-bound Robo constructs using LipoD293 (SignaGen) or Lipofectamine 2000 (ThermoFisher) in 24-well plates containing poly-l-lysine coated glass coverslips. Transfection media were replaced with fresh media after 5 hrs of incubation. 100 nM NELL2 was added to selected wells either at the time of media replacement or 5 min prior to the following step. 24 hrs after transfection, cells were fixed for 10 minutes, washed twice, and incubated with blocking buffer containing 10% normal goat serum (NGS) in PBS. Cells were incubated overnight in 4 °C with primary antibodies (M2 anti-FLAG antibody, 1:500 dilution, Sigma; anti-HA-tag, 1:1000 dilution, Abcam) diluted in PBS containing 10% NGS. Samples were washed with PBS and incubated for 1 hr at RT with goat anti-mouse secondary antibody conjugated with AlexaFluor 568 (1:500, ThermoFisher) and goat anti-rabbit Alexa 647 (1:500, ThermoFisher). Samples were washed with PBS, then mounted on slides with Fluoromount-g mounting medium (ThermoFisher). Images were captured using the Leica SP8 at 40-60x objective within 1 week of staining.

CHAPTER 4: KIRREL HOMODIMERIZATION IN OLFACTORY SYSTEM WIRING

4.1 INTRODUCTION

This chapter contains sections from the manuscript Wang et al., *Cell Reports* (2021), where I shared co-authorship with two other investigators. In the vertebrate olfactory system, olfactory sensory neurons (OSNs) expressing the same olfactory receptor project their axons to a limited set of glomeruli in the olfactory bulb (OB), which allows for the creation of a topographic odor map in the OB (Mombaerts et al. 1996). In the mouse olfactory system, each OSN expresses a single olfactory receptor, which drives the expression of a limited number of cell surface receptors (Serizawa et al. 2006). Specifically, the expression of the cell adhesion receptors Kirrel2 or Kirrel3 in OSN populations is dependent on the odorant-induced activity of the olfactory receptors, and their expression patterns are mostly complementary: Kirrel2 expressing OSNs and Kirrel3 expressing OSNs segregate into separate glomeruli (Serizawa et al. 2006). Expression of Kirrel2 and Kirrel3 is also affected by spontaneous activity in OSNs (Nakashima et al. 2019).

The accessory olfactory system, which is found in most terrestrial vertebrate lineages and is responsible for the detection of chemosignals that guide social behavior, has a similar structure (Brignall and Cloutier 2015; Dulac and Torello 2003), where vomeronasal sensory neurons (VSNs) expressing the same vomeronasal receptor project their axons into a specific set of 6 to 30 glomeruli in the accessory olfactory bulb (AOB) (Belluscio et al. 1999; Del Punta et al. 2002; Rodriguez, Feinstein, and Mombaerts 1999). The coalescence of VSN axons into glomeruli are also shown to be dependent on Kirrel expression, where VSN activity evoked by chemosignals reduces Kirrel2 expression and increases Kirrel3 expression (Prince et al. 2013). The two Kirrel paralogs show mostly complementary expression patterns in VSNs of the VNO and in their axons innervating glomeruli of the AOB. Ablation of Kirrel2 or Kirrel3 expression in mice leads to improper coalescence of VSN axons, resulting in fewer and larger glomeruli being formed in the posterior region of the AOB, while double knock-out mice no longer have recognizable glomeruli (Brignall et al. 2018; Prince et al. 2013).

Members of the Kirrel (Neph) family of cell surface receptors were first identified in fruit flies for controlling axonal pathfinding in the optic chiasm and programmed cell death in retinal cells (Ramos et al. 1993; Wolff and Ready 1991). These molecules have also been recognized for their role in myoblast function during muscle development, and their involvement in building the blood filtration barrier in glomeruli in kidneys (Donoviel et al. 2001; Ruiz-Gómez et al. 2000). The *C. elegans* homolog, SYG-1, has been demonstrated to specify targeting of synapses (Shen and Bargmann 2003). Outside its function in the olfactory system, mammalian Kirrel3 has been shown to be a synaptic adhesion molecule necessary for the formation of a group of synapses in the hippocampus (Martin et al. 2015; Taylor et al. 2020), and is associated with autism spectrum disorders and intellectual disability (Bhalla et al. 2008; De Rubeis et al. 2014; Taylor et al. 2020).

Here, we investigate the molecular basis of Kirrel2- and Kirrel3-mediated glomerulus formation in the AOB. We present the three-dimensional structures of Kirrel2 and Kirrel3 in homodimeric complexes that reveal why Kirrels do not heterodimerize, allowing for proper adhesion and segregation of subsets of sensory axons. We engineer mutations that perturb the homophilic interactions, abolish dimerization and Kirrel-mediated cell adhesion. Finally, we introduce a non-homodimerizing amino acid substitution into the mouse *Kirrel3* allele, which leads to alterations in the wiring of the accessory olfactory system that phenocopy defects observed in *Kirrel3*$^{-/-}$ animals. These results indicate that Kirrel3 function in the control of glomeruli formation depends on ectodomain interactions mediated by Kirrel homodimerization via its first immunoglobulin domain.

4.2 RESULTS

4.2.1 Structural characterization of Kirrel2 and Kirrel3 D1 homodimers

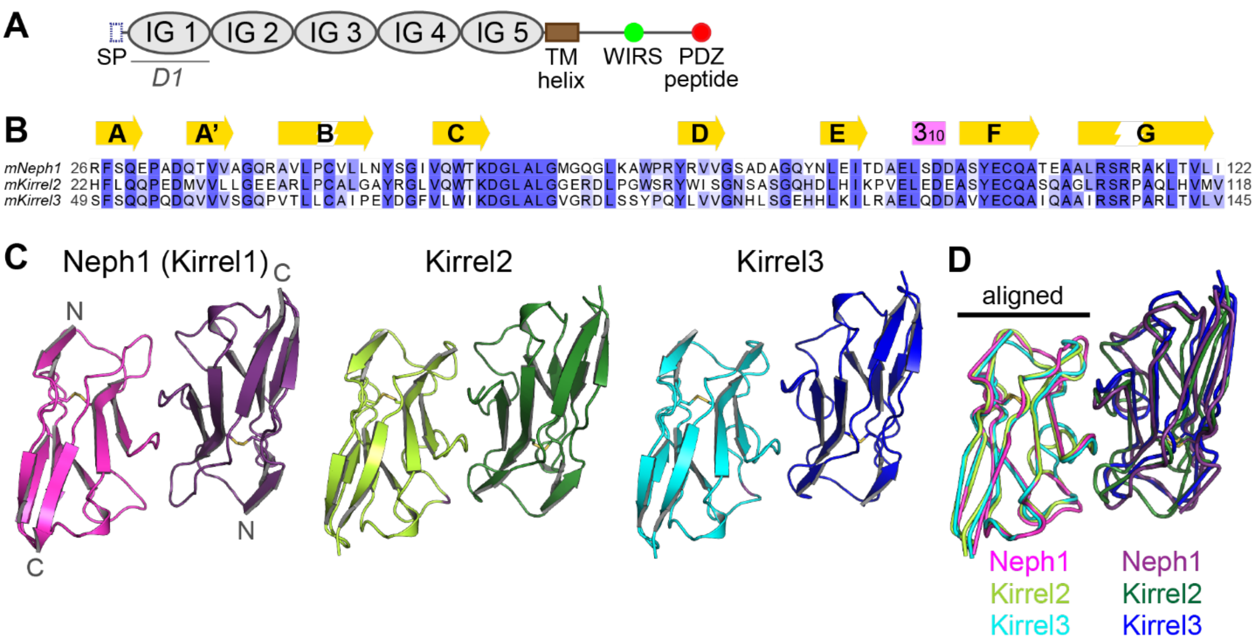

Figure 23: The three mouse Kirrel D1 homodimers share gross structural features. **A.** The conserved domain structure of Kirrels. SP: Signal peptide (N-terminal); TM: Transmembrane; WIRS: WAVE regulatory complex-interacting receptor sequence. **B.** A multisequence alignment of the mouse Kirrel D1 domains. Secondary structure elements, β-strands (yellow arrows) and a 3_{10} helix (purple box) are shown above the alignment. **C.** The three mKirrel D1 dimers shown in cartoon representation. Neph1 (Kirrel1) homodimer structure is from Özkan et al. (2014; PDB ID: 4OFD). **D.** The three mKirrel D1 homodimers are overlayed by aligning the chains shown on the left.

It has been proposed that Kirrel2 and Kirrel3 regulate the coalescence of OSNs and VSNs into glomeruli by homophilic adhesion through their ectodomains (Prince et al. 2013; Serizawa et al. 2006). Vertebrate Kirrel proteins have been shown to form homodimers, but not heterodimers (Gerke et al. 2005; Serizawa et al. 2006), which may be important for axonal segregation into distinct glomeruli. Previously, we determined the crystal structure of mouse Kirrel1 (also known as Neph1) at 4 Å resolution covering the first two immunoglobulin domains, and showed that homodimerization occurs by an interaction between the first domains (D1) of each monomer (Özkan et al. 2014). Due to limited resolution, however, the Kirrel1 electron density was missing for most side chains and details of the interaction interface could not be documented. Vertebrate Kirrels are remarkably similar in their extracellular regions, containing five immunoglobulin domains (Figure 23A) with sequence identities of 53 to 56% for D1 among the three mouse Kirrels (Figure 23B).

In order to explain the molecular basis of homophilic interactions in the absence of heterophilic binding between the Kirrel paralogs, we determined the crystal structures of Kirrel2 and Kirrel3 D1 homodimers at 1.8 Å and 2.1 Å resolution, respectively (Figure 23C and Table 2). When superimposed, the Kirrel2 and Kirrel3 D1 domains have root-mean-square displacements (rmsd) of 1.2 Å to the Kirrel1 D1 domain, and align with an rmsd of 1.0 Å to each other (all Cα atoms). Comparison of the three Kirrel D1 homodimers show that Kirrels dimerize using the same interface and the dimeric architectures are shared (Figure 23D). The three D1 homodimers align with rmsd values of 1.3 to 1.6 Å. Similar dimers have been observed for homodimeric complexes formed by fruit fly Kirrel homologs, Rst and Kirre (Duf), and the heterodimeric SYG-1-SYG-2 complex, the *C. elegans* Kirrel homolog bound to Nephrin-like SYG-2 (Özkan et al. 2014). This distinctive interaction architecture uses the curved *CFG* face of the IG fold to create dimers, and was recently identified to be common to a group of cell surface receptors involved in neuronal wiring, including Dprs, DIPs, IGLONs, Nectins and SynCAMs, as well as Kirrels and Nephrins (Cheng, Park, et al. 2019).

Out of 21 amino acids found in three structures to be at the dimer interface, ten are invariable among the three mouse Kirrels, mostly in the region following the *C* strand within the sequence KDGLALG, and the *F* and *G* strands. The conserved Gln128 (Kirrel3 numbering) in the *F* strand makes hydrogen bonds to the main chain of the conserved stretch in the *CD* loop in all

Table 2, related to Figure 24: Data and refinement statistics for x-ray crystallography.

	Mouse Kirrel2 D1	**Mouse Kirrel3 D1**
Data Collection		
Beamline	SSRL 12-2	APS 24-ID-E
Space Group	$C2$	$P6_3$
Cell Dimensions		
a, b, c (Å)	109.14, 48.44, 44.10	63.24, 63.24, 347.81
α, β, γ (°)	90, 107.01, 90	90, 90, 120
Twin law (Fraction)	–	-k,-h,-l (0.31)[†]
Resolution (Å)	50-1.80 (1.83-1.80)*	50-1.95 (1.98-1.95)
R_{sym} (%)	5.6 (17.3)	11.4 (85.3)
$\langle I\rangle/\langle\sigma(I)\rangle$	21.9 (5.3)	14.6 (1.9)
$CC_{1/2}$ in the highest resolution bin	0.945	0.617
Completeness (%)	94.2 (69.1)	99.9 (99.8)
Redundancy	3.3 (2.6)	4.4 (4.4)
Refinement		
Resolution (Å)	50-1.80 (1.90-1.80)*	50.1-1.95 (1.98-1.95)
Reflections	19,361	56,984
R_{cryst} (%)	15.49 (19.50)	16.02 (22.95)
R_{free} (%)**	18.09 (25.18)	19.53 (27.48)
Number of atoms		
Protein	1633	6408
Ligand	2	8
Water	337	336
Average B-factors (Å^2)		
All	20.1	38.1
Protein	18.1	38.5
Ligand/Glycans	11.8	44.9
Solvent	30.0	31.4
R.m.s. deviations from ideality		
Bond Lengths (Å)	0.004	0.005
Bond Angles (°)	0.632	0.684
Ramachandran plot		
Favored (%)	98.52	96.19
Outliers (%)	0.00	0.00
Rotamer Outliers (%)	0.00	0.14
All-atom Clashscore[†]	0.00	3.43

* The values in parentheses are for reflections in the highest resolution bin.

** 5% of reflections (971 for Kirrel2 and 2846 for Kirrel3) were not used during refinement for cross validation.

[†] Clashscores and twin fraction were calculated by phenix.refine (*Phenix* version 1.19.1-4122).

three Kirrel structures. Beyond this similarity, there are stark differences in the Kirrel2 and Kirrel3 interfaces that likely underlie exclusive homodimerization. Kirrel2 has a hydrogen bonding network at the core of the interface, centered at Gln52 at the two-fold symmetry axis (Figure 24A),

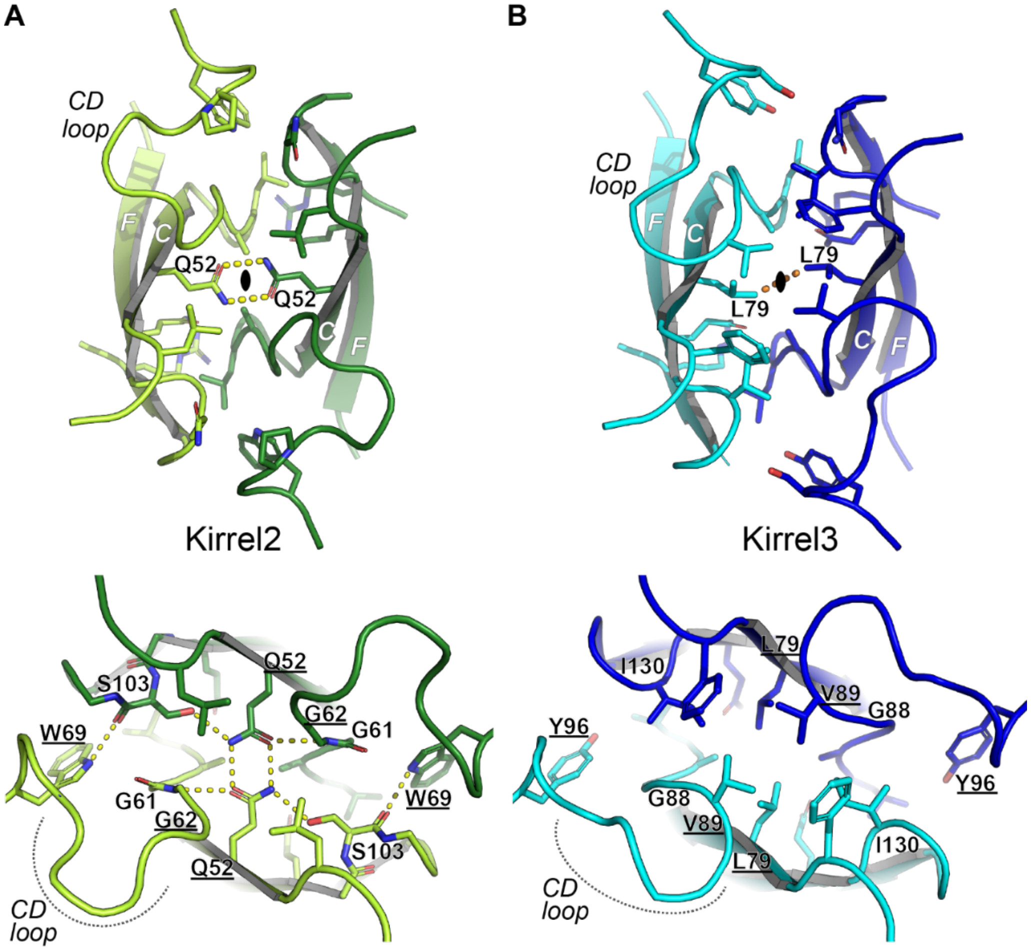

Figure 24: Kirrel2 and Kirrel3 have incompatible chemistries at their dimerization interfaces.

A. Kirrel2 homodimerization interface. The closed oval represents the two-fold symmetry axis surrounded by the bidentate hydrogen bonding (yellow dashes) of two Q52 residues from Kirrel3 monomers. The interface includes an extensive set of hydrogen bonds. **B.** Kirrel3 homodimerization interface. None of the hydrogen bonds depicted in (A) are present in the Kirrel3 interface. The hydrogen bonds between the Q52 side chains at the Kirrel2 dimer symmetry axis are replaced by van der Waals contacts between the L69 side chains (orange dashes) in Kirrel3. The loop connecting the C and D strands are significantly different between the two Kirrel structures. Underlined amino acids vary among ancestral vertebrate sequences and are strong candidates to be specificity determinants.

while the hydrogen bonding network is missing in Kirrel3, which has Leu79 at the symmetry axis instead (Figure 24B). The polar vs. hydrophobic interactions at the Kirrel2 and Kirrel3 interfaces, respectively, would preclude heterodimerization of the two Kirrels.

4.2.2 Evolutionary origins of vertebrate Kirrels and homodimeric specificity

To understand how Kirrel homodimeric specificities arose in vertebrates, we next analyzed the evolutionary histories of Kirrels. All major bilaterian taxa contain Kirrel homologs, which preserve the five-IG domain extracellular region and a cytoplasmic PDZ peptide. We created a maximum likelihood (ML) phylogeny for Kirrels using a multiple sequence alignment of 90 ectodomains (Figure 25A). The three vertebrate Kirrels arose as a result of gene duplications and are more closely related to each other than to invertebrate Kirrels. Kirrel duplication in invertebrates is rare, with one notable exception being *Drosophila*, which has two Kirrels (Rst and Kirre). After gene duplications within vertebrates, there have been several gene losses; this, combined with extensive sequence divergence between vertebrate and invertebrate Kirrels, makes it difficult to accurately reconstruct the branching order of vertebrate Kirrels. Nevertheless, we observe strong bootstrap values for cyclostome Kirrel1 forming a single clade with gnathostome Kirrel1 and excluding Kirrel2 and Kirrel3. This strongly implies that Kirrel2 and Kirrel3 arose from a gene duplication within gnathostomes and are more closely related to each other than to Kirrel1 in support of our ML tree.

To understand the evolution of Kirrel interaction specificity, we mapped variable interface residues in separate Kirrel clades (Figure 25A and B). The sequence logos show that Kirrel1 and Kirrel2 are more similar at their dimerization interfaces, while Kirrel3 diverged and mutated key positions to non-polar amino acids. Surprisingly, much of the variability observed at these positions in vertebrate Kirrels are also seen in invertebrate Kirrels, suggesting that these sites are permissive for multiple modes and specificities of binding.

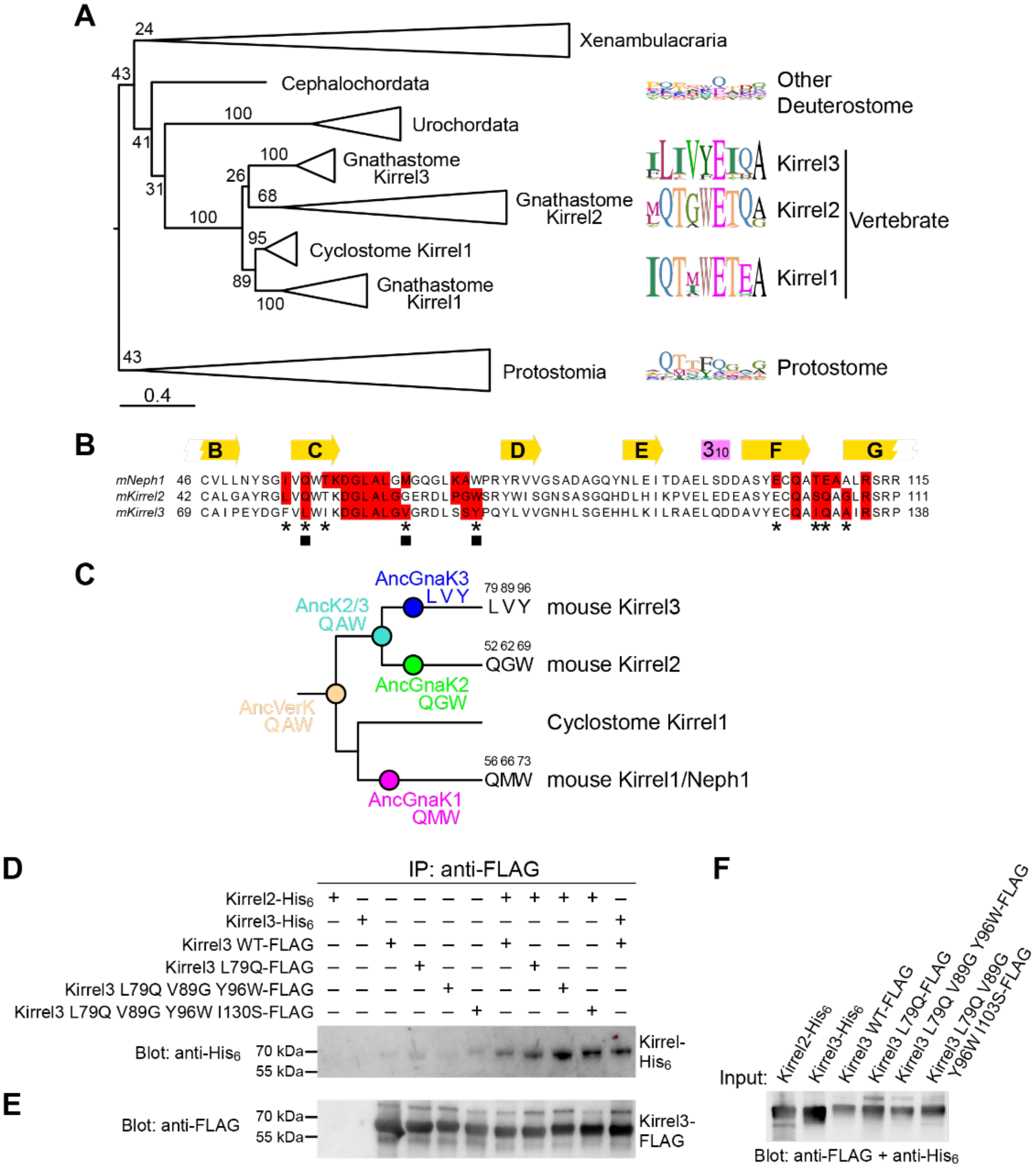

Kirrel2-His6	+	–	–	–	–	–	+	+	+	+	–
Kirrel3-His6	–	+	–	–	–	–	–	–	–	–	+
Kirrel3 WT-FLAG	–	–	+	–	–	–	+	–	–	–	+
Kirrel3 L79Q-FLAG	–	–	–	+	–	–	–	+	–	–	–
Kirrel3 L79Q V89G Y96W-FLAG	–	–	–	–	+	–	–	–	+	–	–
Kirrel3 L79Q V89G Y96W I130S-FLAG	–	–	–	–	–	+	–	–	–	+	–

Figure 25: Phylogenetic analysis of Kirrels.

(Figure 25 continued) **A.** Maximum likelihood tree for Kirrels. The scale bar below represents 0.4 substitutions per site. Numbers on the tree are bootstrap values supporting the adjacent node. The sequence logos to the right show the prevalence of amino acids in selected positions at the Kirrel dimerization interface for specific taxa, placed next to their branch in the phylogenetic tree. Sequence logos were calculated using 26 vertebrate Kirrel1, 17 vertebrate Kirrel2, 22 vertebrate Kirrel3, 8 other deuterostome, and 17 protostome sequences. **B.** Sequence alignment showing all amino acids at the interface: red boxes; 4 Å cutoff used for identifying an interface amino acid. The selected residues used in sequence logos in (A) are marked with an asterisk below. Three positions at the interface that vary among ancestral sequences highlighted in (C) are labeled by closed squares. **C.** The three varying residues among sequence reconstructions of the three ancestral gnathostome Kirrels, the Kirrel2/3 ancestor and the ancestral vertebrate Kirrel are shown on the tree. These positions are underlined in the structural views of the interface in Figure 2. **D.** FLAG-tagged WT and mutant Kirrel3 ectodomains were used to immunoprecipitate hexahistidine-tagged WT Kirrel2 or Kirrel3 ectodomains. Only very low levels of WT Kirrel2-His$_6$ can be pulled down with WT Kirrel3-FLAG; the pulldown becomes increasingly efficient with the Kirrel3 L79Q mutation and the triple and quadruple mutations. **E.** The anti-FLAG blot of the samples eluted with FLAG peptide show similar levels of Kirrel3-FLAG captured on anti-FLAG resin in all samples where Kirrel3 FLAG (WT or mutant) were included. **F.** The expression levels of His$_6$- and FLAG-tagged Kirrels observed with anti-FLAG and anti-His$_6$ antibodies.

Next, we inferred ancestral sequences for Kirrel D1 domains in the vertebrate and gnathostome nodes on the phylogenetic tree (Figure 25C). There are nine variable positions between the common Kirrel2/Kirrel3 ancestor and the ancestral gnathostome Kirrel3. Three of these positions are at the interface (labeled with closed squares in Figure 25B), including two that are part of the hydrogen bonding network seen in Kirrel2 (Q52 and W69), and one contributing strongly to the hydrophobic nature of the Kirrel3 interface (V89 in Kirrel3, G62 in Kirrel2) (see underlined amino acids in structures in Figure 24). Overall, these ancestral sequences support our structural observations that the gnathostome Kirrel3 homodimer interface gained non-polar interactions which resulted in loss of interactions with its Kirrel2 paralogs.

Next, we inferred ancestral sequences for Kirrel D1 domains in the vertebrate and gnathostome nodes on the phylogenetic tree (Figure 25C). There are nine variable positions between the common Kirrel2/Kirrel3 ancestor and the ancestral gnathostome Kirrel3. Three of

these positions are at the interface (labeled with closed squares in Figure 25B), including two that are part of the hydrogen bonding network seen in Kirrel2 (Q52 and W69), and one contributing strongly to the hydrophobic nature of the Kirrel3 interface (V89 in Kirrel3, G62 in Kirrel2) (see underlined amino acids in structures in Figure 24). Overall, these ancestral sequences support our structural observations that the gnathostome Kirrel3 homodimer interface gained non-polar interactions which resulted in loss of interactions with its Kirrel2 paralogs.

To confirm that these residues we identified through the structural and phylogenetic analyses contribute to dimerization specificity, we tested for the co-immunoprecipitation of wild-type Kirrel2 with mutants of Kirrel3 converting the nonpolar "specificity" residues to their corresponding amino acids in Kirrel2. For mutating Kirrel3, we selected the three previously identified residues (L79, V89, and Y96), as well as Ile130, which in Kirrel2 corresponds to Ser103 and supports the hydrogen bonding network at the homodimerization interface (Figure 24). We observed that Kirrel2 was pulled down by the single (L79Q), triple (L79Q V89G Y96W), and quadruple (L79Q V89G Y96W I130S) mutants of Kirrel3 (Figure 25D), indicating that converting the hydrophobic "specificity" layer in Kirrel3 to polar, hydrogen-bonding residues likely allows for interactions with Kirrel2.

4.2.3 Mutagenesis of the Kirrel2 and Kirrel3 D1 dimerization interfaces

To confirm that the Kirrel2 and Kirrel3 D1 interfaces observed in crystal structures mediate dimerization in solution, we set out to mutate these interfaces and test for loss of dimer formation. In size exclusion chromatography (SEC) experiments, Kirrel2 D1 and Kirrel3 D1+D2 proteins elute at a volume that roughly corresponds to that of their dimeric sizes (Figure 26A and B). This dimerization is concentration-specific; size-exclusion runs with diluted samples elute at later volumes, indicating a fast equilibrium between dimeric and monomeric forms of Kirrels. Interface mutations of mouse Kirrel2 D1 and Kirrel3 D1+D2 were tested for dimerization at various concentrations based on SEC elution volumes, which allowed us to rank these mutations for their effect to decrease or abolish dimer formation. For both Kirrel2 and Kirrel3, mutation of the same site, Q101 for Kirrel2 and Q128 for Kirrel3, to alanine abolished dimerization (Figure 26A and B). Alanine mutations of a set of equivalent positions at the dimerization interface of both Kirrels strongly diminished homodimerization: L58/L85, W69/Y96, R108/R135 (Kirrel2/Kirrel3 numbering). The energetic hot spot formed by these four residues create a continuous volume (Figure 26C). Surprisingly, the residue at the dimerization two-fold axis, Q52 for Kirrel2 and L79 for Kirrel3, which is likely important for specificity, is less crucial for binding energetics. In fact, the variable residues necessary for establishing dimerization specificity appear to cause smaller losses of binding energy when mutated, compared to the conserved residues at the hot spot. Overall, these mutagenesis experiments confirm that the interfaces observed in the crystal structures mediate dimer formation in solution.

4.2.4 Kirrel2 and Kirrel3 homophilic adhesion is dependent on D1

While we have shown that the major dimerization interface for Kirrel homologs are within the N-terminal domain (D1) (Özkan et al. 2014, and above), it is not known if the other four domains can also cause dimerization in vertebrate Kirrels. In support of additional dimerization sites, Gerke et al. (2003) reported evidence that dimerization was not limited to any single domain within Kirrel1 and the related Nephrin. Furthermore, a large number of human mutations affecting Kirrel3 function in the ectodomain, but outside D1, have been identified (summarized in Taylor et al. 2020). To test whether Kirrel ectodomains can form dimers using interfaces we did not identify in our crystal structures, we used analytical ultracentrifugation to quantify dimerization of Kirrel2 and Kirrel3 ectodomains and one D1 interface mutant, Kirrel3 Q128A. We performed sedimentation velocity experiments at several concentrations and observed that both WT Kirrel ectodomains exist in a monomer-to-dimer equilibrium, confirming our SEC results (Figure 26D). Kirrel3 ectodomain with the D1 mutation Q128A showed no signs of dimerization at any concentration (Figure 26D), implying that no additional interface mediates dimerization.

Kirrel2 and Kirrel3 have been shown to mediate homophilic cell adhesion, which was suggested as necessary for their function in the regulation of olfactory sensory neuron axonal coalescence into glomeruli and synaptic specification in the hippocampus. We therefore examined the effect of non-dimerizing mutations on Kirrel-dependent adhesion using a cell aggregation assay. Suspension S2 cells were transfected with transmembrane constructs containing Kirrel ectodomains, attached to the transmembrane helix of Neurexin, followed by a cytoplasmic EGFP. We observed strong aggregation in transfected cultures, indicating that Kirrel2 and Kirrel3 form trans-homodimers that aggregate S2 cells (Figure 26E). When the Kirrel2 and Kirrel3 constructs carried mutations that abolish or strongly diminish dimerization through the D1 interface, such as Q128A in Kirrel3, cell aggregation was also abolished. However, an alanine mutation at the "specificity site" Kirrel2 Q52 did not abolish cell aggregation, as the soluble D1+D2 construct with this mutation still behaved as a dimer in SEC (Figure 26A). The analytical ultracentrifugation and cell aggregation experiments demonstrate that the D1 interface we observed in our crystal structures is required for Kirrel homodimerization, and a second interaction site within the ectodomains is either very weak to detect or does not exist.

4.2.5 Kirrel ectodomains form elongated homodimers mediated by D1 interactions

As Kirrels are adhesion molecules carrying signaling motifs, the tertiary structure and conformational states of their ectodomains are relevant for their signaling and adhesive properties.

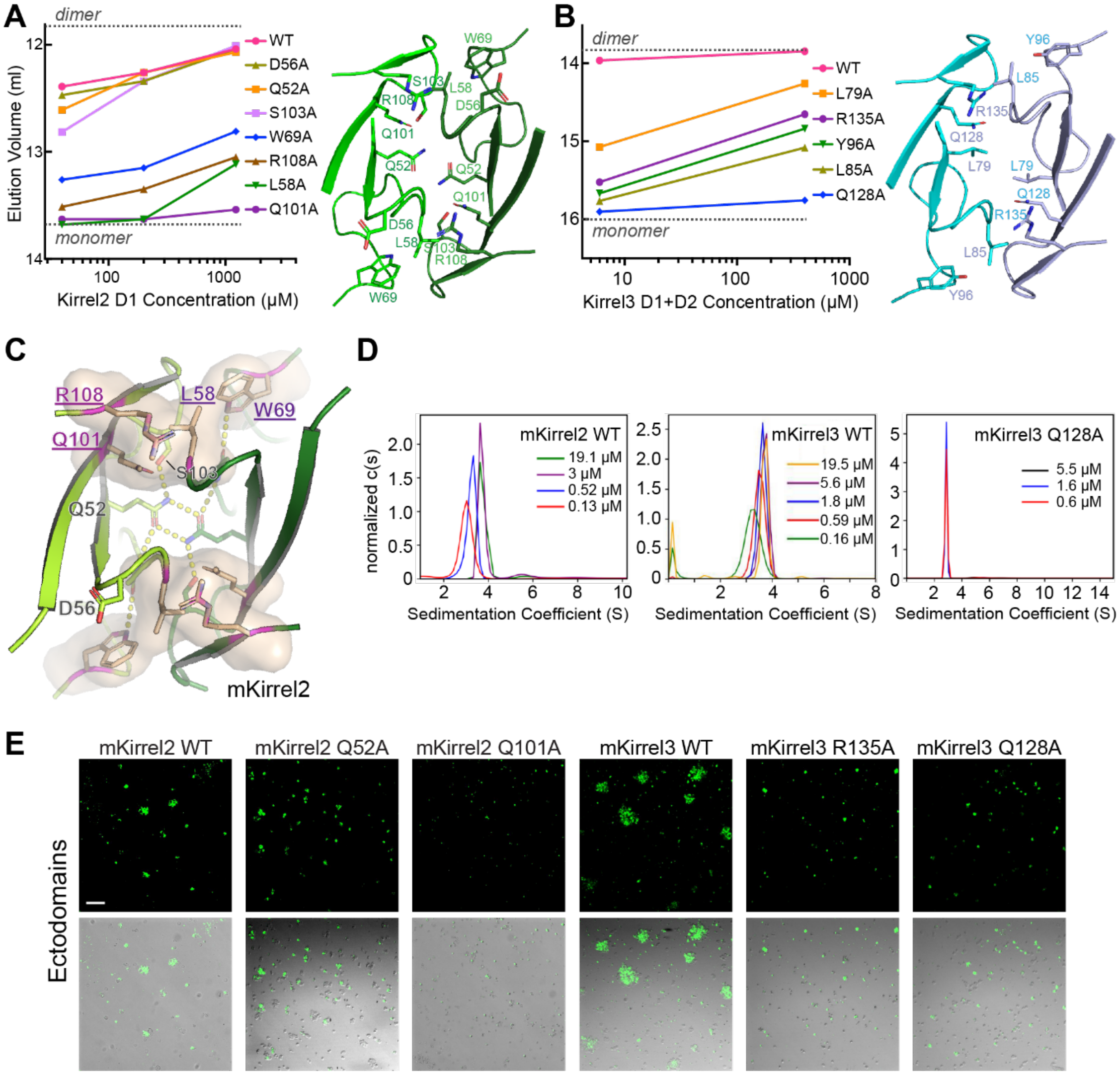

Figure 26: Mutational analysis of the Kirrel2 and Kirrel3 homodimerization interfaces. **A, B.** SEC elution volumes for wild-type and mutant Kirrel2 D1 (A) and Kirrel3 D1+D2 (B) loaded at multiple concentrations on the columns. A Superdex 75 10/300 column was used for the Kirrel2 D1 runs (left) and a Superdex 200 Increase 10/300 column was used for the Kirrel3 D1+D2 runs, both with a column volume of 24 ml. Expected monomeric and dimeric elution volumes are marked by dashed lines on the plots. The structural views to the right show the locations of the amino acids mutated. **C.** Four residues observed to be energetically important for Kirrel dimerization mapped onto Kirrel2 structure and shown as a surface (residue names purple and underlined). **D.** Sedimentation velocity results for mouse Kirrel2 WT (left), Kirrel3 WT (middle) and Kirrel3 Q128A (right) ectodomains performed at several initial protein concentrations, showing lack of dimerization for the Q128A mutant. K_D for WT mKirrel2 and mKirrel3 refine to 0.9 μM [0.2 μM, 3.5 μM] and 0.21 μM [0.11 μM, 0.36 μM] (68.3% confidence intervals are shown in brackets). **E.** Cell aggregation assay for Kirrel2 and Kirrel3, WT and mutants, fused to intracellular GFP, performed with S2 cells. Scale bar, 100 μm.

To gain insights into the three-dimensional structure of Kirrel ectodomains, we studied Kirrel2 and Kirrel3 ectodomains in solution using an SEC-SAXS-MALS setup, including the Kirrel3 Q128A mutant (Figure 27 and Table 3). For all ectodomains tested by SAXS (small-angle x-ray scattering), shapes of pair distance distributions, $P(r)$, show strongly rod-like character, rather than globular or other shapes (Figure 27A, B). Kirrel2 and Kirrel3 homodimers have maximum dimensions ($D_{\max}$) of 39 and 35 nm, respectively, while Kirrel3 Q128A has a $D_{\max}$ of 21 nm, suggesting that Kirrel dimers are nearly double the length of the monomer. The accompanying MALS (multi-angle light scattering) data recapitulate our conclusions from pure SEC runs, where concentrated wild-type Kirrels have molar masses matching dimeric sizes and diluted Kirrel3 samples yield intermediate values between predicted monomer and dimer masses, while Kirrel3 Q128A is a pure monomer (Table 4). These results agree with our elongated Kirrel model where only D1 domains interact between Kirrel monomers, and support a D1-D1, or N-terminal tip-to-tip, interaction model of Kirrel homodimerization.

A prominent feature common to Kirrel2, Kirrel3, and Kirrel3 Q128A ectodomains observed in dimensionless Kratky plots for SAXS data (Figure 27B) is flexibility, likely reflecting significant interdomain movements. While this may complicate low-resolution modeling of the ectodomains, we used *DAMMIF* (Franke and Svergun 2009) to create ab-initio bead models. Bead models for Kirrel2 and Kirrel3 appear as a thin V with a vertex angle of approximately 115°, while a bead model for Kirrel3 Q128A is a straight rod that is as long as each of the “wings” of the Kirrel2 and Kirrel3 models. These conformations agree with our structural models of a fixed angle of Kirrel2 and Kirrel3 dimerization defined by the D1-D1 binding interface.

Table 3, related to Figure 27: Data collection details and analysis statistics for SAXS experiments

	mKirrel2 ECD	**mKirrel3 ECD**	**mKirrel3 ECD Q128A**
Data Collection and Sample Details			
Experiment setup	SEC-SAXS-MALS		
Instrument	BioCAT facility at APS beamline 18-ID with Pilatus3 X 1M (Dectris) detector		
Wavelength (Å)	1.033		
Camera length (m)	3.655		
q-measurement range (Å^{-1})	0.0044 to 0.35		
Exposure time (s)	0.5		
Exposure period (s)	1.0		
Flow rate (ml/min)	0.6		
Chromatography column	Superdex 200 10/300 Increase		
Buffer	10 mM HEPES pH 7.2, 150 mM NaCl		
Temperature	22°C		
Software	BioXTAS RAW version 2.0.2		
Loading concentration (mg/ml)	3.7	5.0	2.0
Loading volume (μl)	425		
Structural Parameters			
Guinier Analysis*			
$I(0)$ (cm^{-1})	0.0231 ± 0.000186	0.0596 ± 0.000169	0.0247 ± 0.000082
R_g (Å)	88.67 ± 1.28	93.17 ± 0.49	54.42 ± 0.30
q range (Å^{-1})	0.005 to 0.0133	0.0047 to 0.0124	0.005 to 0.0227
$q_{min}R_g$ to $q_{max}R_g$	0.444 to 1.178	0.439 to 1.158	0.272 to 1.237
Coefficient of Correlation, R^2	0.981	0.996	0.991
$P(r)$ Analysis (from GNOM**)			
$I(0)$ (cm^{-1})	0.0235 ± 0.000234	0.0595 ± 0.000155	0.0251 ± 0.000085
R_g (Å)	95.97 ± 2.21	95.59 ± 0.40	58.69 ± 0.31
D_{max} (Å)	390	345	213
q range (Å^{-1})	0.0050 to 0.3497	0.0047 to 0.3497	0.0050 to 0.3497
χ^2	0.856	1.050	1.104
Porod Volume estimate (Å^3)	152000	157000	109000
Molecular weight based on volume of correlation (V_c)	80,800	94,600	45,400

* Performed in BioXTAS RAW (Hopkins, J.B. *et al*. (2017) *J Appl Crystallogr* **50**, 1545-1553).

** Svergun, D.I. (1992). *J Appl Crystallogr* **25**, 495-503.

Table 4, related to Figure 27. Data collection details and analysis statistics for MALS experiments.

	mKirrel2 ECD	**mKirrel3 ECD Q128A**	**mKirrel3 ECD WT run 1**	**mKirrel3 ECD WT run 2**	**mKirrel3 ECD WT run 3**
Experiment Type	SEC-SAXS-MALS				
Instrument	DAWN HELEOS with Optilab T-rEX at BioCAT (APS beamline 18-ID)				
Wavelength (nm)	660 (for light scattering) and 658 (for RI)				
Flow rate (ml/min)	0.6				
Chromatography column	Superdex 200 10/300 Increase				
Buffer	10 mM HEPES pH 7.2, 150 mM NaCl				
Refractive index of the solvent (assumed)	1.331				
Temperature	25°C				
Software	ASTRA version 7.3.2.19 (Wyatt)				
Loading volume (μl)	425				
Loading concentration (mg/ml)	3.7	2.0	5.0	2.0	0.5
dn/*dc**	0.182	0.181	0.181	0.181	0.181
M_n**	97,200 (±6.2%)	54,830 (±7.5%)	111,100 (±6.5%)	105,400 (±4.6%)	97,910 (±5.2%)
M_w†	97,630 (±6.2%)	55,200 (±7.3%)	111,400 (±6.5%)	105,500 (±4.6%)	98,170 (±5.2%)

* *dn*/*dc* values are estimated based on predicted N-linked glycosylation content.

** Number-averaged molar mass.
† Weight-averaged molar mass.

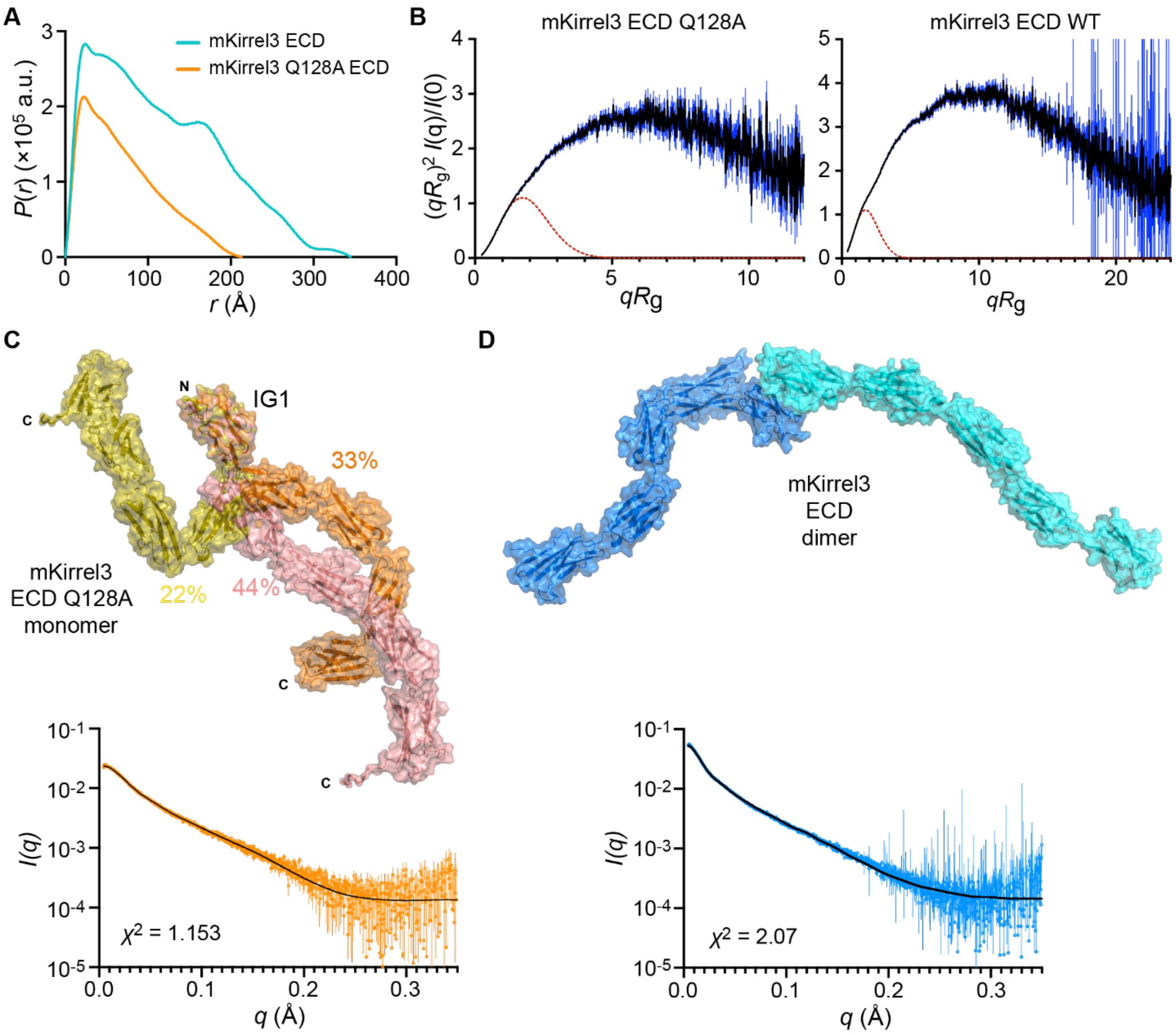

Figure 27: SAXS analysis of Kirrel ectodomains.

A. Pair distance distributions, *P*(*r*), for mKirrel3 ectodomains, WT and Q128A. WT Kirrel3 is a longer molecule than Kirrel3 Q128A since it has a larger $D_{\max}$ (35 nm vs. 21 nm). **B.** Dimensionless Kratky plots for mKirrel3 ectodomains; blue vertical lines are measured errors. Dashed red lines show predicted plots for rigid, globular molecules with the same R_g. **C.** Ensemble model fitting of SAXS data for mKirrel3 Q128A ectodomain using *EOM*. The three-model ensemble with contributions are indicated as percentages next to the models. The scattering profile predicted from the ensemble model (black) closely matches observed scattering data (orange; measurement errors are indicated by vertical bars). **D.** *SASREF* model of mKirrel3 WT ectodomain dimer, and its predicted scattering (black) overlayed on observed SAXS data (blue; measurement errors are indicated by vertical bars).

Next, we attempted to model Kirrel ectodomains using an ensemble representation with *EOM* from the *ATSAS* suite (Tria et al. 2015), where flexibility was allowed between five rigid-body-defined IG domains, which were available through our high-resolution Kirrel D1 structures or were modeled (Domains 2 to 5) based on similar immunoglobulin domain templates. *EOM* can explain observed SAXS profiles for the monomeric Kirrel3 Q128A using a three-model ensemble that has theoretical scattering matching observed data with high fidelity ($\chi^2 = 1.15$, Figure 27C). While the homodimer also shows strong flexibility based on the Kratky analysis (Figure 27B), ensemble modeling did not yield an equally satisfactory model for explaining WT Kirrel3 scattering data, possibly due to the presence of monomeric species in solution and a higher-degree of flexibility caused by movements between ten, rather than five domains. For the dimeric Kirrel3 WT SAXS data, we used *SASREF* from the same package to allow for interdomain flexibility within one model (Petoukhov and Svergun 2005) (Figure 27D). When the resulting model was aligned to the SAXS bead model from *DAMMIF*, we observed a strong overlap, supporting the validity of our SAXS bead models as well as our model of Kirrel tip-to-tip dimerization. These results further point to a lack of secondary dimerization sites.

4.2.6 Kirrel3 Q128A mutation causes defects in glomerulus formation in the AOB

In order to assess whether the Kirrel D1-to-D1 model of homophilic adhesion contributes to Kirrel3 function in wiring the nervous system, a graduate student, Neelima Vaddadi, working under the supervision of our collaborator, Dr. Jean-François Cloutier, examined the effect of abolishing Kirrel3 dimerization on vomeronasal sensory neuron axon targeting in the AOB. We engineered mice expressing the Kirrel3 Q128A amino acid substitution, which abolishes Kirrel3 dimerization, using CRISPR technology (Figure 28A-C). An analysis of Kirrel3 protein in lysates extracted from brain samples of wild-type and *Kirrel3*$^{Q128A/Q128A}$ mice reveals that Kirrel3 Q128A

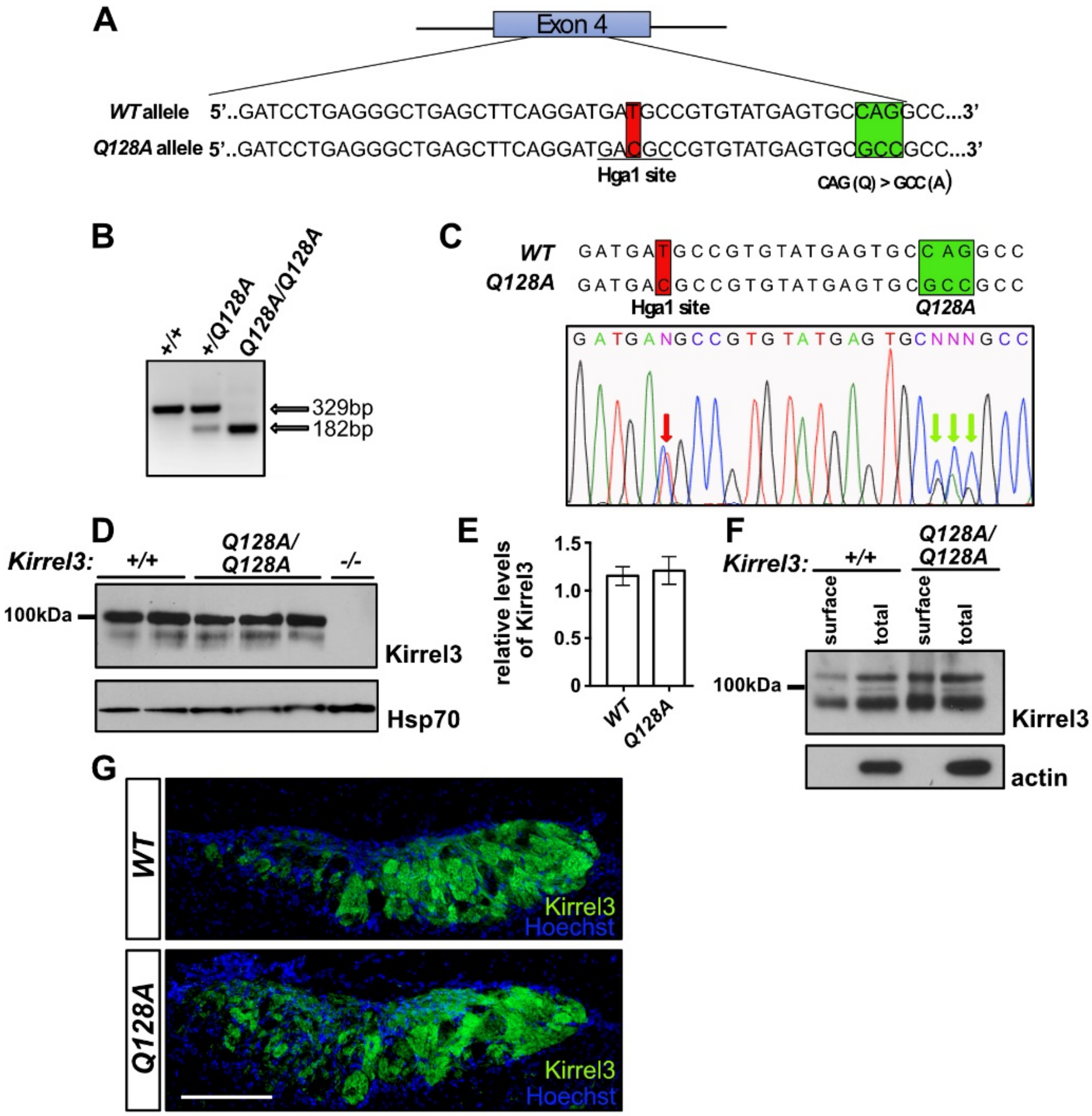

Figure 28: Characterization of the Kirrel3 Q128A mouse.

A. Diagram of the generation of the *Kirrel3 Q128A* mouse. Mice carrying a modified *Kirrel3* allele containing mutations that modify amino acid 128 from a glutamine (Q) to an alanine (A), as well as a silent mutation introducing an HgaI restriction enzyme cutting site for genotyping purposes, were generated. Green square: Q to A mutations. Red square: mutation creating an HgaI restriction site. **B-C.** Identification of the *Kirrel3 Q128A* allele by restriction enzyme digest and DNA sequencing. Digestion with HgaI (B) and DNA sequencing (C) of a PCR fragment from exon 4 of the *Kirrel3* allele demonstrate the presence of the newly introduced HgaI restriction site. DNA sequencing also reveals the

(Figure 28 continued) presence of the three nucleotide substitutions resulting in the Q to A amino acid substitution in a *Kirrel3*$^{+/Q128A}$ mouse. The red arrows in the electropherogram in C indicate the overlapping peaks caused by the nucleotide substitutions in one of the *Kirrel3* alleles. **D-E.** Quantification of Kirrel3 protein by western blot of brain lysate collected from *Kirrel3*$^{+/+}$ and *Kirrel3*$^{Q128A/Q128A}$ mice shows that similar levels of Kirrel3 and Kirrel3 Q128A levels are expressed in the brain of these mice, respectively. Data were analyzed using unpaired *t*-test; *n*=3 for *Kirrel3*$^{+/+}$ and 4 for *Kirrel3*$^{Q128A/Q128A}$ mice. **F.** Surface membrane distribution of Kirrel3 Q128A in acute brain slices. Western blots of acute brain slice lysate collected from *Kirrel3*$^{+/+}$ and *Kirrel3*$^{Q128A/Q128A}$ mice following incubation with biotin and isolation of surface proteins by batch streptavidin chromatography. Both Kirrel3 and Kirrel3 Q128A are distributed to the cell surface. **G.** Immunohistochemistry on sagittal sections of the AOB from *Kirrel3*$^{+/+}$ and *Kirrel3*$^{Q128A/Q128A}$ adult mice labelled with antibodies against Kirrel3 and Hoechst. The Kirrel3 and Kirrel3 Q128 proteins can be detected in subsets of glomeruli in both the anterior and posterior regions of the AOB in *Kirrel3*$^{+/+}$ and *Kirrel3*$^{Q128A/Q128A}$ mice, respectively. Scale bar is 200 μm.

is expressed at comparable levels to the wild-type protein in the brain (Figure 28D,E). Additionally, cell surface biotinylation assays on brain slices from control and *Kirrel3*$^{Q128A/Q128A}$ mice, combined with flow cytometry of HEK293T cells transfected with full-length WT and Q128A Kirrel3, reveals that the mutant protein is properly trafficked to the cell's surface (Figure 28F).We then investigated the expression patterns of Kirrel3 Q128A on VSN axons innervating the AOB. Kirrel3 is expressed on subsets of VSN axons innervating glomeruli throughout the AOB with a large proportion of glomeruli in the posterior region expressing Kirrel3 (Prince et al. 2013). Sagittal sections of the AOB stained for Kirrel3 demonstrated a clear localization of Kirrel3 in a majority of glomeruli in the posterior region of the AOB in both wild-type and *Kirrel3*$^{Q128A/Q128A}$ mice (Figure 28G). Since *Kirrel3*$^{-/-}$ mice show altered glomeruli structure in the posterior region of the AOB (Prince et al. 2013), we next performed a detailed analysis of the glomerular layer in *Kirrel3*$^{Q128A/Q128A}$ mice. To visualize and delineate glomeruli, sagittal sections of the AOB of control and *Kirrel3*$^{Q128A/Q128A}$ mice were stained with anti-VGLUT2, which marks excitatory pre-synaptic terminals in the AOB. As previously observed in *Kirrel3*$^{-/-}$ mice (Prince et al. 2013), the

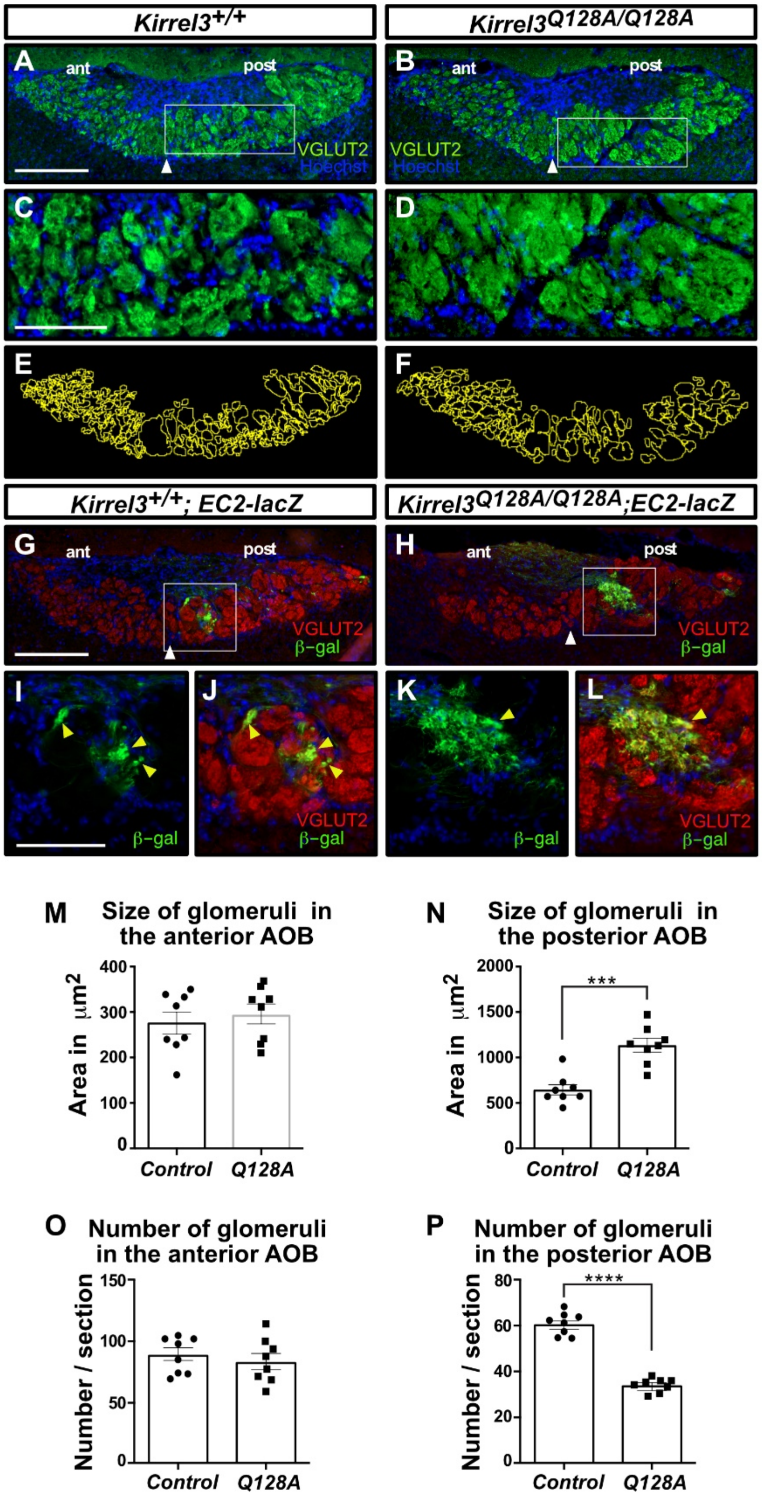

Figure 29: Glomeruli structure is altered in the AOB of Kirrel3$^{Q128A/Q128A}$ mice.

(Figure 29 continued) **A-F.** Parasagittal sections of the AOB from adult *Kirrel3*$^{+/+}$ (A,C) and *Kirrel3*$^{Q128A/Q128A}$ (B,D) mice, labelled with a VGLUT2 antibody and Hoechst (A-D). Higher magnification of outlined regions in A and B are shown in C and D, respectively. Glomeruli in the posterior region of the AOB in *Kirrel3*$^{Q128A/Q128A}$ mice appear significantly larger and less numerous when compared to *Kirrel3*$^{+/+}$ mice (E,F). White arrowheads denote the boundary between the anterior (ant) and posterior (post) regions of the AOB. **G-L.** Parasagittal sections of the AOB from adult *Kirrel3*$^{+/+}$*; EC2-lacZ* (G) and *Kirrel3*$^{Q128A/Q128A}$*; EC2-lacZ* (H) mice, labelled with a VGLUT2 (red) and □-galactosidase (green) antibodies and Hoechst (G-L). Higher magnification of outlined regions in G and H are shown in I,J and D,L, respectively. EC2-positive axons coalesce into small and well-defined glomeruli in *Kirrel3*$^{+/+}$*; EC2-lacZ* mice (yellow arrowheads, I, J) but innervate larger heterogenous glomeruli in *Kirrel3*$^{Q128A/Q128A}$ mice (yellow arrowheads in K, L). **M-P.** Quantification of the size and number of glomeruli in the anterior (G,I) and posterior regions (H,J) of the AOB in adult control and *Kirrel3*$^{Q128A/Q128A}$ mice. A representation of the glomeruli outlining approach used for quantification using sections in panels A and B as examples are shown in E and F, respectively. A significant increase in the size of glomeruli in the posterior (*Control:* 644.0 ± 56.2 μm^2; *Kirrel3*$^{Q128A/Q128A}$: 1134.1 ± 74.5 μm^2), but not anterior (*Control:* 284.0 ± 19.6 μm^2; *Kirrel3*$^{Q128A/Q128A}$: 295.6 ± 22.1 μm^2), region of the AOB is observed in the *Kirrel3*$^{Q128A/Q128A}$ mice (G,H). There is also a decrease in glomeruli numbers in the posterior (*Control:* 61.15 ± 1.75; *Kirrel3*$^{Q128A/Q128A}$: 34.27 ± 1.02), but not anterior (*Control:* 87.21 ± 4.92; *Kirrel3*$^{Q128A/Q128A}$: 84.22 ± 6.33), region of the AOB in *Kirrel3*$^{Q128A/Q128A}$ mice (J). Data were analyzed using unpaired *t*-test; *n*=8 mice for each genotype. *****p*-value < 0.0001 (glomerular counts), ****p*-value < 0.001 (glomerular size), error bars: ± SEM. Scale bars: 250 μm in A,B and 100 μm in C,D.

size and number of glomeruli in the anterior region of the AOB appears unaffected in *Kirrel3*$^{Q128A/Q128A}$ mice when compared to control animals (Figure 29A, B, G, I). In contrast, and as observed in *Kirrel3*$^{-/-}$ mice, the posterior region of the AOB in *Kirrel3*$^{Q128A/Q128A}$ mice contains significantly fewer glomeruli and the average size of each glomerulus in increased by ~43% (Figure 29A-C, H, J). Thus, the Kirrel3 D1-D1 binding interface is necessary for proper coalescence of VSN axons into glomeruli of the AOB.

4.3 DISCUSSION

The wiring of the nervous system is guided by a combination of intercellular interactions mediated by cell surface receptors (Sanes and Zipursky 2020). The interactions can be heterotypic, usually allowing for establishing connectivity between different neuronal types, guiding growth of axons in a gradient field established by cues or by contacts between processes resulting in attraction or repulsion. Homotypic interactions can also be used to establish synaptic connections (as Kirrel3 is known to mediate in the hippocampus), lead to contact-mediated repulsion or to fasciculation and coalesce axons. Kirrel2 and Kirrel3 are differentially expressed in sets of sensory neurons whose axons are segregated into separate glomeruli in the accessory and main olfactory bulbs. The molecular mechanism through which differential expression of Kirrel family members in populations of sensory axons modulates their segregation into glomeruli remained to be addressed.

Structures presented here show that Kirrel2 have key residues that allow the formation of a hydrogen bonding network at the homodimeric interface, while Kirrel3 evolved a hydrophobic interface in lieu of this hydrogen bonding network. Ancestral vertebrate Kirrel has crucial amino acids compatible with the presence of the hydrogen bonding network, and this specialization of a non-polar Kirrel3 interface core likely evolved to ensure exclusive homodimerization of the two Kirrels, and no heterodimerization, allowing for the segregation of OSN termini into separate Kirrel2 and Kirrel3-expressing glomeruli. This finding of incompatible interface chemistries is distinct to the vertebrate Kirrels: The two fruit fly Kirrel dimerization interfaces show strong conservation and compatible chemistries that would allow them to create putative complexes (Özkan et al. 2014), and there is evidence that fly Kirrels can form heterodimers (Özkan et al. 2013). We otherwise found that Kirrel duplications outside vertebrates is relatively rare.

The distribution of extant Kirrel proteins we identified in cyclostomes and gnathostomes are consistent with the duplication of Kirrels during the early chordate whole-genome duplication events (Dehal and Boore 2005). Given that ancestral Kirrel2 and Kirrel3 have chemically incompatible interface sequences similar to mouse Kirrels and that extant jawed fish Kirrel sequences also follow these patterns, Kirrel specialization must have appeared early in gnathostomes and before the rise of distinct accessory olfactory systems and several expansions in olfactory receptor gene families (Bear et al. 2016; Poncelet and Shimeld 2020). Therefore, it is attractive to speculate that specialization of Kirrels and other cell surface receptors differentially expressed in OSNs and VSNs and duplicated during the whole-genome duplication events, may have set the stage for increases in ORs, OSNs and glomeruli in main and accessory olfactory bulbs.

Kirrels have been identified and implicated in numerous functional contexts in the nervous system. Loss of Kirrel2 and Kirrel3 causes disorganization of a subset of glomeruli in the main and accessory olfactory bulbs (Brignall et al. 2018; Nakashima et al. 2019; Prince et al. 2013; Vaddadi et al. 2019), and Kirrel3 knockout mice show behavioral abnormalities similar to those in autistic patients, including defects in social responses, auditory sensory processing and communication, and repetitive behaviors (Hisaoka et al. 2018; Völker et al. 2018), in addition to loss of male-male aggression likely as a result of miswiring in the AOB (Prince et al. 2013). Furthermore, several mutations in human autism and intellectual disability patients were identified (see Taylor et al. 2020 for a list). To our surprise, none of the missense mutations are in the first domain, including mutations recently reported to affect Kirrel3-mediated cell adhesion (Taylor et al. 2020). We therefore studied the entire Kirrel2 and Kirrel3 ectodomains using a combination of biophysical methods but could not produce evidence that there are secondary binding sites outside the D1-D1 interface. A single alanine mutation at the D1-D1 Kirrel3 dimer interface completely abolishes ectodomain dimerization at micromolar concentrations. SAXS data suggest highly elongated models for dimerized Kirrels compatible with D1-D1 intermolecular interactions, further rendering other putative binding sites unlikely or very weak. Additional structural studies on liposomes and lipid bilayers may be necessary to refute or confirm secondary *cis* or *trans* binding sites.

We also showed that the dimerization interface observed in our structures directly contributes to glomerulus formation, at least in the case of Kirrel3. Morphological analysis of glomeruli in the AOB using the Kirrel3 Q128A substitution closely resembled those of the *Kirrel3* knockout, where glomeruli increase in size but decrease in number in the posterior AOB. We have confirmed that the Q128A mutant displays correctly to the cell surface, which implies that the observed AOB phenotype is not due to misfolding or trafficking errors. Though we did not test Kirrel2 loss-of-function mutations *in vivo*, Kirrel2 shares a closely related structure and evolutionary history with Kirrel3, and it is reasonable to assume that the dimerization interface on Kirrel2 D1 may also control glomerulus formation in a similar manner. However, while Kirrel homodimerization is necessary for proper glomerulus formation, it is likely that other molecules contribute to glomerular segregation of axons, including expression of vomeronasal receptors and other receptor pairs (such as Eph-Ephrin), and neuronal activity.

Multiple lines of evidence support the idea that Kirrels and its homologs act as more than “molecular Velcro” in nervous system development. In the hippocampus, Kirrel3 homophilic adhesion is required, but not sufficient for synapse formation, and mutations that occur outside of the D1 binding domains and even in the intracellular domains prevent synapse formation, despite being able to form homodimeric complexes (Taylor et al. 2020). The *C. elegans* homologs SYG-1 and SYG-2 were shown to be signaling receptors, whose functions depend on the exact geometry of ectodomain dimerization also mediated by D1 (Özkan et al. 2014). Finally, Kirrels carry conserved and functional signaling motifs in their cytoplasmic domain, including phosphorylation sites, PDZ motifs, and actin cytoskeleton recruitment sequences (Bulchand et al. 2010; Chia et al.

2014; Gerke et al. 2006; Harita et al. 2008; Huber et al. 2003; Sellin et al. 2003; Yesildag et al. 2015). These findings suggest that Kirrel3 undergoes active signaling once the homodimeric complexes have formed, which may be influenced by the overall flexibility and conformation of the extracellular domains and how tightly Kirrels may pack at the site of a Kirrel-mediated cell adhesion.

The question remains, however, of whether Kirrel2 and Kirrel3 also actively signal for the formation of glomeruli and may also regulate synapse formation of sensory neurons in these glomeruli with second-order neurons, such as mitral cells. As Kirrel3 has been shown to specify synapse formation in the hippocampus between dentate gyrus and CA1 neurons, it is possible that Kirrels play a dual role of simple adhesion and synapse specification. Some second-order neurons in the AOB were observed to selectively form dendrites to VSNs expressing the same vomeronasal receptors (Del Punta et al. 2002), indicating that synapses formed in the glomeruli may be specified by cell surface receptors controlled by vomeronasal receptor expression, such as Kirrels, to organize sensory input. A mechanism through which Kirrels mediate both VSN coalescence and synapse formation onto mitral cells would be appealing for its simplicity in explaining wiring specificity.

4.4 METHODS

4.4.1 Protein Expression and Purification

For biophysical and structural studies, mouse Kirrel2 and Kirrel3 constructs were expressed in High Five cells (*Trichoplusia ni*) using the baculovirus expression system. All expression constructs were tagged C-terminally with hexahistidine tags in the baculoviral transfer vector pAcGP67A (BD Biosciences). Proteins were purified using Ni-NTA agarose (Qiagen) resin first, followed by size-exclusion chromatography with Superdex 75 10/300 or Superdex 200 10/300

Increase columns (GE Healthcare) in 1x HBS (10 mM HEPES pH 7.2, 150 mM NaCl). We observed that some of the Kirrel constructs tend to precipitate at higher concentrations at 4°C; therefore, proteins were purified and stored only for short periods at 16 to 22°C.

4.4.2 Protein Crystallization

Purified mKirrel2 D1 was concentrated to 10.6 mg/ml and crystallized using the sitting-drop vapor-diffusion method in 0.4 M Potassium/Sodium tartrate. Crystals were cryo-protected in 0.5 M Sodium acetate, 30% Ethylene glycol, and vitrified in liquid nitrogen. Complete diffraction dataset was collected at the SSRL beamline 12-2.

Purified mKirrel3 D1 was concentrated to 9.1 mg/ml and crystallized using the sitting-drop vapor-diffusion method in 0.1 M Sodium cacodylate, pH 6.5, 1.4 M Sodium acetate. Crystals were cryo-protected in 0.1 M Sodium cacodylate, pH 6.5, 1.4 M Sodium acetate with 30% Ethylene glycol, and vitrified in liquid nitrogen. Complete diffraction dataset was collected at the APS beamline 24-ID-E.

4.4.3 Structure Determination by X-ray Crystallography

Diffraction data were reduced using *HKL2000* (Otwinowski and Minor 1997). Structure of mKirrel2 D1 was phased with molecular replacement using mouse Duf/Kirre D1 as model (PDB ID: 4OFI; Özkan et al. 2014) with *PHASER* (McCoy et al. 2007) as part of the *PHENIX* suite (Liebschner et al. 2019). For molecular replacement of the mKirrel3 D1 data set, a partly refined mKirrel2 D1 structure was used. Model building and refinement were done using *Coot* (Emsley et al. 2010, 2010) and *phenix.refine* (Afonine et al. 2012), respectively. mKirrel3 D1 model was refined with eight TLS groups, one for each chain in the asymmetric unit, while no TLS refinement was used for the mKirrel2 model. Crystal structures and structure factors are deposited with the Protein Data Bank with accession codes 7LTW (mKirrel2 D1) and 7LU6 (mKirrel3 D1).

4.4.4 Phylogenetics and Ancestral Sequence Reconstructions

Putative Kirrel orthologs were identified using a reciprocal *BLAST* strategy with the three mouse Kirrels, mouse Nephrin, and *D. melanogaster* Rst and Kirre. Each sequence hit was confirmed to contain conserved features of Kirrels and Nephrins, specifically five and ten IG/FnIIII domains, respectively, in the extracellular regions, and a membrane helix. A total of 90 Kirrel and 41 Nephrin-like proteins were identified across major protostome and deuterostome taxa; we failed to detect clear Kirrel and Nephrin orthologs in other metazoan groups.

The mature ectodomains of 90 Kirrel sequences were aligned using *MUSCLE* (version 3.8.425) with default parameters (Edgar 2004), as the other regions cannot be aligned with high confidence. Parts of the alignment with insertions represented by few sequences were removed, and maximum likelihood phylogenies were inferred using *RAxML-NG* v1.0.1 (Kozlov et al. 2019) using the best-fit LG+I+G4 evolutionary model determined by *MODELTEST-NG* (Darriba et al. 2020). Among the three vertebrate Kirrels, Kirrel2 shows faster and heterogenous rates of evolution in gnathostomes. Ancestral sequences were inferred using the marginal reconstruction algorithm in *PAML* v4.8 (Z. Yang 2007) using the LG+G4 model and the amino acid frequencies inferred on the ML tree by *RAxML* v8.2.12 (Stamatakis 2014).

Sequence logos are calculated in Geneious version 2020.2 (https://www.geneious.com). The list of species from which the sequences are collected are in the legend for Source Data 1.

4.4.5 Co-immunoprecipitation Assay

Baculoviruses expressing WT and mutant Kirrel3 ectodomains with C-terminal FLAG tags, and WT Kirrel2 and Kirrel3 ectodomains with a C-terminal hexahistidine-tag were used to infect High Five cells. 60-72 hrs post-infection, cultures were spun down, and conditioned media were collected. Hexahistidine-tagged Kirrel cultures were mixed with FLAG-tagged Kirrel cultures at

1:1 volume (total: 1000 μl) and incubated for 3 hours at room temperature with Anti-DYKDDDDK G1 affinity resin (GenScript) to capture WT and mutant Kirrel3-FLAG. Proteins captured on beads were washed twice in Tris-buffered saline (TBS, pH 7.6), eluted using 0.5 mg/ml FLAG peptide in TBS, and mixed with 6x SDS sample loading buffer. Following SDS-PAGE gel electrophoresis, samples were blotted onto Sequi-Blot PVDF membranes (Bio-Rad), and co-immunoprecipitated Kirrel2-His$_6$ was detected using anti-His antibodies conjugated to iFluor 488 (GenScript). Anti-DYKDDDDK antibodies conjugated to iFluor 488 (GenScript) were also used to detect and confirm expression of FLAG-tagged Kirrel3 constructs captured on resin.

4.4.6 Analytical Ultracentrifugation

Analytical ultracentrifugation data was collected at the UT Southwestern Macromolecular Biophysics Resource laboratory. mKirrel2 and mKirrel3 ectodomain samples were placed in 0.3 or 1.2-cm charcoal-filled Epon centerpieces sandwiched between sapphire windows. Cells were placed in an An50-Ti rotor and spun at 20°C at 50,000 rpm for sedimentation velocity experiments. During the spins, concentration profiles were measured using absorbance at 230 nm or using Rayleigh interferometry for the highest concentration samples. The data were analyzed using the *c*(*s*) methodology in *SEDFIT* (P. Schuck 2000). Partial-specific volume, density, and viscosity were calculated using *SEDNTERP* (Laue et al. 1992), and the following values were used in data analysis: ε_{230} = 389,836 (mKirrel2) and 395,466 (mKirrel3) $M^{-1}cm^{-1}$; $\varepsilon_{\text{interferometric}}$ = 150,896 (mKirrel2) and 151,329 (mKirrel3) $M^{-1}cm^{-1}$; ρ(solution) = 1.0052 g/cm3; η(solution) = 0.010249 Poise.

To calculate dissociation constants, *GUSSI* (Brautigam 2015) was used to integrate the *c*(*s*) distributions, which were assembled into isotherm files that were imported into *SEDPHAT*, where a monomer-dimer model was imposed (Peter Schuck 2003) with a fixed *s*-value for the monomer (2.87 S). All AUC figures were rendered in *GUSSI*.

The Q128A mutant for the mKirrel3 ectodomain displayed an unmoving peak at all concentrations with a calculated sedimentation coefficient of 2.87 S, which represents the monomer, while the WT mKirrel2 and mKirrel3 ectodomains had c(s) distributions showing increasing sedimentation coefficients with increasing protein concentrations, where dimeric mKIrrel2 and mKirrel3 have refined sedimentation coefficients of 3.9 and 3.8 S, respectively. The single peaks observed in the *S* vs. $c(s)$ plots, in addition to size-exclusion chromatography elution profiles showing single peaks corresponding to intermediate hydrodynamic sizes, strongly suggest fast rates of dimerization kinetics ($k_{\text{off}} > 10^{-3}\ \text{s}^{-1}$)

4.4.7 Cell Aggregation Assays

Kirrel ectodomains were cloned in the Drosophila expression plasmid pAWG (Drosophila Genomics Resource Center), and transiently transfected in S2 cells using Effectene (QIAGEN, catalog no. 301425). Cells were collected three days post-transfection, spun down at 250 x g for 5 minutes, washed once with phosphate-buffered saline, and re-suspended in serum-free Schneider's media (Lonza, catalog no. 04-351Q) at 10^7/ml cell density before imaging.

4.4.8 SEC-SAXS-MALS

Scattering data was collected for Kirrel ectodomains at the Advanced Photon Source beamline 18-ID using a SEC-SAXS-MALS setup. *BioXTAS RAW* version 2.0.2 was used for SAXS data collection and data reduction (Hopkins, Gillilan, and Skou 2017). The *RAW* interface was also used for Guinier analysis of the scattering data and the indirect Fourier transform methods implemented in *GNOM* (Svergun 1992), part of the *ATSAS* package (Manalastas-Cantos et al. 2021), for pair-distance distribution analysis. Domains 2 to 5 for mKirrel3 were modeled using the

I-TASSER server (Roy, Kucukural, and Zhang 2010; J. Yang and Zhang 2015). Modeling using the SAXS data was performed using the *ATSAS* package version 3.0.3 with the *ab initio* shape determination by bead modeling in *DAMMIF (Franke and Svergun 2009)*, with the ensemble optimization method implemented in *EOM* (Tria et al. 2015), and with the simulated annealing protocol for connected domains in *SASREF* (Petoukhov and Svergun 2005).

Light scattering data was collected at the APS 18-ID beamline on a DAWN HELEOS with a T-rEX refractometer (Wyatt Technology) at 25°C, and analyzed in *ASTRA* version 7.3.2.19. *dn*/*dc* values of 0.181 to 0.182 were used to account for predicted glycosylation for molar mass calculations. Further details about MALS data collection and analysis are tabulated in Table 4. Expected molecular masses for Kirrel2 and Kirrel3 WT ectodomain constructs without glycosylation are both 53.0 kDa. With predicted N-linked glycosylation added by the insect cell expression system, we expect molecular masses for Kirrel2 and Kirrel3 WT ectodomain monomers to be 56 to 59 kDa.

4.4.9 Flow Cytometry Assay for Cell Surface Trafficking

Kirrel3 WT and Q128A cDNA, excluding the signal peptide, were cloned C-terminal to a preprotrypsin leader sequence and a FLAG peptide (DYKDDDDK) under the control of the CMV promoter, and transfected into HEK293T cells using LipoD293 (SignaGen Laboratories, catalog no. SL100668). After 48 h, transfected cells were detached from the cell culture plate by incubating cells in a citric saline solution (135 mM potassium chloride, 50 mM sodium citrate) at 37°C for 5 min, followed by addition of Dulbecco's modified Eagle medium (Thermo Fisher, catalog no. 11965092) with 10% fetal bovine serum and mechanical suspension of cells. Cells were spun down at 500 *g* for 5 min washed with phosphate-buffered saline (PBS; Thermo Fisher, catalog no. BP661-50, 137 mM NaCl, 2.7 mM KCl, 11.9 mM phosphate, pH 7.4), then resuspended in PBS +

0.1% bovine serum albumin (BSA). For staining of Kirrel3 displayed on the cell surface, cells were incubated with anti-FLAG M2 antibody (Sigma, catalog no. F3165; 1:1000 dilution in PBS with 0.1% BSA) for 30 min at room temperature, washed twice with PBS + 0.1% BSA, then incubated with a secondary donkey anti-mouse Alexa Fluor 488 antibody (Thermo Fisher, catalog no. A-21202; 1:500 dilution in PBS with 0.1% BSA). In preparation for flow cytometry, cells were washed twice and resuspended in PBS + 0.1% BSA. Surface display of the Kirrel3 ectodomains on HEK cells were measured on the Accuri C6 flow cytometer (BD Biosciences) with the 488 nm excitation laser and the 533 nm filter in 10,000 cells per sample.

4.4.10 Animals

The *Kirrel3 Q128A* mouse line was generated as follows: sgRNAs were designed using the open access software Breaking-Cas (https://bioinfogp.cnb.csic.es/tools/breakingcas) (Oliveros et al. 2016) and tested for cutting efficiency using a T7 assay as previously described (Sakurai et al. 2014). One-cell stage C57Bl6 mouse zygotes were microinjected with the sgRNA, Cas9 protein, and a donor DNA template to introduce the required DNA mutations in the *Kirrel3* allele (see Figure 28A) and were implanted in surrogate female mice. Offsprings were screened for the presence of the target mutations by PCR, restriction enzyme analysis, and DNA sequencing. Three *Kirrel3 Q128A* founder lines were chosen for further analyses and backcrossed for three generations in the C57Bl6 background to segregate any potential off-target mutations. Analyses of the glomerular structure of the AOB presented in Figure 29 was performed on *Kirrel3 Q128A* mice derived from a single founder line. Similar analyses were also performed on *Kirrel3 Q128A* mice derived from two other founder lines and revealed similar phenotypes (data not shown). The *EC2-tau-lacZ* (Tg(Vmn2r43-lacZ*)#Ddg) mouse line has previously been described (Cloutier et al. 2004). All animal procedures have been approved by The Neuro Animal Care Committee and McGill University, in accordance with guidelines of Canadian Council of Animal Care.

4.4.11 Immunohistochemistry

Two to three-month-old adult mice were anesthetized and perfused transcardially with 10 ml ice-cold 1x PBS followed by 10 ml 4% paraformaldehyde solution in 1x PBS. Brains were dissected and post-fixed in 4% paraformaldehyde solution for 30 min followed by 24 h cryoprotection in 30% sucrose. 20 μm-thick sagittal AOB sections were collected on microscope slides and incubated overnight at 4°C with the following primary antibodies: Anti-VGLUT2, 1:500 (Synaptic Systems) or anti-Kirrel3, 1:100 (Neuromab). After rinsing in Tris-Buffered Saline, the appropriate secondary antibody-Alexa 488 conjugate (Molecular Laboratories) was applied at 1:500 dilution to detect the primary antibody and BS lectin at 1:1500 (Vector Laboratories) was applied along with the secondary antibody. Sections were counter-stained with Hoechst at 1:20,000 dilution (Thermo Fisher Scientific).

4.4.12 Analysis of Glomeruli in the AOB

Analysis of the size and number of glomeruli in AOB sections were performed as previously described (Brignall et al. 2018; Prince et al. 2013). 20 μm-thick sagittal sections of the AOB were obtained from *Kirrel3*$^{+/+}$, *Kirrel3* $^{+/Q128A}$, and *Kirrel3* $^{Q128A/Q128A}$ mouse brains. A blinded analysis measuring glomerular size and number using Fiji software (Schindelin et al. 2012) was performed on 8 to 10 consecutive sections from both AOBs that contained anterior and posterior regions of similar sizes at comparable medial-lateral level. Each VGLUT2 positive unit surrounded by a region of non-innervated neuropil was defined as a glomerulus and was manually traced on Fiji by an expert. The number of glomeruli and their sizes was measured from each section examined and the average values for each mouse brain was calculated. Since no difference was observed between

Kirrel3$^{+/+}$ and *Kirrel3* $^{+/Q128A}$ mice, they were grouped together and designated as Controls. The anterior-posterior AOB border was identified by staining sections with BS lectin (data not shown). Littermates were used for analyses.

4.4.13 Analysis of Kirrel3 protein expression

Whole brain lysates were harvested using 20 mM HEPES, 320 mM sucrose with protease inhibitors (0.1 μg/μl Leupeptin/Aprotinin and 1 mM PMSF). Protein concentration of lysate was determined using the Bio-Rad protein concentration assay and equal amounts of protein were loaded and subjected to SDS-PAGE gel electrophoresis followed by transfer to PVDF membranes (Immobilon-P). Membranes were probed with mouse anti-Kirrel3 1:100 (Neuromab Clone N321C/49; catalog no. 75-333) that detects the long and short isoforms of Kirrel3, rat anti-HSC70/HSP73 1:10,000 (Enzo Life Sciences), or rabbit anti-β-actin 1:1,000 (Cell Signalling Technology), followed with appropriate HRP-conjugated secondary antibodies. Blots were developed using SuperSignal West Femto Kit (Thermo Fisher Scientific). Quantification of relative protein levels was performed on scanned immunoblots using Fiji software.

4.4.14 Cell surface biotinylation in acute brain slices

Cell surface biotinylation assay was performed as described (Gabriel, Wu, and Melikian 2014). Acute mouse brain slices were prepared from *Kirrel3*$^{Q128A/Q128A}$ and *Kirrel3*$^{+/+}$ mice, placed in ACSF and allowed to recover in a recovery chamber for 1 hour at room temperature. Two slices were incubated in in chilled ACSF containing 1 mg/ml EZ-link Sulfo-NHS-SS-Biotin (Thermo Fisher Scientific) for 45 minutes. The biotin was then quenched with two washes of 10 mM Glycine in ACSF at 4°C followed by three washes in ice cold ACSF for 5 min. Slices were then harvested in RIPA buffer (10 mM Tris pH 7.45, 150 mM NaCl, 1 mM EDTA, 1% Triton X-100, 0.1% SDS and 1% sodium deoxycholate) supplemented with protease and phosphatase inhibitors

(100 mM PMSF and PhosSTOP tablet (Roche)). Biotinylated proteins were precipitated with streptavidin-agarose beads (Thermo Fisher Scientific) at 4°C overnight, washed, and eluted from beads using SDS-PAGE reducing sample buffer. Equal amounts of protein were then subjected to a Western Blot analysis as described above.

CHAPTER 5: DISCUSSION

CELL SIGNALING AND NERVOUS SYSTEM WIRING

Communication between a developing neuron and its extracellular space plays a key role in directing neural circuit assembly. In this dissertation, we have explored three systems of dendritic and axonal guidance, each demonstrating a different logic of molecular interactions uniquely suited for their roles. The development of entire nervous systems depends on the combination of such varied and specialized molecular recognition systems to regulate the assembly of diverse neuronal circuits. Our findings not only reveal how the structural properties of these proteins contribute to the mechanisms of receptor signaling and neurite guidance, but also open questions about the evolutionary origins of nervous system complexity and how small changes in structural properties can contribute to divergence in function.

The quaternary complex of MNR-1, SAX-7, LECT-2, and DMA-1 represents an elegant solution to the growth patterning of the PVD dendrite arbors. DMA-1 is activated by simultaneous interaction with 3 ligands; absence of even a single ligand prevents development of the full arbor to the quaternary branches (Dong et al. 2013; Zou et al. 2016). All-or-nothing receptor activation by a ternary "key" has not been identified in any other system and may be an adaptation to direct the growth of a simple and highly stereotyped nervous system, without flexibility or plasticity. The cues in this case act less like a "guide" to indicate direction of growth and more as a map of allowed and disallowed spaces as the dendrite extends, outlining the full extent of the possible dendrite arbor. Alternatively, this form of arbor mapping may represent a dendrite-specific strategy for arborization, as dendrites branch extensively compared to axons and must evenly sample a large receptive field instead of innervating a few target neurons (Jan and Jan 2010b).

In contrast, mammalian Robo3 is a single receptor among three tightly coordinated receptor-ligand pairs that mediate midline crossing in spinal cord commissures. In this system, proper axonal navigation is dependent on the timing of receptor activation, rather than the overlap of multiple cues(Z. Chen et al. 2008, 3; Zelina, Blockus, Zagar, Péres, Friocourt, Wu, Rama, Fouquet, Hohenester, Tessier-Lavigne, Schweitzer, Crollius, et al. 2014, 3). The ability of Robo3 to perform NELL2-mediated axon repulsion in addition to its regulatory role modulates midline crossing by adding an additional cue that guides commissural axon navigation. Modulation by the addition of multiple cues or adjusting the responses of existing ones appears to give this system flexibility to adapt to the context of each particular nervous system, while also ensuring the key navigational challenge of crossing the midline and preventing re-crossing.

Kirrel2 and Kirrel3 operate in the simplest manner, mediating axon guidance through formation of *trans*-homodimeric pairs, but act in conjunction with other attractive and repulsive cues present on the same axonal surface to create at least 1,100 glomeruli of unique molecular identity in the olfactory bulb (Zapiec and Mombaerts 2015). EphA and Ephrin-A, for example, mediate contact-mediated repulsion in a converse manner to Kirrel2 and Kirrel3's homophilic adhesion (Serizawa et al. 2006). The independent action of multiple different combinations of such cell-surface receptors, as well as longer-range guidance cues, expands the possible number of distinct molecular identities of glomeruli and ensures the coalescence of OSNs expressing the same ORs into homogenous glomeruli. The expression of these cues is regulated by the activity of the OR of each OSN—which is stochastically determined—and enables newly differentiated neurons to integrate into existing olfactory circuits well into adulthood.

SIGNAL TRANSDUCTION AND CYTOSKELETAL REMODELING

Guidance cues generally direct the growth of developing axons and dendrites through modulation of the cytoskeleton. Though the exact details of DMA-1 activation are unknown, its intracellular PDZ domains forms complexes with the claudin-like protein, HPO-30, which localizes DMA-1 to the dendritic surface (Zou et al. 2016), as well as with the guanine nucleotide exchange factor, Tiam-1, with which it modulates F-actin localization and polymerization (Tang et al. 2019). These complexes also activate actin polymerization through the WAVE regulatory complex (Shi et al. 2021). Robo family proteins may signal through WAVE as well as WASP complexes indirectly through interactions with srGAP (Blockus and Chédotal 2016b; Iversen et al. 2020). Robo3 activation by NELL2 has been demonstrated to downregulate cdc42 through srGAP, inhibiting actin polymerization (Jayabal et al. 2021). Activation of these pathways may be dependent on the formation of rigid cell-surface clusters by NELL2-Robo3 complexes.

Phase separation of these proteins is a potential mechanism used to recruit additional Robo3 receptors or to maintain a high local concentration in order to stimulate downstream recruitment of signaling molecules (Case, Ditlev, and Rosen 2019). While Robo3 is capable of forming condensates and punctate cell-surface clusters without NELL2, addition of NELL2 alters condensate properties to be more rigid and initiates cluster formation at lower concentrations than Robo3 alone. Phase separation may also play a role in Kirrel2 and Kirrel3 signaling through the co-factor Nephrin1. Kirrel1 complexes with Nephrin1, whose phosphorylated cytoplasmic tails are capable of initiating spontaneous actin polymerization through formation of condensates with Nck and N-WASP (Garg et al. 2007; Li et al. 2012; Banjade and Rosen 2014). As Nephrin1 is also expressed in the olfactory system, Kirrel2 and Kirrel3 may utilize the same signaling pathways to stimulate actin polymerization and stabilize the growth cone upon homodimerization (Putaala 2001).

EVOLUTION OF PROTEINS AND NERVOUS SYSTEM EXPANSION

The Robo and Kirrel protein families also represent two avenues of study to compare the evolution of protein function in context of the nervous system. While Robo1 and Robo2 have redundant roles in spinal cord development and axon repulsion, mammalian Robo3 displays obvious divergent functions, such as loss of binding to Slit and development of DCC potentiation (Beamish and Kennedy 2015). As there is a lack of research on the role of Robo3 in non-mammalian vertebrate nervous system development, how Robo3 functions in nervous system development outside of mammals is unknown. Loss of Slit binding in mammalian Robo3 may have accompanied development of DCC potentiation, in order to prevent counterproductive repulsive signaling. In the case of non-mammalian vertebrates, Robo3 potentiation of DCC has not been observed, which may be a reason why Slit binding is retained in these lineages (Beamish and Kennedy 2015, 3). However, Robo3 expression is conserved in the developing CNS among amniotes, including a rapid downregulation of expression in most commissural neurons after midline crossing, indicating that it still plays a major role in coordinating commissural axon crossing even outside of mammals, perhaps through regulation of Robo1/2 (Friocourt et al. 2019). Robo3's functions appear to aid development in the context of larger and more complex systems and may have found distinct strategies to do so among different vertebrate clades. Its additional role in mammals as a NELL2 receptor further increases the modulatory signals allowing for precise control of commissural neuron migration and further investigation into NELL2-Robo3 signaling in non-mammalian species will reveal whether this is a common strategy among chordates.

In comparison, Kirrel2 and Kirrel3 show much smaller differences in function, both undergoing homophilic adhesion and playing similar roles in directing axon targeting and coalescence. However, a small number of mutations early in Kirrel3 evolution contributed to a major shift from homodimerization mediated through hydrophilic residues to hydrophobic interactions, precluding heterodimerization between Kirrel2 and Kirrel3. In the olfactory system, this has led to a nearly two-fold increase in the number of possible unique glomeruli of axons from OSNs expressing the same OR, allowing for a greater ability to recognize chemical stimuli for more complex behavioral patterns (Brignall et al. 2018; Prince et al. 2013).

CONCLUSION

At its most basic, assembly of neural circuits depends on the regulation of attractive and repulsive cues. However, as organisms have evolved, the sum of guidance cues required for the development of complex nervous systems has multiplied, requiring finely tuned interactions between different cues for specialized systems. By determining the precise molecular interactions between these guidance cues and receptors and understanding their signaling mechanisms, we can understand how the most minute changes can contribute to observable changes in morphology and behavior.

BIBLIOGRAPHY

Afonine, Pavel V, Ralf W Grosse-Kunstleve, Nathaniel Echols, Jeffrey J Headd, Nigel W Moriarty, Marat Mustyakimov, Thomas C Terwilliger, Alexandre Urzhumtsev, Peter H Zwart, and Paul D Adams. 2012. "Towards Automated Crystallographic Structure Refinement with Phenix.Refine." *Acta Crystallographica. Section D, Biological Crystallography* 68 (Pt 4): 352–67. https://doi.org/10.1107/S0907444912001308.

Aleksandrova, Nataliia, Irina Gutsche, Eaazhisai Kandiah, Sergiy V. Avilov, Maxim V. Petoukhov, Elena Seiradake, and Andrew A. McCarthy. 2018. "Robo1 Forms a Compact Dimer-of-Dimers Assembly." *Structure (London, England: 1993)* 26 (2): 320-328.e4. https://doi.org/10.1016/j.str.2017.12.003.

Alfaro, Joshua F., Cheng-Xin Gong, Matthew E. Monroe, Joshua T. Aldrich, Therese R. W. Clauss, Samuel O. Purvine, Zihao Wang, et al. 2012. "Tandem Mass Spectrometry Identifies Many Mouse Brain O-GlcNAcylated Proteins Including EGF Domain-Specific O-GlcNAc Transferase Targets." *Proceedings of the National Academy of Sciences of the United States of America* 109 (19): 7280–85. https://doi.org/10.1073/pnas.1200425109.

Banjade, Sudeep, and Michael K Rosen. 2014. "Phase Transitions of Multivalent Proteins Can Promote Clustering of Membrane Receptors." *ELife* 3 (October): e04123. https://doi.org/10.7554/eLife.04123.

Barak, Reut, Galit Yom-Tov, Julia Guez-Haddad, Lital Gasri-Plotnitsky, Roy Maimon, Moran Cohen-Berkman, Andrew A. McCarthy, et al. 2019. "Structural Principles in Robo Activation and Auto-Inhibition." *Cell* 177 (2): 272-285.e16. https://doi.org/10/gfwk5b.

Beamish, Ian V., and Timothy E. Kennedy. 2015. "Robo3: The Road Taken." *Developmental Cell* 32 (1): 3–4. https://doi.org/10.1016/j.devcel.2014.12.021.

Bear, Daniel M., Jean-Marc Lassance, Hopi E. Hoekstra, and Sandeep Robert Datta. 2016. "The Evolving Neural and Genetic Architecture of Vertebrate Olfaction." *Current Biology: CB* 26 (20): R1039–49. https://doi.org/10.1016/j.cub.2016.09.011.

Belluscio, L., G. Koentges, R. Axel, and C. Dulac. 1999. "A Map of Pheromone Receptor Activation in the Mammalian Brain." *Cell* 97 (2): 209–20. https://doi.org/10.1016/s0092-8674(00)80731-x.

Bhalla, Kavita, Yue Luo, Tim Buchan, Michael A. Beachem, Gregory F. Guzauskas, Sydney Ladd, Shelly J. Bratcher, et al. 2008. "Alterations in CDH15 and KIRREL3 in Patients with Mild to Severe Intellectual Disability." *American Journal of Human Genetics* 83 (6): 703–13. https://doi.org/10.1016/j.ajhg.2008.10.020.

Blockus, Heike, and Alain Chédotal. 2016a. "Slit-Robo Signaling." *Development (Cambridge, England)* 143 (17): 3037–44. https://doi.org/10.1242/dev.132829.

———. 2016b. “Slit-Robo Signaling.” *Development* 143 (17): 3037–44. https://doi.org/10.1242/dev.132829.

Boyer, Nicholas P., and Stephanie L. Gupton. 2018. “Revisiting Netrin-1: One Who Guides (Axons).” *Frontiers in Cellular Neuroscience* 12: 221. https://doi.org/10.3389/fncel.2018.00221.

Brautigam, Chad A. 2015. “Calculations and Publication-Quality Illustrations for Analytical Ultracentrifugation Data.” *Methods in Enzymology* 562: 109–33. https://doi.org/10.1016/bs.mie.2015.05.001.

Brignall, Alexandra C., and Jean-François Cloutier. 2015. “Neural Map Formation and Sensory Coding in the Vomeronasal System.” *Cellular and Molecular Life Sciences: CMLS* 72 (24): 4697–4709. https://doi.org/10.1007/s00018-015-2029-5.

Brignall, Alexandra C., Reesha Raja, Alina Phen, Janet E. A. Prince, Emilie Dumontier, and Jean-François Cloutier. 2018. “Loss of Kirrel Family Members Alters Glomerular Structure and Synapse Numbers in the Accessory Olfactory Bulb.” *Brain Structure & Function* 223 (1): 307–19. https://doi.org/10.1007/s00429-017-1485-0.

Brose, K., K. S. Bland, K. H. Wang, D. Arnott, W. Henzel, C. S. Goodman, M. Tessier-Lavigne, and T. Kidd. 1999. “Slit Proteins Bind Robo Receptors and Have an Evolutionarily Conserved Role in Repulsive Axon Guidance.” *Cell* 96 (6): 795–806.

Bulchand, Sarada, Sree Devi Menon, Simi Elizabeth George, and William Chia. 2010. “The Intracellular Domain of Dumbfounded Affects Myoblast Fusion Efficiency and Interacts with Rolling Pebbles and Loner.” *PloS One* 5 (2): e9374. https://doi.org/10.1371/journal.pone.0009374.

Camurri, Laura, Elvira Mambetisaeva, Derek Davies, John Parnavelas, Vasi Sundaresan, and William Andrews. 2005. “Evidence for the Existence of Two Robo3 Isoforms with Divergent Biochemical Properties.” *Molecular and Cellular Neurosciences* 30 (4): 485–93. https://doi.org/10.1016/j.mcn.2005.07.014.

Case, Lindsay B., Jonathon A. Ditlev, and Michael K. Rosen. 2019. “Regulation of Transmembrane Signaling by Phase Separation.” *Annual Review of Biophysics* 48 (1): 465–94. https://doi.org/10.1146/annurev-biophys-052118-115534.

Chen, Jianling, Shunying Yu, Yingmei Fu, and Xiaohong Li. 2014. “Synaptic Proteins and Receptors Defects in Autism Spectrum Disorders.” *Frontiers in Cellular Neuroscience* 8: 276. https://doi.org/10.3389/fncel.2014.00276.

Chen, Vincent B, W Bryan Arendall 3rd, Jeffrey J Headd, Daniel A Keedy, Robert M Immormino, Gary J Kapral, Laura W Murray, Jane S Richardson, and David C Richardson. 2010. “MolProbity: All-Atom Structure Validation for Macromolecular

Crystallography." *Acta Crystallographica. Section D, Biological Crystallography* 66 (Pt 1): 12–21. https://doi.org/10.1107/S0907444909042073.

Chen, Zhe, Bryan B. Gore, Hua Long, Le Ma, and Marc Tessier-Lavigne. 2008. "Alternative Splicing of the Robo3 Axon Guidance Receptor Governs the Midline Switch from Attraction to Repulsion." *Neuron* 58 (3): 325–32. https://doi.org/10.1016/j.neuron.2008.02.016.

Cheng, Shouqiang, James Ashley, Justyna D. Kurleto, Meike Lobb-Rabe, Yeonhee Jenny Park, Robert A. Carrillo, and Engin Özkan. 2019. "Molecular Basis of Synaptic Specificity by Immunoglobulin Superfamily Receptors in Drosophila." *ELife* 8 (January): e41028. https://doi.org/10.7554/eLife.41028.

Cheng, Shouqiang, Yeonwoo Park, Justyna D. Kurleto, Mili Jeon, Kai Zinn, Joseph W. Thornton, and Engin Özkan. 2019. "Family of Neural Wiring Receptors in Bilaterians Defined by Phylogenetic, Biochemical, and Structural Evidence." *Proceedings of the National Academy of Sciences of the United States of America* 116 (20): 9837–42. https://doi.org/10.1073/pnas.1818631116.

Chia, Poh Hui, Baoyu Chen, Pengpeng Li, Michael K Rosen, and Kang Shen. 2014. "Local F-Actin Network Links Synapse Formation and Axon Branching." *Cell* 156 (1–2): 208–20. https://doi.org/10.1016/j.cell.2013.12.009.

Chisholm, A., and M. Tessier-Lavigne. 1999. "Conservation and Divergence of Axon Guidance Mechanisms." *Current Opinion in Neurobiology* 9 (5): 603–15. https://doi.org/10.1016/S0959-4388(99)00021-5.

Cloutier, Jean-François, Amar Sahay, Ernie C. Chang, Marc Tessier-Lavigne, Catherine Dulac, Alex L. Kolodkin, and David D. Ginty. 2004. "Differential Requirements for Semaphorin 3F and Slit-1 in Axonal Targeting, Fasciculation, and Segregation of Olfactory Sensory Neuron Projections." *The Journal of Neuroscience: The Official Journal of the Society for Neuroscience* 24 (41): 9087–96. https://doi.org/10.1523/JNEUROSCI.2786-04.2004.

Cronin, Ciarán N, Kheng B Lim, and Joe Rogers. 2007. "Production of Selenomethionyl-Derivatized Proteins in Baculovirus-Infected Insect Cells." *Protein Science: A Publication of the Protein Society* 16 (9): 2023–29. https://doi.org/10.1110/ps.072931407.

Darriba, Diego, David Posada, Alexey M. Kozlov, Alexandros Stamatakis, Benoit Morel, and Tomas Flouri. 2020. "ModelTest-NG: A New and Scalable Tool for the Selection of DNA and Protein Evolutionary Models." *Molecular Biology and Evolution* 37 (1): 291–94. https://doi.org/10.1093/molbev/msz189.

De Rubeis, Silvia, Xin He, Arthur P. Goldberg, Christopher S. Poultney, Kaitlin Samocha, A. Erucment Cicek, Yan Kou, et al. 2014. "Synaptic, Transcriptional and Chromatin Genes Disrupted in Autism." *Nature* 515 (7526): 209–15. https://doi.org/10.1038/nature13772.

Dehal, Paramvir, and Jeffrey L. Boore. 2005. "Two Rounds of Whole Genome Duplication in the Ancestral Vertebrate." *PLoS Biology* 3 (10): e314. https://doi.org/10.1371/journal.pbio.0030314.

Del Punta, Karina, Adam Puche, Niels C. Adams, Ivan Rodriguez, and Peter Mombaerts. 2002. "A Divergent Pattern of Sensory Axonal Projections Is Rendered Convergent by Second-Order Neurons in the Accessory Olfactory Bulb." *Neuron* 35 (6): 1057–66. https://doi.org/10.1016/s0896-6273(02)00904-2.

Desai, Jayashree, Mark E. Shannon, Mahlon D. Johnson, David W. Ruff, Lori A. Hughes, Marilyn K. Kerley, Donald A. Carpenter, Dabney K. Johnson, Eugene M. Rinchik, and Cymbeline T. Culiat. 2006. "Nell1-Deficient Mice Have Reduced Expression of Extracellular Matrix Proteins Causing Cranial and Vertebral Defects." *Human Molecular Genetics* 15 (April): 1329–41. https://doi.org/10.1093/hmg/ddl053.

Díaz-Balzac, Carlos A., Maisha Rahman, María I. Lázaro-Peña, Lourdes A. Martin Hernandez, Yehuda Salzberg, Cristina Aguirre-Chen, Zaven Kaprielian, and Hannes E. Bülow. 2016. "Muscle- and Skin-Derived Cues Jointly Orchestrate Patterning of Somatosensory Dendrites." *Current Biology* 26 (17): 2397. https://doi.org/10.1016/j.cub.2016.07.078.

Dickson, Barry J., and Giorgio F. Gilestro. 2006. "Regulation of Commissural Axon Pathfinding by Slit and Its Robo Receptors." *Annual Review of Cell and Developmental Biology* 22: 651–75. https://doi.org/10.1146/annurev.cellbio.21.090704.151234.

Dong, Xintong, Hui Chiu, Yeonhee Jenny Park, Wei Zou, Yan Zou, Engin Özkan, Chieh Chang, and Kang Shen. 2016. "Precise Regulation of the Guidance Receptor DMA-1 by KPC-1/Furin Instructs Dendritic Branching Decisions." *ELife* 5 (March): e11008. https://doi.org/10.7554/eLife.11008.

Dong, Xintong, Oliver W. Liu, Audrey S. Howell, and Kang Shen. 2013. "An Extracellular Adhesion Molecule Complex Patterns Dendritic Branching and Morphogenesis." *Cell* 155 (2): 296–307. https://doi.org/10.1016/j.cell.2013.08.059.

Donoviel, D. B., D. D. Freed, H. Vogel, D. G. Potter, E. Hawkins, J. P. Barrish, B. N. Mathur, et al. 2001. "Proteinuria and Perinatal Lethality in Mice Lacking NEPH1, a Novel Protein with Homology to NEPHRIN." *Molecular and Cellular Biology* 21 (14): 4829–36. https://doi.org/10.1128/MCB.21.14.4829-4836.2001.

Dulac, Catherine, and A. Thomas Torello. 2003. "Molecular Detection of Pheromone Signals in Mammals: From Genes to Behaviour." *Nature Reviews. Neuroscience* 4 (7): 551–62. https://doi.org/10.1038/nrn1140.

Edgar, Robert C. 2004. "MUSCLE: Multiple Sequence Alignment with High Accuracy and High Throughput." *Nucleic Acids Research* 32 (5): 1792–97. https://doi.org/10.1093/nar/gkh340.

Emsley, P, B Lohkamp, W G Scott, and K Cowtan. 2010. “Features and Development of Coot.” *Acta Crystallographica. Section D, Biological Crystallography* 66 (Pt 4): 486–501. https://doi.org/10.1107/S0907444910007493.

Evans, Timothy A., Celine Santiago, Elise Arbeille, and Greg J. Bashaw. 2015. “Robo2 Acts in Trans to Inhibit Slit-Robo1 Repulsion in Pre-Crossing Commissural Axons.” *ELife* 4: e08407. https://doi.org/10.7554/eLife.08407.

Finci, Lorenzo I., Nina Krüger, Xiaqin Sun, Jie Zhang, Magda Chegkazi, Yu Wu, Gundolf Schenk, et al. 2014. “The Crystal Structure of Netrin-1 in Complex with DCC Reveals the Bifunctionality of Netrin-1 as a Guidance Cue.” *Neuron* 83 (4): 839–49. https://doi.org/10.1016/j.neuron.2014.07.010.

Franke, Daniel, and Dmitri I. Svergun. 2009. “DAMMIF, a Program for Rapid Ab-Initio Shape Determination in Small-Angle Scattering.” *Journal of Applied Crystallography* 42 (Pt 2): 342–46. https://doi.org/10.1107/S0021889809000338.

Friocourt, François, and Alain Chédotal. 2017. “The Robo3 Receptor, a Key Player in the Development, Evolution, and Function of Commissural Systems: Function and Dysfunction of Robo3.” *Developmental Neurobiology* 77 (7): 876–90. https://doi.org/10.1002/dneu.22478.

Friocourt, François, Peter Kozulin, Morgane Belle, Rodrigo Suárez, Nicolas Di-Poï, Linda J. Richards, Paolo Giacobini, and Alain Chédotal. 2019. “Shared and Differential Features of Robo3 Expression Pattern in Amniotes.” *Journal of Comparative Neurology* 527 (12): 2009–29. https://doi.org/10.1002/cne.24648.

Fukuhara, Noémi, Jason A. Howitt, Sadaf-Ahmahni Hussain, and Erhard Hohenester. 2008. “Structural and Functional Analysis of Slit and Heparin Binding to Immunoglobulin-like Domains 1 and 2 of Drosophila Robo.” *The Journal of Biological Chemistry* 283 (23): 16226–34. https://doi.org/10/bp62x7.

Gabriel, Luke R., Sijia Wu, and Haley E. Melikian. 2014. “Brain Slice Biotinylation: An Ex Vivo Approach to Measure Region-Specific Plasma Membrane Protein Trafficking in Adult Neurons.” *Journal of Visualized Experiments: JoVE*, no. 86 (April): e51240. https://doi.org/10.3791/51240.

Garg, Puneet, Rakesh Verma, Deepak Nihalani, Duncan B. Johnstone, and Lawrence B. Holzman. 2007. “Neph1 Cooperates with Nephrin To Transduce a Signal That Induces Actin Polymerization.” *Molecular and Cellular Biology* 27 (24): 8698–8712. https://doi.org/10.1128/MCB.00948-07.

Gerke, Peter, Thomas Benzing, Martin Höhne, Andreas Kispert, Michael Frotscher, Gerd Walz, and Oliver Kretz. 2006. “Neuronal Expression and Interaction with the Synaptic Protein CASK Suggest a Role for Neph1 and Neph2 in Synaptogenesis.” *The Journal of Comparative Neurology* 498 (4): 466–75. https://doi.org/10.1002/cne.21064.

Gerke, Peter, Tobias B. Huber, Lorenz Sellin, Thomas Benzing, and Gerd Walz. 2003. “Homodimerization and Heterodimerization of the Glomerular Podocyte Proteins Nephrin and NEPH1.” *Journal of the American Society of Nephrology: JASN* 14 (4): 918–26. https://doi.org/10.1097/01.asn.0000057853.05686.89.

Gerke, Peter, Lorenz Sellin, Oliver Kretz, Daniel Petraschka, Hanswalter Zentgraf, Thomas Benzing, and Gerd Walz. 2005. “NEPH2 Is Located at the Glomerular Slit Diaphragm, Interacts with Nephrin and Is Cleaved from Podocytes by Metalloproteinases.” *Journal of the American Society of Nephrology: JASN* 16 (6): 1693–1702. https://doi.org/10.1681/ASN.2004060439.

Gilabert-Juan, Javier, Ana Rosa Sáez, Guillermo Lopez-Campos, Noelia Sebastiá-Ortega, Rocio González-Martínez, Juan Costa, Josep María Haro, et al. 2015. “Semaphorin and Plexin Gene Expression Is Altered in the Prefrontal Cortex of Schizophrenia Patients with and without Auditory Hallucinations.” *Psychiatry Research* 229 (3): 850–57. https://doi.org/10.1016/j.psychres.2015.07.074.

Giuffre, Brittney A., and Rebecca Jeanmonod. 2018. *Anatomy, Back, Nerves, Sciatic*. *StatPearls*.

Goodman, Kerry M., Rotem Rubinstein, Hanbin Dan, Fabiana Bahna, Seetha Mannepalli, Göran Ahlsén, Chan Aye Thu, et al. 2017. “Protocadherin Cis-Dimer Architecture and Recognition Unit Diversity.” *Proceedings of the National Academy of Sciences of the United States of America* 114 (46): E9829–37. https://doi.org/10.1073/pnas.1713449114.

Harita, Yutaka, Hidetake Kurihara, Hidetaka Kosako, Tohru Tezuka, Takashi Sekine, Takashi Igarashi, and Seisuke Hattori. 2008. “Neph1, a Component of the Kidney Slit Diaphragm, Is Tyrosine-Phosphorylated by the Src Family Tyrosine Kinase and Modulates Intracellular Signaling by Binding to Grb2.” *The Journal of Biological Chemistry* 283 (14): 9177–86. https://doi.org/10.1074/jbc.M707247200.

Hisaoka, Tomoko, Tadasuke Komori, Toshio Kitamura, and Yoshihiro Morikawa. 2018. “Abnormal Behaviours Relevant to Neurodevelopmental Disorders in Kirrel3-Knockout Mice.” *Scientific Reports* 8 (1): 1408. https://doi.org/10.1038/s41598-018-19844-7.

Hochberg, Georg K. A., and Joseph W. Thornton. 2017. “Reconstructing Ancient Proteins to Understand the Causes of Structure and Function.” *Annual Review of Biophysics* 46 (1): 247–69. https://doi.org/10.1146/annurev-biophys-070816-033631.

Hohenester, Erhard. 2008. “Structural Insight into Slit-Robo Signalling.” *Biochemical Society Transactions* 36 (Pt 2): 251–56. https://doi.org/10.1042/BST0360251.

Hong, Weizhe, and Liqun Luo. 2014. “Genetic Control of Wiring Specificity in the Fly Olfactory System.” *Genetics* 196 (1): 17–29. https://doi.org/10.1534/genetics.113.154336.

Hopkins, Jesse Bennett, Richard E. Gillilan, and Soren Skou. 2017. “BioXTAS RAW: Improvements to a Free Open-Source Program for Small-Angle X-Ray Scattering Data

Reduction and Analysis." *Journal of Applied Crystallography* 50 (Pt 5): 1545–53. https://doi.org/10.1107/S1600576717011438.

Howitt, Jason A, Naomi J Clout, and Erhard Hohenester. 2004. "Binding Site for Robo Receptors Revealed by Dissection of the Leucine-Rich Repeat Region of Slit." *The EMBO Journal* 23 (22): 4406–12. https://doi.org/10.1038/sj.emboj.7600446.

Hu, H. 2001. "Cell-Surface Heparan Sulfate Is Involved in the Repulsive Guidance Activities of Slit2 Protein." *Nature Neuroscience* 4 (July): 695–701. https://doi.org/10.1038/89482.

Huber, Tobias B, Miriam Schmidts, Peter Gerke, Bernhard Schermer, Anne Zahn, Björn Hartleben, Lorenz Sellin, Gerd Walz, and Thomas Benzing. 2003. "The Carboxyl Terminus of Neph Family Members Binds to the PDZ Domain Protein Zonula Occludens-1." *The Journal of Biological Chemistry* 278 (15): 13417–21. https://doi.org/10.1074/jbc.C200678200.

Huminiecki, Lukasz, Michael Gorn, Steven Suchting, Richard Poulsom, and Roy Bicknell. 2002. "Magic Roundabout Is a New Member of the Roundabout Receptor Family That Is Endothelial Specific and Expressed at Sites of Active Angiogenesis." *Genomics* 79 (4): 547–52. https://doi.org/10.1006/geno.2002.6745.

Hussain, Sadaf-Ahmahni, Michael Piper, Noémi Fukuhara, Laure Strochlic, Gian Cho, Jason A. Howitt, Yassir Ahmed, et al. 2006. "A Molecular Mechanism for the Heparan Sulfate Dependence of Slit-Robo Signaling." *The Journal of Biological Chemistry* 281 (51): 39693–98. https://doi.org/10/bmsk69.

Iversen, Katrine, François Beaubien, Janet E.A. Prince, and Jean-François Cloutier. 2020. "Axon Guidance: Slit–Robo Signaling." In *Cellular Migration and Formation of Axons and Dendrites*, 147–73. Elsevier. https://doi.org/10.1016/B978-0-12-814407-7.00007-9.

Jan, Yuh-Nung, and Lily Yeh Jan. 2010a. "Branching out: Mechanisms of Dendritic Arborization." *Nature Reviews Neuroscience* 11 (5): 316–28. https://doi.org/10.1038/nrn2836.

———. 2010b. "Branching out: Mechanisms of Dendritic Arborization." *Nature Reviews Neuroscience* 11 (5): 316–28. https://doi.org/10.1038/nrn2836.

Jaworski, Alexander, Hua Long, and Marc Tessier-Lavigne. 2010. "Collaborative and Specialized Functions of Robo1 and Robo2 in Spinal Commissural Axon Guidance." *The Journal of Neuroscience: The Official Journal of the Society for Neuroscience* 30 (28): 9445–53. https://doi.org/10.1523/JNEUROSCI.6290-09.2010.

Jaworski, Alexander, Irene Tom, Raymond K. Tong, Holly K. Gildea, Alexander W. Koch, Lino C. Gonzalez, and Marc Tessier-Lavigne. 2015. "Operational Redundancy in Axon Guidance through the Multifunctional Receptor Robo3 and Its Ligand NELL2." *Science (New York, N.Y.)* 350 (6263): 961–65. https://doi.org/10.1126/science.aad2615.

Jayabal, Panneerselvam, Fuchun Zhou, Xiufen Lei, Xiuye Ma, Barron Blackman, Susan T. Weintraub, Peter J. Houghton, and Yuzuru Shiio. 2021. “NELL2-Cdc42 Signaling Regulates BAF Complexes and Ewing Sarcoma Cell Growth.” *Cell Reports* 36 (1): 109254. https://doi.org/10.1016/j.celrep.2021.109254.

Jen, Joanna C., Wai-Man Chan, Thomas M. Bosley, Jijun Wan, Janai R. Carr, Udo Rüb, David Shattuck, et al. 2004. “Mutations in a Human ROBO Gene Disrupt Hindbrain Axon Pathway Crossing and Morphogenesis.” *Science (New York, N.Y.)* 304 (5676): 1509–13. https://doi.org/10.1126/science.1096437.

Jiang, Yulan, Hiroya Obama, Soh Leh Kuan, Ritsuko Nakamura, Chizu Nakamoto, Zhufeng Ouyang, and Masaru Nakamoto. 2009. “In Vitro Guidance of Retinal Axons by a Tectal Lamina-Specific Glycoprotein Nel.” *Molecular and Cellular Neurosciences* 41 (2): 113–19. https://doi.org/10.1016/j.mcn.2009.02.006.

Kabsch, Wolfgang. 2010. “XDS.” *Acta Crystallographica. Section D, Biological Crystallography* 66 (Pt 2): 125–32. https://doi.org/10.1107/S0907444909047337.

Kennedy, T E, T Serafini, J R de la Torre, and M Tessier-Lavigne. 1994. “Netrins Are Diffusible Chemotropic Factors for Commissural Axons in the Embryonic Spinal Cord.” *Cell* 78 (3): 425–35. https://doi.org/8062385.

Kim, Hyun, Chang Man Ha, Jungil Choi, Eun Jung Choi, Jongrye Jeon, Changmee Kim, Sang Kyu Park, Sang Soo Kang, Kyungjin Kim, and Byung Ju Lee. 2002. “Ontogeny and the Possible Function of a Novel Epidermal Growth Factor-like Repeat Domain-Containing Protein, NELL2, in the Rat Brain.” *Journal of Neurochemistry* 83 (December): 1389–1400.

Kolodkin, Alex L., and Marc Tessier-Lavigne. 2011. “Mechanisms and Molecules of Neuronal Wiring: A Primer.” *Cold Spring Harbor Perspectives in Biology* 3 (6). https://doi.org/10.1101/cshperspect.a001727.

Komiyama, Takaki, and Liqun Luo. 2006. “Development of Wiring Specificity in the Olfactory System.” *Current Opinion in Neurobiology* 16 (1): 67–73. https://doi.org/10.1016/j.conb.2005.12.002.

Kozlov, Alexey M., Diego Darriba, Tomáš Flouri, Benoit Morel, and Alexandros Stamatakis. 2019. “RAxML-NG: A Fast, Scalable and User-Friendly Tool for Maximum Likelihood Phylogenetic Inference.” *Bioinformatics (Oxford, England)* 35 (21): 4453–55. https://doi.org/10.1093/bioinformatics/btz305.

Kuroda, S., M. Oyasu, M. Kawakami, N. Kanayama, K. Tanizawa, N. Saito, T. Abe, S. Matsuhashi, and K. Ting. 1999. “Biochemical Characterization and Expression Analysis of Neural Thrombospondin-1-like Proteins NELL1 and NELL2.” *Biochemical and Biophysical Research Communications* 265 (1): 79–86. https://doi.org/10.1006/bbrc.1999.1638.

Laue, T. M., B. D. Shah, R. M. Ridgeway, and S. L. Pelletier. 1992. “Computer-Aided Interpretation of Analytical Sedimentation Data for Proteins.” In *Analytical Ultracentrifugation in Biochemistry and Polymer Science*, edited by S. E. Harding, A. J. Rowe, and J. C. Horton, 90–125. Cambridge, UK: The Royal Society of Chemistry.

Li, Pilong, Sudeep Banjade, Hui-Chun Cheng, Soyeon Kim, Baoyu Chen, Liang Guo, Marc Llaguno, et al. 2012. “Phase Transitions in the Assembly of Multivalent Signalling Proteins.” *Nature* 483 (7389): 336–40. https://doi.org/10.1038/nature10879.

Liebschner, Dorothee, Pavel V. Afonine, Matthew L. Baker, Gábor Bunkóczi, Vincent B. Chen, Tristan I. Croll, Bradley Hintze, et al. 2019. “Macromolecular Structure Determination Using X-Rays, Neutrons and Electrons: Recent Developments in Phenix.” *Acta Crystallographica. Section D, Structural Biology* 75 (Pt 10): 861–77. https://doi.org/10.1107/S2059798319011471.

Liu, Zhe, Kalpana Patel, Hannes Schmidt, William Andrews, Adrian Pini, and Vasi Sundaresan. 2004. “Extracellular Ig Domains 1 and 2 of Robo Are Important for Ligand (Slit) Binding.” *Molecular and Cellular Neurosciences* 26 (2): 232–40. https://doi.org/10.1016/j.mcn.2004.01.002.

Mambetisaeva, Elvira T., William Andrews, Laura Camurri, Adelaide Annan, and Vasi Sundaresan. 2005. “Robo Family of Proteins Exhibit Differential Expression in Mouse Spinal Cord and Robo-Slit Interaction Is Required for Midline Crossing in Vertebrate Spinal Cord.” *Developmental Dynamics: An Official Publication of the American Association of Anatomists* 233 (1): 41–51. https://doi.org/10.1002/dvdy.20324.

Manalastas-Cantos, K., P. V. Konarev, N. R. Hajizadeh, A. G. Kikhney, M. V. Petoukhov, D. S. Molodenskiy, A. Panjkovich, et al. 2021. “ATSAS 3.0: Expanded Functionality and New Tools for Small-Angle Scattering Data Analysis.” *Journal of Applied Crystallography* 54 (1): 343–55. https://doi.org/10.1107/S1600576720013412.

Martin, E. Anne, Shruti Muralidhar, Zhirong Wang, Diégo Cordero Cervantes, Raunak Basu, Matthew R. Taylor, Jennifer Hunter, et al. 2015. “The Intellectual Disability Gene Kirrel3 Regulates Target-Specific Mossy Fiber Synapse Development in the Hippocampus.” *ELife* 4: e09395. https://doi.org/10.7554/eLife.09395.

Matsuhashi, S., S. Noji, E. Koyama, F. Myokai, H. Ohuchi, S. Taniguchi, and K. Hori. 1995. “New Gene, Nel, Encoding a M(r) 93 K Protein with EGF-like Repeats Is Strongly Expressed in Neural Tissues of Early Stage Chick Embryos.” *Developmental Dynamics: An Official Publication of the American Association of Anatomists* 203 (2): 212–22. https://doi.org/10.1002/aja.1002030209.

McCoy, Airlie J., Ralf W. Grosse-Kunstleve, Paul D. Adams, Martyn D. Winn, Laurent C. Storoni, and Randy J. Read. 2007. “Phaser Crystallographic Software.” *Journal of Applied Crystallography* 40 (Pt 4): 658–74. https://doi.org/10.1107/S0021889807021206.

Mombaerts, P., F. Wang, C. Dulac, S. K. Chao, A. Nemes, M. Mendelsohn, J. Edmondson, and R. Axel. 1996. “Visualizing an Olfactory Sensory Map.” *Cell* 87 (4): 675–86. https://doi.org/10.1016/s0092-8674(00)81387-2.

Morlot, Cecile, Nicole M. Thielens, Raimond B. G. Ravelli, Wieger Hemrika, Roland A. Romijn, Piet Gros, Stephen Cusack, and Andrew A. McCarthy. 2007. “Structural Insights into the Slit-Robo Complex.” *Proceedings of the National Academy of Sciences of the United States of America* 104 (38): 14923–28. https://doi.org/10.1073/pnas.0705310104.

Nakamoto, Chizu, Elaine Durward, Masato Horie, and Masaru Nakamoto. 2019. “Nell2 Regulates the Contralateral-versus-Ipsilateral Visual Projection as a Domain-Specific Positional Cue.” *Development (Cambridge, England)* 146 (4): dev170704. https://doi.org/10.1242/dev.170704.

Nakamura, Yoko, Ai Hasebe, Kaneyoshi Takahashi, Masumi Iijima, Nobuo Yoshimoto, Andrés D. Maturana, Kang Ting, Shun’ichi Kuroda, and Tomoaki Niimi. 2014. “Oligomerization-Induced Conformational Change in the C-Terminal Region of Nel-like Molecule 1 (NELL1) Protein Is Necessary for the Efficient Mediation of Murine MC3T3-E1 Cell Adhesion and Spreading.” *The Journal of Biological Chemistry* 289 (14): 9781–94. https://doi.org/10.1074/jbc.M113.507020.

Nakashima, Ai, Naoki Ihara, Mayo Shigeta, Hiroshi Kiyonari, Yuji Ikegaya, and Haruki Takeuchi. 2019. “Structured Spike Series Specify Gene Expression Patterns for Olfactory Circuit Formation.” *Science (New York, N.Y.)* 365 (6448). https://doi.org/10.1126/science.aaw5030.

Nelson, Branden R., Sachiko Matsuhashi, and Frances Lefcort. 2002. “Restricted Neural Epidermal Growth Factor-like like 2 (NELL2) Expression during Muscle and Neuronal Differentiation.” *Mechanisms of Development* 119 Suppl 1 (December): S11-9.

Ogawa, Mitsutaka, Yuya Senoo, Kazutaka Ikeda, Hideyuki Takeuchi, and Tetsuya Okajima. 2018. “Structural Divergence in O-GlcNAc Glycans Displayed on Epidermal Growth Factor-like Repeats of Mammalian Notch1.” *Molecules (Basel, Switzerland)* 23 (7). https://doi.org/10.3390/molecules23071745.

Oliveros, Juan C., Mònica Franch, Daniel Tabas-Madrid, David San-León, Lluis Montoliu, Pilar Cubas, and Florencio Pazos. 2016. “Breaking-Cas-Interactive Design of Guide RNAs for CRISPR-Cas Experiments for ENSEMBL Genomes.” *Nucleic Acids Research* 44 (W1): W267-271. https://doi.org/10.1093/nar/gkw407.

Otwinowski, Zbyszek, and Wladek Minor. 1997. “[20] Processing of X-Ray Diffraction Data Collected in Oscillation Mode.” In *Macromolecular Crystallography, Part A*, edited by Charles W. Carter Jr. and Robert M. Sweet, 276:307–26. Methods in Enzymology. Academic Press (New York). https://doi.org/10.1016/S0076-6879(97)76066-X.

Özkan, Engin, Robert A Carrillo, Catharine L Eastman, Richard Weiszmann, Deepa Waghray, Karl G Johnson, Kai Zinn, Susan E Celniker, and K Christopher Garcia. 2013. "An Extracellular Interactome of Immunoglobulin and LRR Proteins Reveals Receptor-Ligand Networks." *Cell* 154 (1): 228–39. https://doi.org/10.1016/j.cell.2013.06.006.

Özkan, Engin, Poh Hui Chia, Ruiqi Rachel Wang, Natalia Goriatcheva, Dominika Borek, Zbyszek Otwinowski, Thomas Walz, Kang Shen, and K Christopher Garcia. 2014. "Extracellular Architecture of the SYG-1/SYG-2 Adhesion Complex Instructs Synaptogenesis." *Cell* 156 (3): 482–94. https://doi.org/10.1016/j.cell.2014.01.004.

Petoukhov, Maxim V., and Dmitri I. Svergun. 2005. "Global Rigid Body Modeling of Macromolecular Complexes against Small-Angle Scattering Data." *Biophysical Journal* 89 (2): 1237–50. https://doi.org/10.1529/biophysj.105.064154.

Poncelet, Guillaume, and Sebastian M. Shimeld. 2020. "The Evolutionary Origins of the Vertebrate Olfactory System." *Open Biology* 10 (12): 200330. https://doi.org/10.1098/rsob.200330.

Prince, Janet E. A., Alexandra C. Brignall, Tyler Cutforth, Kang Shen, and Jean-François Cloutier. 2013. "Kirrel3 Is Required for the Coalescence of Vomeronasal Sensory Neuron Axons into Glomeruli and for Male-Male Aggression." *Development (Cambridge, England)* 140 (11): 2398–2408. https://doi.org/10.1242/dev.087262.

Putaala, H. 2001. "The Murine Nephrin Gene Is Specifically Expressed in Kidney, Brain and Pancreas: Inactivation of the Gene Leads to Massive Proteinuria and Neonatal Death." *Human Molecular Genetics* 10 (1): 1–8. https://doi.org/10.1093/hmg/10.1.1.

Rambo, Robert P., and John A. Tainer. 2013. "Accurate Assessment of Mass, Models and Resolution by Small-Angle Scattering." *Nature* 496 (7446): 477–81. https://doi.org/10.1038/nature12070.

Ramos, R G, G L Igloi, B Lichte, U Baumann, D Maier, T Schneider, J H Brandstätter, A Fröhlich, and K F Fischbach. 1993. "The Irregular Chiasm C-Roughest Locus of Drosophila, Which Affects Axonal Projections and Programmed Cell Death, Encodes a Novel Immunoglobulin-like Protein." *Genes & Development* 7 (12B): 2533–47.

Rodriguez, I., P. Feinstein, and P. Mombaerts. 1999. "Variable Patterns of Axonal Projections of Sensory Neurons in the Mouse Vomeronasal System." *Cell* 97 (2): 199–208. https://doi.org/10.1016/s0092-8674(00)80730-8.

Rothberg, J. M., J. R. Jacobs, C. S. Goodman, and S. Artavanis-Tsakonas. 1990. "Slit: An Extracellular Protein Necessary for Development of Midline Glia and Commissural Axon Pathways Contains Both EGF and LRR Domains." *Genes & Development* 4 (12A): 2169–87.

Roy, Ambrish, Alper Kucukural, and Yang Zhang. 2010. “I-TASSER: A Unified Platform for Automated Protein Structure and Function Prediction.” *Nature Protocols* 5 (4): 725–38. https://doi.org/10.1038/nprot.2010.5.

Rubinstein, Rotem, Chan Aye Thu, Kerry Marie Goodman, Holly Noelle Wolcott, Fabiana Bahna, Seetha Mannepalli, Goran Ahlsen, et al. 2015. “Molecular Logic of Neuronal Self-Recognition through Protocadherin Domain Interactions.” *Cell* 163 (October): 629–42. https://doi.org/10.1016/j.cell.2015.09.026.

Ruiz-Gómez, M., N. Coutts, A. Price, M. V. Taylor, and M. Bate. 2000. “Drosophila Dumbfounded: A Myoblast Attractant Essential for Fusion.” *Cell* 102 (2): 189–98.

Russell, Samantha A., and Greg J. Bashaw. 2018. “Axon Guidance Pathways and the Control of Gene Expression: Axon Guidance Pathways and Gene Expression.” *Developmental Dynamics* 247 (4): 571–80. https://doi.org/10.1002/dvdy.24609.

Sabatier, Christelle, Andrew S. Plump, null Le Ma, Katja Brose, Atsushi Tamada, Fujio Murakami, Eva Y.-H. P. Lee, and Marc Tessier-Lavigne. 2004. “The Divergent Robo Family Protein Rig-1/Robo3 Is a Negative Regulator of Slit Responsiveness Required for Midline Crossing by Commissural Axons.” *Cell* 117 (2): 157–69.

Sakurai, Takayuki, Satoshi Watanabe, Akiko Kamiyoshi, Masahiro Sato, and Takayuki Shindo. 2014. “A Single Blastocyst Assay Optimized for Detecting CRISPR/Cas9 System-Induced Indel Mutations in Mice.” *BMC Biotechnology* 14 (July): 69. https://doi.org/10.1186/1472-6750-14-69.

Salzberg, Yehuda, Carlos A. Díaz-Balzac, Nelson J. Ramirez-Suarez, Matthew Attreed, Eillen Tecle, Muriel Desbois, Zaven Kaprielian, and Hannes E. Bülow. 2013. “Skin-Derived Cues Control Arborization of Sensory Dendrites in Caenorhabditis Elegans.” *Cell* 155 (2): 308–20. https://doi.org/10.1016/j.cell.2013.08.058.

Salzman, Gabriel S., Sarah D. Ackerman, Chen Ding, Akiko Koide, Katherine Leon, Rong Luo, Hannah M. Stoveken, et al. 2016. “Structural Basis for Regulation of GPR56/ADGRG1 by Its Alternatively Spliced Extracellular Domains.” *Neuron* 91 (6): 1292–1304. https://doi.org/10.1016/j.neuron.2016.08.022.

Sanes, Joshua R., and S. Lawrence Zipursky. 2020. “Synaptic Specificity, Recognition Molecules, and Assembly of Neural Circuits.” *Cell* 181 (3): 536–56. https://doi.org/10.1016/j.cell.2020.04.008.

Schindelin, Johannes, Ignacio Arganda-Carreras, Erwin Frise, Verena Kaynig, Mark Longair, Tobias Pietzsch, Stephan Preibisch, et al. 2012. “Fiji: An Open-Source Platform for Biological-Image Analysis.” *Nature Methods* 9 (7): 676–82. https://doi.org/10.1038/nmeth.2019.

Schroeder, Anna, and Joris de Wit. 2018. “Leucine-Rich Repeat-Containing Synaptic Adhesion Molecules as Organizers of Synaptic Specificity and Diversity.” *Experimental & Molecular Medicine* 50 (4): 1–9. https://doi.org/10.1038/s12276-017-0023-8.

Schuck, P. 2000. “Size-Distribution Analysis of Macromolecules by Sedimentation Velocity Ultracentrifugation and Lamm Equation Modeling.” *Biophysical Journal* 78 (3): 1606–19. https://doi.org/10.1016/S0006-3495(00)76713-0.

Schuck, Peter. 2003. “On the Analysis of Protein Self-Association by Sedimentation Velocity Analytical Ultracentrifugation.” *Analytical Biochemistry* 320 (1): 104–24. https://doi.org/10.1016/s0003-2697(03)00289-6.

Seiradake, Elena, Anne C. von Philipsborn, Maud Henry, Martin Fritz, Hugues Lortat-Jacob, Marc Jamin, Wieger Hemrika, Martin Bastmeyer, Stephen Cusack, and Andrew A. McCarthy. 2009. “Structure and Functional Relevance of the Slit2 Homodimerization Domain.” *EMBO Reports* 10 (7): 736–41. https://doi.org/10.1038/embor.2009.95.

Sellin, Lorenz, Tobias B. Huber, Peter Gerke, Ivo Quack, Hermann Pavenstädt, and Gerd Walz. 2003. “NEPH1 Defines a Novel Family of Podocin Interacting Proteins.” *FASEB Journal: Official Publication of the Federation of American Societies for Experimental Biology* 17 (1): 115–17. https://doi.org/10.1096/fj.02-0242fje.

Serizawa, Shou, Kazunari Miyamichi, Haruki Takeuchi, Yuya Yamagishi, Misao Suzuki, and Hitoshi Sakano. 2006. “A Neuronal Identity Code for the Odorant Receptor-Specific and Activity-Dependent Axon Sorting.” *Cell* 127 (5): 1057–69. https://doi.org/10.1016/j.cell.2006.10.031.

Shen, Kang, and Cornelia I Bargmann. 2003. “The Immunoglobulin Superfamily Protein SYG-1 Determines the Location of Specific Synapses in C. Elegans.” *Cell* 112 (5): 619–30.

Shi, Rebecca, Daniel A. Kramer, Baoyu Chen, and Kang Shen. 2021. “A Two-Step Actin Polymerization Mechanism Drives Dendrite Branching.” *Neural Development* 16 (1): 3. https://doi.org/10.1186/s13064-021-00154-0.

Siddiq, Mohammad A, Georg KA Hochberg, and Joseph W Thornton. 2017. “Evolution of Protein Specificity: Insights from Ancestral Protein Reconstruction.” *Current Opinion in Structural Biology* 47 (December): 113–22. https://doi.org/10.1016/j.sbi.2017.07.003.

Stamatakis, Alexandros. 2014. “RAxML Version 8: A Tool for Phylogenetic Analysis and Post-Analysis of Large Phylogenies.” *Bioinformatics (Oxford, England)* 30 (9): 1312–13. https://doi.org/10.1093/bioinformatics/btu033.

Stoeckli, Esther T. 2018. “Understanding Axon Guidance: Are We Nearly There Yet?” *Development* 145 (10): dev151415. https://doi.org/10.1242/dev.151415.

Südhof, Thomas C. 2017. "Synaptic Neurexin Complexes: A Molecular Code for the Logic of Neural Circuits." *Cell* 171 (4): 745–69. https://doi.org/10.1016/j.cell.2017.10.024.

Sundaresan, V., I. Roberts, A. Bateman, A. Bankier, M. Sheppard, C. Hobbs, J. Xiong, et al. 1998. "The DUTT1 Gene, a Novel NCAM Family Member Is Expressed in Developing Murine Neural Tissues and Has an Unusually Broad Pattern of Expression." *Molecular and Cellular Neurosciences* 11 (1–2): 29–35. https://doi.org/10.1006/mcne.1998.0672.

Svergun, D. I. 1992. "Determination of the Regularization Parameter in Indirect-Transform Methods Using Perceptual Criteria." *Journal of Applied Crystallography* 25 (4): 495–503. https://doi.org/10.1107/S0021889892001663.

Tang, Leo TH, Carlos A Diaz-Balzac, Maisha Rahman, Nelson J Ramirez-Suarez, Yehuda Salzberg, Maria I Lázaro-Peña, and Hannes E Bülow. 2019. "TIAM-1/GEF Can Shape Somatosensory Dendrites Independently of Its GEF Activity by Regulating F-Actin Localization." *ELife* 8 (January): e38949. https://doi.org/10.7554/eLife.38949.

Taylor, Matthew R., E. Anne Martin, Brooke Sinnen, Rajdeep Trilokekar, Emmanuelle Ranza, Stylianos E. Antonarakis, and Megan E. Williams. 2020. "Kirrel3-Mediated Synapse Formation Is Attenuated by Disease-Associated Missense Variants." *The Journal of Neuroscience: The Official Journal of the Society for Neuroscience* 40 (28): 5376–88. https://doi.org/10.1523/JNEUROSCI.3058-19.2020.

Terwilliger, Thomas C., Paul D. Adams, Randy J. Read, Airlie J. McCoy, Nigel W. Moriarty, Ralf W. Grosse-Kunstleve, Pavel V. Afonine, Peter H. Zwart, and Li Wei Hung. 2009. "Decision-Making in Structure Solution Using Bayesian Estimates of Map Quality: The PHENIX AutoSol Wizard." *Acta Crystallographica. Section D, Biological Crystallography* 65 (Pt 6): 582–601. https://doi.org/10.1107/S0907444909012098.

Tria, Giancarlo, Haydyn D. T. Mertens, Michael Kachala, and Dmitri I. Svergun. 2015. "Advanced Ensemble Modelling of Flexible Macromolecules Using X-Ray Solution Scattering." *IUCrJ* 2 (Pt 2): 207–17. https://doi.org/10.1107/S205225251500202X.

Vaddadi, Neelima, Katrine Iversen, Reesha Raja, Alina Phen, Alexandra Brignall, Emilie Dumontier, and Jean-François Cloutier. 2019. "Kirrel2 Is Differentially Required in Populations of Olfactory Sensory Neurons for the Targeting of Axons in the Olfactory Bulb." *Development (Cambridge, England)* 146 (11). https://doi.org/10.1242/dev.173310.

Vagin, A., and A. Lebedev. 2015. "MoRDa, an Automatic Molecular Replacement Pipeline." *Acta Crystallographica Section A: Foundations and Advances* A71 (August): s19. https://doi.org/10.1107/S2053273315099672.

Völker, Linus A., Barbara A. Maar, Barbara A. Pulido Guevara, Andras Bilkei-Gorzo, Andreas Zimmer, Hella Brönneke, Claudia Dafinger, et al. 2018. "Neph2/Kirrel3 Regulates

Sensory Input, Motor Coordination, and Home-Cage Activity in Rodents." *Genes, Brain, and Behavior* 17 (8): e12516. https://doi.org/10.1111/gbb.12516.

Volkov, Vladimir V., and Dmitri I. Svergun. 2003. "Uniqueness of Ab Initio Shape Determination in Small-angle Scattering." *Journal of Applied Crystallography* 36 (3-1): 860–64. https://doi.org/10.1107/S0021889803000268.

Vulliemoz, Serge, Olivier Raineteau, and Denis Jabaudon. 2005. "Reaching beyond the Midline: Why Are Human Brains Cross Wired?" *The Lancet Neurology* 4 (2): 87–99. https://doi.org/10.1016/S1474-4422(05)00990-7.

Wang, Fan, Adriana Nemes, Monica Mendelsohn, and Richard Axel. 1998. "Odorant Receptors Govern the Formation of a Precise Topographic Map." *Cell* 93 (1): 47–60. https://doi.org/10.1016/S0092-8674(00)81145-9.

Watanabe, T. K., T. Katagiri, M. Suzuki, F. Shimizu, T. Fujiwara, N. Kanemoto, Y. Nakamura, Y. Hirai, H. Maekawa, and E. i Takahashi. 1996. "Cloning and Characterization of Two Novel Human CDNAs (NELL1 and NELL2) Encoding Proteins with Six EGF-like Repeats." *Genomics* 38 (3): 273–76.

Wolff, T, and D F Ready. 1991. "Cell Death in Normal and Rough Eye Mutants of Drosophila." *Development (Cambridge, England)* 113 (3): 825–39.

Xu, Kai, Zhuhao Wu, Nicolas Renier, Alexander Antipenko, Dorothea Tzvetkova-Robev, Yan Xu, Maria Minchenko, et al. 2014. "Neural Migration. Structures of Netrin-1 Bound to Two Receptors Provide Insight into Its Axon Guidance Mechanism." *Science (New York, N.Y.)* 344 (6189): 1275–79. https://doi.org/10.1126/science.1255149.

Yadav, Suresh Singh, and Gopeshwar Narayan. 2014. "Role of ROBO4 Signalling in Developmental and Pathological Angiogenesis." *BioMed Research International* 2014: 683025. https://doi.org/10.1155/2014/683025.

Yam, Patricia T., Sébastien D. Langlois, Steves Morin, and Frédéric Charron. 2009. "Sonic Hedgehog Guides Axons through a Noncanonical, Src-Family-Kinase-Dependent Signaling Pathway." *Neuron* 62 (3): 349–62. https://doi.org/10.1016/j.neuron.2009.03.022.

Yamagata, Masahito, Joshua R Sanes, and Joshua A Weiner. 2003. "Synaptic Adhesion Molecules." *Current Opinion in Cell Biology* 15 (5): 621–32.

Yamamoto, Naoka, Manabu Kashiwagi, Manami Ishihara, Takaaki Kojima, Andrés D. Maturana, Shun'ichi Kuroda, and Tomoaki Niimi. 2019. "Robo2 Contains a Cryptic Binding Site for Neural EGFL-like (NELL) Protein 1/2." *The Journal of Biological Chemistry* 294 (12): 4693–4703. https://doi.org/10.1074/jbc.RA118.005819.

Yang, Jianyi, and Yang Zhang. 2015. "I-TASSER Server: New Development for Protein Structure and Function Predictions." *Nucleic Acids Research* 43 (W1): W174-181. https://doi.org/10.1093/nar/gkv342.

Yang, Ziheng. 2007. "PAML 4: Phylogenetic Analysis by Maximum Likelihood." *Molecular Biology and Evolution* 24 (8): 1586–91. https://doi.org/10.1093/molbev/msm088.

Ye, Xiyue, Yan Qiu, Yuqing Gao, Dong Wan, and Huifeng Zhu. 2019. "A Subtle Network Mediating Axon Guidance: Intrinsic Dynamic Structure of Growth Cone, Attractive and Repulsive Molecular Cues, and the Intermediate Role of Signaling Pathways." *Neural Plasticity* 2019 (April): 1–26. https://doi.org/10.1155/2019/1719829.

Yesildag, Burcak, Thomas Bock, Karolin Herrmanns, Bernd Wollscheid, and Markus Stoffel. 2015. "Kin of IRRE-like Protein 2 Is a Phosphorylated Glycoprotein That Regulates Basal Insulin Secretion." *The Journal of Biological Chemistry* 290 (43): 25891–906. https://doi.org/10.1074/jbc.M115.684704.

Yom-Tov, Galit, Reut Barak, Omri Matalon, Mira Barda-Saad, Julia Guez-Haddad, and Yarden Opatowsky. 2017. "Robo Ig4 Is a Dimerization Domain." *Journal of Molecular Biology* 429 (23): 3606–16. https://doi.org/10.1016/j.jmb.2017.10.002.

Zakrys, Linas, Richard J. Ward, John D. Pediani, Antoine G. Godin, Gerard J. Graham, and Graeme Milligan. 2014. "Roundabout 1 Exists Predominantly as a Basal Dimeric Complex and This Is Unaffected by Binding of the Ligand Slit2." *The Biochemical Journal* 461 (1): 61–73. https://doi.org/10.1042/BJ20140190.

Zapiec, Bolek, and Peter Mombaerts. 2015. "Multiplex Assessment of the Positions of Odorant Receptor-Specific Glomeruli in the Mouse Olfactory Bulb by Serial Two-Photon Tomography." *Proceedings of the National Academy of Sciences* 112 (43): E5873–82. https://doi.org/10.1073/pnas.1512135112.

Zelina, Pavol, Heike Blockus, Yvrick Zagar, Amélie Péres, François Friocourt, Zhuhao Wu, Nicolas Rama, Coralie Fouquet, Erhard Hohenester, Marc Tessier-Lavigne, Jörn Schweitzer, Hugues Roest Crollius, et al. 2014. "Signaling Switch of the Axon Guidance Receptor Robo3 during Vertebrate Evolution." *Neuron* 84 (6): 1258–72. https://doi.org/10.1016/j.neuron.2014.11.004.

Zelina, Pavol, Heike Blockus, Yvrick Zagar, Amélie Péres, François Friocourt, Zhuhao Wu, Nicolas Rama, Coralie Fouquet, Erhard Hohenester, Marc Tessier-Lavigne, Jörn Schweitzer, Hugues Roest Crollius, et al. 2014. "Signaling Switch of the Axon Guidance Receptor Robo3 during Vertebrate Evolution." *Neuron* 84 (6): 1258–72. https://doi.org/10.1016/j.neuron.2014.11.004.

Zhao, Huaying, Chad A. Brautigam, Rodolfo Ghirlando, and Peter Schuck. 2013. "Overview of Current Methods in Sedimentation Velocity and Sedimentation Equilibrium Analytical

Ultracentrifugation." *Current Protocols in Protein Science*, February, Unit20.12. https://doi.org/10.1002/0471140864.ps2012s71.

Zou, Wei, Ao Shen, Xintong Dong, Madina Tugizova, Yang K Xiang, and Kang Shen. 2016. "A Multi-Protein Receptor-Ligand Complex Underlies Combinatorial Dendrite Guidance Choices in C. Elegans." *ELife* 5 (October). https://doi.org/10.7554/eLife.18345.